

Fabrication of Polymeric Materials via Anodic Aluminum Oxide Templating

Zur Erlangung des akademischen Grades eines

DOKTORS DER NATURWISSENSCHAFTEN

(Dr. rer. nat.)

von der KIT-Fakultät für Chemie und Biowissenschaften

des Karlsruher Instituts für Technologie (KIT)

genehmigte

DISSERTATION

von

M.Sc. Xia Huang

aus

Chongqing, V. R. China

KIT-Dekan:	Prof. Dr. Manfred Wilhelm
Referent:	Prof. Dr. Patrick Théato
Korreferent:	Prof. Dr. Pavel Levkin
Tag der mündlichen Prüfung:	21.07.2020

Die vorliegende Arbeit wurde vom Oktober 2015 bis März 2020 unter Anleitung von Prof. Dr Patrick Théato am Karlsruher Institut für Technologie (KIT) und der Universität Hamburg (UHH) im Rahmen einer gemeinschaftlichen Betreuung angefertigt.

Erklärung

Ich versichere hiermit, dass ich diese Arbeit selbstständig angefertigt habe und keine anderen, als die angegebenen Quellen und Hinweise benutzt, sowie die wörtlich oder inhaltlich übernommenen Stellen als solche kenntlich gemacht und die Satzung des Karlsruher Instituts für Technologie (KIT) zur Sicherung guter wissenschaftlicher Praxis in der gültigen Fassung beachtet habe. Die elektronische Version der Arbeit stimmt mit der schriftlichen überein und die Abgabe und Archivierung der Primärdaten gemäß Abs. A (6) der Regeln zur Sicherung guter wissenschaftlicher Praxis des KIT beim Institut ist gesichert.

Karlsruhe, 06.08.2020

Abstract

Differing from hard bulk materials, polymeric soft nanomaterials have received enormous interests owing to their unique physical and chemical properties. Control of the properties and responsiveness of nanomaterials is essential for tailoring their applications in new technologies. Anodic aluminum oxide (AAO) templates that feature well-arranged cylindrical nanopores are a versatile tool for preparing nanostructured materials. The porous structure of AAO is adjustable on demand which could further realize morphological control of obtained nanomaterials. In order to comprehensively investigate nanomaterials from synthesis to applications, herein a structure adjustable AAO templating strategy, featuring with flexibility and adjustability, is applied as a powerful methodology to construct polymeric nanomaterials, leading to potential applications of polymeric nanomaterials in diverse fields.

In this thesis, based on a self-made laboratory AAO setup, AAO templates that differ in their structures and morphologies, were fabricated. Furthermore, the relationship between working conditions, such as anodization time and type of electrolyte, as well as template structures were intensively studied for further customized designs (Chapter 3). Subsequently, the fabricated AAO templates were used to prepare one dimensional polymeric Janus nanorods. A single nanorod consists of two different polymeric segments which are chemically bonded. According to this, variations of each block for the preparation of distinguished Janus nanorods upon specific designs are achievable (Chapter 4). Subsequently, two dimensional smart films bearing well-arranged pillar arrays are prepared. Combining *in situ* polymerization under confinement in the cylindrical pores of an AAO template with post-polymerization modification, hierarchical films bearing well-aligned poly(pentafluorophenyl acrylate) micro-arrays grafted with pH responsive poly(methacrylic acid) nanobrushes are obtained. These smart films show underwater superoleophobicity and pH reversible oil adhesion property that are promising for oil manipulation. The developed methodology is mild and with high efficiency, which could be used for facile fabrication of various hierarchical films (Chapter 5). Ultimately, smart composite membranes featuring three dimensional structures were fabricated based on through-hole isotropic AAO templates. In detail, AAO membranes were functionalized via grafting of the carbon dioxide responsive polymer poly(methyl methacrylate-*co*-2-(diethylamino)ethyl methacrylate) through surface-initiated reversible addition-fragmentation chain transfer polymerization. The carbon dioxide dependent filtration efficiency of obtained polymer-AAO composite membranes for water and oil-water emulsions are further investigated (Chapter 6).

In summary, AAO templating is a powerful tool to fabricate nanostructures of diverse dimensions. By combining AAO templating with established synthesis and modification approaches, polymeric nanomaterials ranging from one to two to three dimensions are readily prepared. The fabrication methods

listed in this thesis are not designed for individual applications, but for customary applications in the field of polymer science towards the preparation of intelligent nanomaterials.

Zusammenfassung

Im Gegensatz zu harten Materialien haben polymere weiche Nanomaterialien mit identischer Zusammensetzung aufgrund ihrer einzigartigen physikalischen und chemischen Eigenschaften enormes Interesse erhalten. Die Kontrolle der Eigenschaften und der Reaktionsfähigkeit von Nanomaterialien ist für die Anpassung ihrer Anwendungen in neue Technologien von entscheidender Bedeutung. Anodische Aluminiumoxid (AAO)-Template mit wohlangeordneten zylindrischen Nanoporen sind ein vielseitiges Werkzeug zur Herstellung nanostrukturierter Materialien. Die poröse Struktur von AAO ist bei Bedarf einstellbar, wodurch die morphologische Kontrolle der erhaltenen Nanomaterialien weitergreifend realisiert werden könnte. Um Nanomaterialien von der Synthese bis zur Anwendung umfassend zu untersuchen, wird hier eine strukturanpassbare AAO-Templat-Strategie mit Flexibilität und Einstellbarkeit als leistungsstarkes Werkzeug zum Aufbau polymerer Nanomaterialien angewendet, was zu potenziellen Anwendungen polymerer Nanomaterialien in verschiedenen Bereichen führt.

In dieser Arbeit wurden AAO-Template hergestellt, die sich in ihren Strukturen und Morphologien unterscheiden und auf einem selbst erstellten AAO-Labora Aufbau basieren. Darüber hinaus wurde der Zusammenhang zwischen Arbeitsbedingungen wie Anodisierungszeit und Elektrolyttyp sowie Templatstrukturen für weitere anwendungsspezifische Konstruktionen intensiv untersucht (Kapitel 3). Anschließend wurden die hergestellten AAO-Template verwendet, um eindimensionale polymere Janus-Nanostäbe herzustellen. Ein einzelner Nanostab besteht aus zwei verschiedenen Polymersegmenten, die chemisch verbunden sind. Demnach sind Variationen jedes Blocks zur Herstellung von ausgezeichneten Janus-Nanostäben nach bestimmten Designs möglich (Kapitel 4). Anschließend werden zweidimensionale intelligente Filme mit gut angeordneten Säulen anordnungen hergestellt. Durch Kombination der In-situ-Polymerisation unter Einschluss in den zylindrischen Poren eines AAO-Templats mit der Post-Polymerisationsmodifikation werden hierarchische Filme mit wohlausgerichteten Poly(pentafluorphenylacrylat)-Mikroarrays erhalten, auf die mit auf pH-Wert ansprechenden Poly(methacrylsäure)-Nanobürsten gepropft sind. Diese intelligenten Filme zeigen Unterwasser-Superoleophobie und pH-reversible Adhäsionseigenschaften zu Öl, welche für die Ölmanipulation vielversprechend sind. Die entwickelte Methodik ist mild und von hoher Effizienz, die zur einfachen Herstellung verschiedener hierarchischer Filme verwendet werden kann (Kapitel 5). Letztendlich wurden intelligente Verbundmembranen mit dreidimensionalen Strukturen auf der Basis von isotropen AAO-Templaten mit Durchgangsloch hergestellt. Im Detail wurden AAO-Membranen durch Pfropfen des auf Kohlendioxid ansprechenden Polymers Poly(methylmethacrylat-co-2-(diethylamino) ethylmethacrylat) durch oberflächeninitiierte reversible Additions-Fragmentierungs-Kettenübertragungspolymerisation

funktionalisiert. Die kohlendioxidabhängige Filtrationseffizienz der erhaltenen Polymer-AAO-Verbundmembranen für Wasser- und Öl-Wasser-Emulsionen wurde untersucht (Kapitel 6).

Zusammenfassend ist festzuhalten, dass AAO-Templatisierung ein leistungsstarkes Werkzeug zur Herstellung von Nanostrukturen mit verschiedenen Dimensionen. Durch die Kombination von AAO-Templaten mit etablierten Synthese- und Modifizierungsansätzen lassen sich leicht polymere Nanomaterialien im Bereich von einer, zwei und bis drei Dimensionen herstellen. Die in dieser Arbeit aufgeführten Herstellungsverfahren sind nicht für Einzelanwendungen konzipiert, sondern für übliche Anwendungen auf dem Gebiet der Polymerwissenschaft zur Herstellung intelligenter Nanomaterialien.

Contents

Erklärung.....	III
Abstract	V
Zusammenfassung	VII
1. Introduction	1
1.1. History and General Remarks	2
1.2. Porous Anodic Aluminum Oxide Template	3
1.2.1. Types of Anodic Aluminum Oxide Template	4
1.2.2. Electrochemical Principles during Anodic Aluminum Oxide Template Fabrication.....	5
1.2.3. Pore Formation Mechanisms	6
1.3. General AAO Template Fabrication Method and Experimental Set-up	9
1.4. Controlled Parameters of AAO Template Pore Density	10
1.4.1. Pore Diameter.....	11
1.4.2. Pore Length	11
1.4.3. Interpore Distance	12
1.4.4. Complex Internal Pore Architectures	12
1.5. AAO template Assisted Fabrication of Polymer Nanostructures	14
1.5.1. Melt Template Wetting	15
1.5.2. Solution Template Wetting.....	15
1.5.3. Polymerization in AAO Template.....	17
1.5.4. Layer-by-layer Assembly	19
1.5.5. Electrochemical Deposition.....	20
1.6. Polymeric Nanoarrays via AAO Templating	21
1.6.1. Dry Adhesion and Hydrophobic Surfaces	21
1.6.2. Optical Applications.....	23
1.6.3. Stimuli-Responsive Nanopillars.....	24
1.6.3.1. Temperature Responsive Polymers and Nanopillars.....	25
1.6.3.2. pH Responsive Polymers and Nanopillars	27
1.6.3.3. Light Responsive Polymers and Nanopillars.....	28
1.6.4. Bio-related Applications.....	29
1.7. Direct Functionalization of AAO Membrane.....	31
1.7.1. Self-Assembly	32

1.7.2. Initiated Chemical Vapor Deposition	34
1.7.3. Polymer Grafting	34
2. Scope and Objectives	39
3. Manufacturing of AAO Templates	41
3.1. Introduction	41
3.2. Electro-polishing	42
3.3. First Anodization	43
3.4. Chemical Etching	44
3.5. Second Anodization	45
3.6. Pore Widening	47
3.7. Aluminum Removing	48
3.8 Backside Opening	49
3.9. Conclusion	50
4. Polymeric One-dimensional Janus Nanorods via AAO Templating	51
4.1. Introduction	51
4.2. Strategy	53
4.3. Results and Discussion	54
4.4. Conclusion	59
5. Hierarchical Superoleophobic Film with Reversible pH Response from AAO Patterning	60
5.1. Introduction	61
5.2. Strategy	63
5.3. Results and Discussion	64
5.4. Conclusion	72
6. Carbon Dioxide Gated AAO Based Nanocomposite Membrane	74
6.1. Introduction	74
6.2. Strategy	76
6.3. Results and Discussion	77
6.4. Conclusion	85
7. Concluding Remarks and Outlook	87
8. Materials and Methods	89
8.1. Materials	89
8.2. Characterization Methods and Instrumentations	90
8.2.1. Scanning Electron Microscopy	90
8.2.1.1. Theoretical Background	90
8.2.1.2. Instrumental Information	91

8.2.2. Transmittance Electron Microscopy.....	91
8.2.2.1. Theoretical Background	91
8.2.2.2. Instrumental Information.....	92
8.2.3. Oxygen Plasma Cleaner	92
8.2.3.1. Theoretical Background	92
8.2.3.2. Instrumental Information.....	93
8.2.4. Fourier-transformation Infrared Spectroscopy	93
8.2.4.1. Theoretical Background	93
8.2.4.2. Instrumental Information.....	94
8.2.5. Nuclear Magnetic Resonance Spectroscopy.....	94
8.2.5.1. Theoretical Background	94
8.2.5.2. Instrumental Information.....	95
8.2.6. Gel Permeation Chromatography	95
8.2.6.1. Theoretical Background	95
8.2.6.2. Instrumental Information.....	95
8.2.7. Contact Angle.....	95
8.2.8. Dynamic Light Scattering.....	96
8.2.9. Optical Microscopy	96
8.3. Experimental Procedures.....	96
8.3.1. Synthetic Protocols.....	96
8.3.1.1. Synthesis of Pentafluorophenyl Acrylate	96
8.3.1.2. Synthesis of 4-Acryloylbenzophenone.....	97
8.3.1.3. Synthesis of TFA Salt of <i>t</i> -Boc-aminoethyl 2-bromoisobutyrate.....	98
8.3.1.4. Synthesis of 2-Oxo-2-((3-(triethoxysilyl)propyl)amino)ethyl benzodithioate	99
8.3.1.5. Synthesis of Amine-ended PMAA via ATRP.....	101
8.3.2. Fabrication Procedures	102
8.3.2.1. Preparation of Anodic Aluminum Oxide Template (Chapter 4, 5, 6)	102
8.3.2.2. Fabrication of Janus PS- <i>b</i> -PNIPAm Nanorods (Chapter 4).....	102
8.3.2.3. Fabrication of Janus PNIPAm- <i>b</i> -PPFPA Nanorods (Chapter 4).....	103
8.3.2.4. Fabrication of Janus PPYNP- <i>b</i> -PMMA Nanorods (Chapter 4).....	103
8.3.2.5. Silanization of Polyester Film (Chapter 5).....	104
8.3.2.6. Preparation of Pillar-PPFPA (Chapter 5)	104
8.3.2.7. Post-polymerization Modification of Pillar-PPFPA with PMAA (Chapter 5).....	105
8.3.2.8. Preparation of Flat-PPFPA (Chapter 5).....	105
8.3.2.9. Post-polymerization Modification of Flat-PPFPA with PMAA (Chapter 5)	105

8.3.2.10. Immobilization of S-CTA onto AAO Membrane (Chapter 6)	105
8.3.2.11. SI-RAFT Polymerization of Poly(MMA- <i>co</i> -DEAEMA) on AAO Membrane (Chapter 6).....	106
8.3.2.12. Flux experiment (Chapter 6)	107
8.3.2.13. Emulsion Preparation (Chapter 6).....	108
9. Reference.....	109
Appendix	124
List of Abbreviations.....	124
List of Publications.....	127
Conference Contributions.....	127
Acknowledgements	128

1. Introduction

Materials with nanoscale dimension or bearing nanometer-scale structures are defined as nanomaterials.^[1] The implications of nanomaterials refer to various realms including chemistry, physics, biomedical science, energy science and materials science. Not only because of their optimized minute size, nanomaterials also offer distinctive control over their regime of property uniqueness than bulk materials.^[2] Attributing to high research interests, the expectations of technologies emerging from the fabrication of nanomaterials are accreting, which attracted tremendous exploration from researchers worldwide.

In general, methods for fabrication of nanomaterials are divided into two categories: “bottom-up” and “top-down”. The “bottom-up” strategy built up nanomaterials from atoms, molecules, and colloidal particles, while the “top-down” approach applies various methods of lithography to imitate nanostructures.^[3] Template-assisted fabrication techniques stand out amongst lithography nanofabrication methods owing to their cost effectiveness, wide accessibility and the capability of precise scale controllability. Porous templates that are used in nanofabrication, such as ion track etched membranes, anodic metal oxides, macroporous silicon and block copolymer templates,^[4] can not only be used for sacrificial nanopatterning, but the templates themselves are also capable to be employed as fundamental materials for efficient nanofiltration, separation, or storage.^[5] Specially, the anodic aluminum oxide (AAO) template is worthy to be comprehensively investigated by taking advantage of its attractive properties, such as: highly-ordered porous structure, precise dimensional controllability, chemical and mechanical stability, etc. Utterly, the AAO template occupies a decisive position in fabricating nanomaterials.

In this regard, the research presented within this thesis is focused on the preparation of diverse AAO templates and investigating the structure-function relation; furthermore, based on the as-prepared template to fabricate one-dimensional, two-dimensional and three-dimensional nanomaterials via template-assisted nanofabrication. Additionally, this thesis aims to expand the AAO-template-assisted nanofabrication methodology as well as explore diverse nanomaterials that could be fabricated by AAO template-assisted method.

1.1. History and General Remarks

Aluminum is one of the most abundant elements on earth, which is highly used in aerospace industry, transportation and construction.^[6] Aluminum is vulnerable to oxygen and has high oxygen affinity, thus aluminum oxide layers are easy to form on aluminum surface once exposed to oxygen, a phenomenon that is recognized as passivation. The thin oxide layer prevents aluminum from further oxidation and thus hampers the material from graver corrosion.^[7] Besides, corrosive chemicals such as chlorides or sulfates induce local corrosion of metal under aggressive outdoor environment conditions, for example, chloride ions easily penetrate or adsorb by the passive film or even oxide layer which leads to damages.^[8]

Dating back to 1857, Buff was the first who found that aluminum can be electrochemically oxidized in aqueous solution to form a thicker oxidized layer than the oxide layer formed in ambient environment.^[9] This electrochemical oxidation is called anodization because the aluminum part is processed to be the anode in an electrolytic cell. Indeed, 63 years later, this phenomenon was firstly industrialized for the protection of seaplane from etching by corrosive seawater.^[10] Shortly after, the anodization of aluminum was realized for the preparation of porous aluminum oxide for magnetic memory storages and recording devices in 1970. Nevertheless, this porous aluminum oxide was bearing a poor ordering of pores and a limited pore density.^[11,12]

A milestone discovery in the anodic aluminum oxide manufacturing history was reported in the year of 1995. Masuda and Fukuda disclosed fabrication of anodic porous alumina with a highly ordered nanopore arrays via a two-step anodization method for the first time, a method still in use today.^[13] As depicted in Figure 1.1, briefly, after first anodization process, the anodic porous alumina membrane was obtained as disordered porous structure, which is followed by a wet etching to remove the disordered aluminum oxide layer, and respectively leave the hexagonally arranged bug-holes on the top of the remaining aluminum layer. Consequently, after the second anodization procedure, the nanopores are grown from those bug-holes into uniform cylindrical pores.^[14]

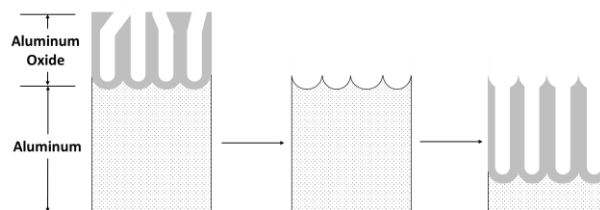


Figure 1.1. Schematic diagram of two-step anodization method for fabrication of porous alumina.

Generally, porous anodic aluminum oxide (AAO) templates, which are obtained from two-step anodization method, are composed of highly aligned cylindrical pores with a thin barrier oxide layer in confocal contact with aluminum substrate.^[15] The cylindrical pores are self-ordered into hexagonal close-packed arrangement forming a honeycomb-like structure, while interrupted at the boundaries (Figure 1.2). Depending on the anodization conditions, the pore diameter, pore density and the pore length could be regulated and controlled. For instance, the range for pore diameter can be attained from 6 nm to 400 nm, while pore densities can reach up to 10^{11} cm⁻², and additionally pore lengths up to 100 μ m are obtainable.^[16–18]

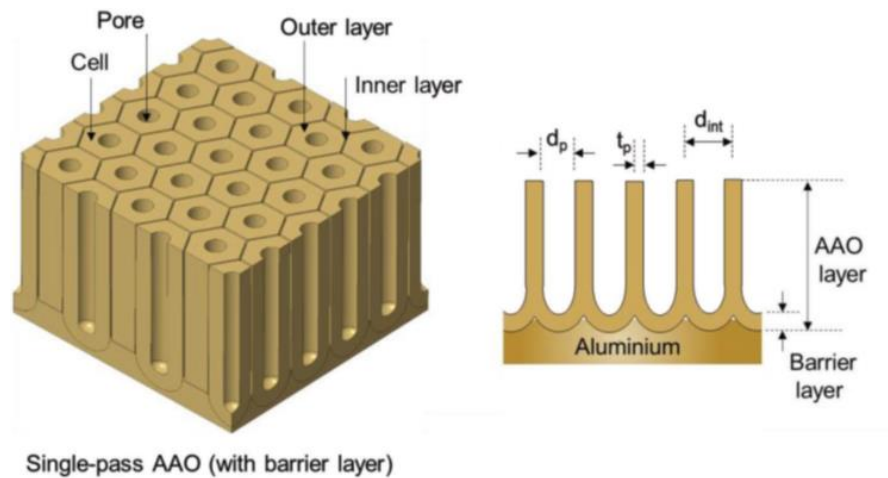


Figure 1.2. Schematic representation of porous anodic aluminum oxide templates. Reprinted with permission from Ref. [19], copyright (2019) John Wiley and Sons.

1.2. Porous Anodic Aluminum Oxide Template

Porous anodic aluminum oxide template, i.e. AAO, as aforementioned, is a self-organized material bearing honeycomb-like structure arranged by cylindrical pores. Owing to the uniform nanostructure, in addition to their highly thermal, mechanical and organic chemical resistance as well as the low fabrication cost, AAO templates have attracted plenty of interest in the field of nanotechnology, specifically for the fabrication of nanorods, nanodots, nanotubes, nanopillars as well as for the development of functional nanocomposites, such as: sensors, optical- and electrical-devices, smart surfaces and filtration membranes, etc.^[20]

1.2.1. Types of Anodic Aluminum Oxide Template

The anodic aluminum oxide template is mainly divided into two categories depending on the morphology, known as barrier-type film and porous-type film.^[21] A barrier-type film is characterized by low porosity, which is formed in neutral electrolytes, such as borate, oxalate, citrate, phosphate, adipate and tungstate. In those neutral electrolytes, the formed oxide is mostly insoluble. On the contrary, the porous-type film is formed in acidic electrolytes, e.g. selenic acid, sulfuric acid, oxalic acid, phosphoric acid, chromic acid; additionally, the formed oxide is slightly soluble in those acidic electrolytes. Besides, barrier-type and porous-type templates are also differing in the context of their respective oxide growth kinetics. Figure 1.3 demonstrates the oxide growth kinetics of barrier-type and porous-type AAO under potentiostatic condition. As illustrated, fabricating of barrier-type AAO upon potentiostatic condition, current density (j) declines exponentially with the time (t). As reported, the thickness of barrier-type film is directly proportional to the practical voltage. Therefore, the film growth rate is declining practically with time, which leads to a limitation of the thickness growth of the barrier-type AAO membrane. On the contrary, for the porous-type AAO template, the current density is kept constant. Thus the thickness is linearly propagating to the total amount of charge (i.e. anodization time) of the electrochemical reaction.^[20]

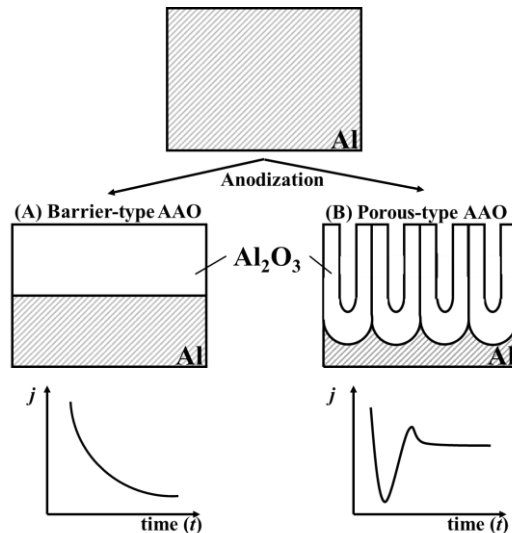


Figure 1.3. Respective current (j) - time (t) transients under potentiostatic condition of (A) barrier-type and (B) porous-type anodic aluminum oxide. Reproduced with permission from Ref. [20], copyright (2014) American Chemical Society.

1.2.2. Electrochemical Principles during Anodic Aluminum Oxide Template Fabrication

Electrochemical reactions during anodic aluminum oxide template fabrication process are schematically illustrated in Figure 1.4. Upon anodization operation, Al^{3+} cations are first formed at the metal/oxide interfaces from Al at the anode. In the meantime, ionization of H_2O occurs and result in formation of O^{2-} anions and H^+ cations. Under high electric field, the mobile Al^{3+} cations are able to penetrate into anodic oxide layer, while, O^{2-} anions move towards the metal/oxide interface under the promotion of external electric field. When dissociative Al^{3+} cations and O^{2-} anions bump into each other, Al_2O_3 are formed. Critically, only 70 % of Al^{3+} cations will react with O^{2-} anions and the remaining Al^{3+} cations will dissolve in the electrolyte phase. Besides, dissociated H^+ will not only react with the formed Al_2O_3 , but will also move to the cathode and be reduced into molecular hydrogen.^[20,22]

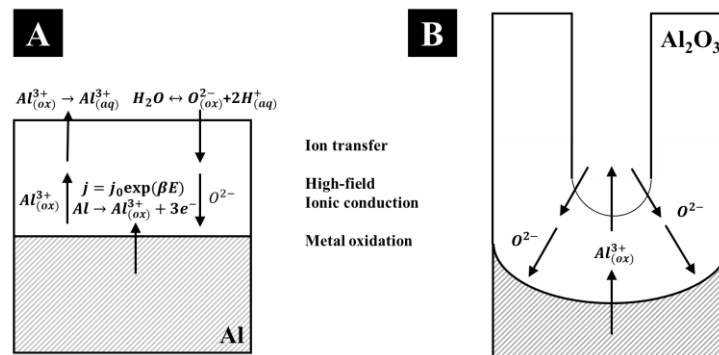


Figure 1.4. Schematic diagram of elementary interfacial reactions for (A) barrier-type and (B) porous-type anodic aluminum oxide. Reproduced with permission from Ref. [20], copyright (2014) American Chemical Society.

The following reactions^[23–25] are considered to be possibly occurring at the interfaces:

- (i) At the metal/oxide interfaces:



- (ii) At the oxide/electrolyte interfaces:

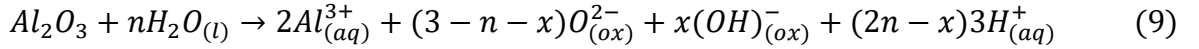




In conclusion, the anodic oxidation of aluminum in an electrolyte can be written as:



The overall reaction at the oxide/electrolyte interfaces could be ascribed as follows:



Where n indicate the amount of water dissociated per mole of Al_2O_3 which is dissolved simultaneously; x denotes the ratio of oxide anions of O^{2-} and OH^{-} .

Although the formed Al_2O_3 layer will be simultaneously dissolved by the electrolyte during electro-oxidation, the dissolving kinetics are far below the kinetics of forming the Al_2O_3 layer, hence resulting in the accumulative growth of an Al_2O_3 layer.^[26]

1.2.3. Pore Formation Mechanisms

The self-ordering pore formation process of aluminum during anodization can be categorized into four main stages, which are schematically demonstrated in Figure 1.5 A, while Figure 1.5 B shows change of current density during anodization process.

Commonly, in the first stage (I in Figure 1.5 A), a compact barrier oxide layer is formed between the aluminum surface and electrolyte under constant voltage. The formed oxide layer leads to an increase of the aluminum surface resistance, which further induces a significant decrease of the current density. Additionally, the distribution of the current density between oxide barriers is highly depending on the surface roughness of the oxide layer. A rough oxide surface results in a local decline of the current taking place between oxide layer and electrolyte, which synchronously results in a locally focusing of the electric field (E) (Stage II in Figure 1.5 A).

According to the high-field conduction theory proposed by Güntherschulze and Betz,^[27,28] anodic oxide is grown under high field condition and the ionic current density (j) is associated with the movement of charged ions in the barrier oxide as well as the electric field (E), which is written as:

$$j = j_0 \exp(\beta E) = j_0 \exp(\beta \Delta U / t_b) \quad (10)$$

Where j_0 and β are material-dependent constants at a given temperature; ΔU is potential drop, i.e. also the effective electric field impressed on the barrier layer; t_b is the thickness of the barrier layer.

From equation (10), we can conclude that, initially, the electric field of aluminum oxide layer was evenly dispersed, and upon the increment in the thickness of barrier layer during the anodization process, their current density decreased, which is in accordance with the results from stage I of Figure 1.5 A.

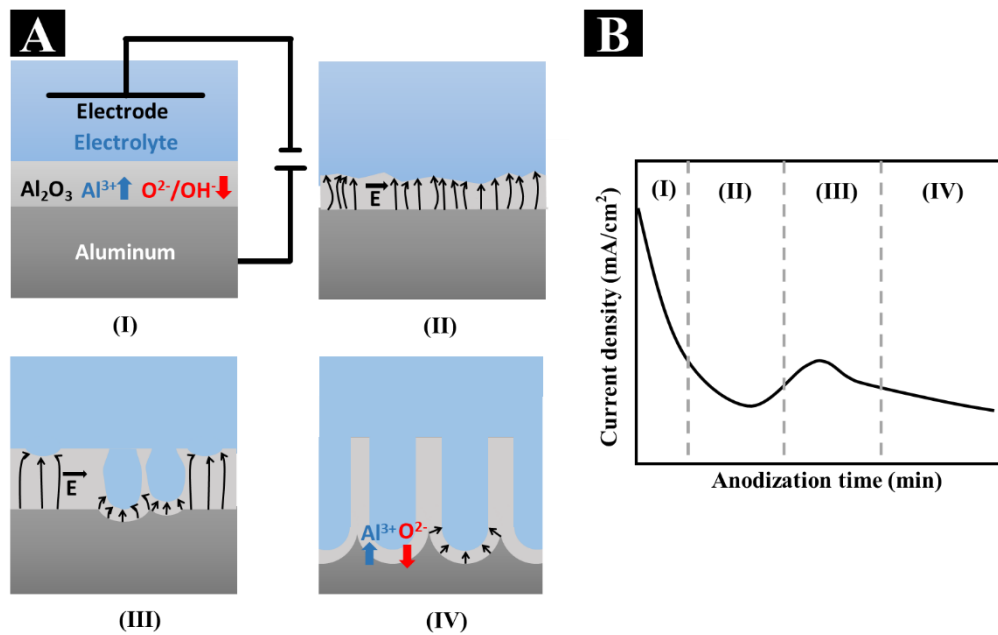


Figure 1.5. Schematic diagram of (A) stages of pore growth: (I) formation of oxide layer; (II) formation of pits by local electric field heterogeneities; (III) initial pore formation; (IV) pore growth under steady-state conditions; and (B) typical current density curve of electrochemical anodization. Reproduced with permission from Ref. [29], copyright (2013) Elsevier.

In fact, acidic electrolyte causes erosion of aluminum oxide layer, and results in the formation of tiny cracks at the interface between the oxide layer and the electrolyte. The formed cracks are also called as penetration paths. As shown in Figure 1.6, in the beginning, the electric field and current density were distributed homogenously across the flat aluminum oxide layer (Figure 1.6 a). After forming the penetration path, the electric field and current density underneath are focused and enhanced owing to the incrustation of aluminum oxide layer (Figure 1.6 b). Subsequently, a local

Joule heating effect occurred, which further accelerated dissolving of the oxide layer, hence the penetration paths developed into readily recognized pores (Figure 1.6 c). To sum up, the penetration process illustrates the reaction that happened in stage III from Figure 1.5 A.

The growth rate of pores is determined by the competition between the generation and dissolution velocity of aluminum oxide. Specifically, after forming of aluminum oxide pores, Al^{3+} will keep dissolving owing to the heterogeneous distribution of the electric field and current density below the pores. This phenomenon reveals that before reaching a stable state during pore growth, the rate of aluminum oxide dissolution is higher in comparison to that of its generation, thus further raising the current density. When the pore growth reaches a certain degree, the electric field and ionic current are locally focused in the barrier layer under the pores. Meanwhile, the current localizes between the aluminum and barrier layer, which induces the barrier layer to form semicircular grooves. Gradually, the rate difference of aluminum oxide dissolution and generation decreases. Ultimately, the rate of aluminum oxide dissolution and generation will become the same, therefore reaching a dynamic equilibrium.

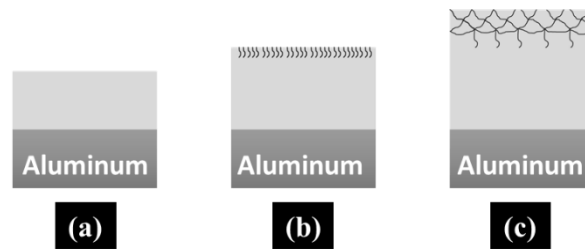


Figure 1.6. Schematic diagram demonstrating the development of penetration paths during the anodization process. Reproduced with permission from Ref. [30], copyright (1997) Elsevier.

Under the aforementioned situation, the current density will be constant, while the thickness of the barrier layer will remain unchanged. Accordingly, oxidation of aluminum will occur under the formed pores, hence the development of aluminum oxide will be in the vertical direction, which is perpendicular to the pores (stage IV in Figure 1.5 A). During oxidation process, owing to the variations in the electronic density, the volume expands upon transformation from aluminum into aluminum oxide. Attributed to the jostle of expanded pores, cylindrical pores will eventually pile up as the most efficient way and form a uniform distributed hexagonal packing. Meanwhile, along with the anodization time, hexagonal cells are arranged regularly, and ultimately form close-packed porous arrays.^[29–31]

1.3. General AAO Template Fabrication Method and Experimental Set-up

Self-ordered anodized aluminum oxide templates are fabricated by a general two-step anodization process, which mainly consists of four working steps (Figure 1.7). Roughness on the aluminum surface will induce current localization during anodization process, which will further lead to aluminum burning or breakdown, and eventually end up with heterogeneously arranged porous structures. Hence, electro-polishing step before the anodization is essential. Electro-polishing is carried out in a highly ionic solution. Under constant voltage the irregular protuberances or sharp points on aluminum surface are electrically oxidized and subsequent dissolved in the electrolyte under the effect of high pronounced charge concentration. After electro-polishing, a thin layer of undesired material on the aluminum surface is removed, leaving superior smooth and optically clean appearance.

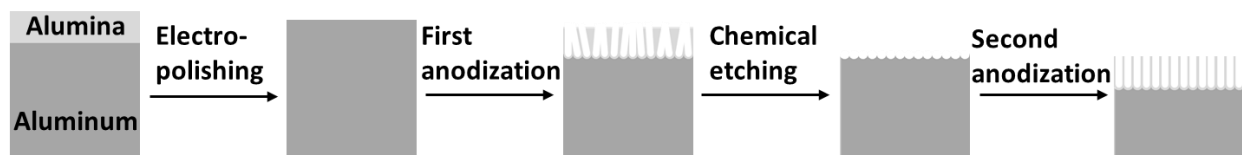


Figure 1.7. Schematic illustrations of working procedures for AAO template fabrication.

During the first anodization process, the electro-polished aluminum discs are installed as the anode, while platinum wires as the cathode, respectively. Upon anodization, a thin alumina layer will first form on the aluminum metal surface. Under the influence of the Joule effect, the aluminum oxide layer between aluminum and electrolyte will be dissolved, subsequently transformed into pore pit structures, which eventually grow into separated pores. However, the randomly formed pit structures will grow into irregularly distributed cylindrical pores. In order to solve this problem, a second anodization step should be carried out. Moreover, prior that, a chemically etching step has to be processed in between to remove the formed irregular alumina pores and leave only regularly arranged shallow grooves. Afterwards, a second anodization starts from the pits left from etching, each cave acts as a nucleation center that is growing into well-arranged pore structures in the course of the anodization.

The experimental device for the fabrication of well-ordered AAO template is schematically illustrated in Figure 1.8. Basically, the set-up consists of a two-electrode system which is driven by computer programmed power supply. Upon anodization, aluminum discs are inserted between

PVC electrolyte container and a copper plate that is connected to the anode of the power supply. A metal lid with a stirring head and a woven Pt wire net is covered on top of the PVC cell. The Pt wire is linked to the cathode of the power supply. During anodization, the whole chamber is placed on a cooling plate that is connected with a recirculating chiller and the electrolyte is continuously agitated by the stirrer. Depending on the desired dimension of AAO template, various type of electrolytes and corresponding voltage are applied.

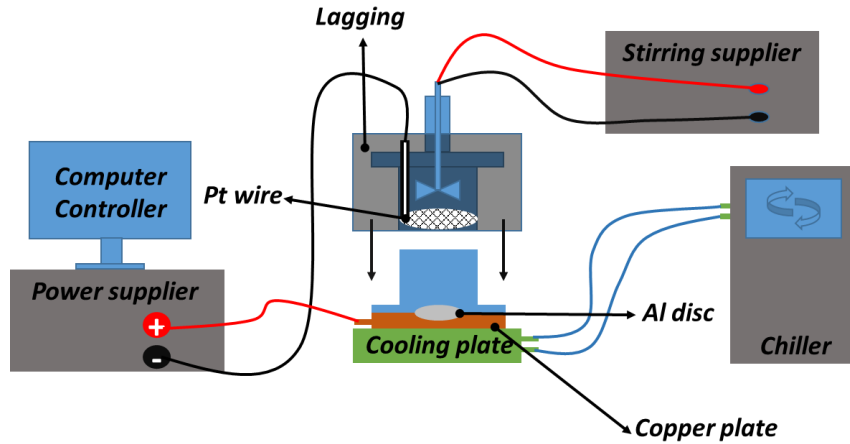


Figure 1.8. Schematic experimental set up for the fabrication of AAO template.

1.4. Controlled Parameters of AAO Template Pore Density

AAO template pore density can be controlled by adjusting the type of electrolyte solution and applied voltage. The interpore distance is in a linear relationship with the applied voltage, while the pore diameter is controlled by the type of the electrolytes.^[32–35] Upon anodization, aluminum metal is oxidized into alumina. Owing to the compressive stress by volume expansion during this process at the entire metal/oxide interface, the material expands in vertical direction that should lead to mutually extruding of formed nanopores, as a consequence, pores are presenting the densest hexagonal closed-packed arrangement.

1.4.1. Pore Diameter

It is reported that the pore diameter is linearly proportional to the applied voltage.^[36] Besides, the pore diameter is also dependent on the anodization temperature and anodization time owing to the dissolution of pore wall by applied electrolyte during pore growing process.^[37] In addition, diameter of pores can be further enlarged in acidic solution after anodization, i.e. typically in the presence of aqueous H₃PO₄. Typically, pore diameters of AAO templates could range from 25 nm to 400 nm depending on the electrolyte (H₂SO₄, H₂C₂O₄, H₃PO₄) and subsequent pore widening process. Interestingly, synthesis of ultrathin AAO templates with pore diameter lower than 20 nm is also achievable. Indeed, by anodizing in selenic acid at 48 V, AAO templates with 10-nm-scale-pores are obtained.^[38]

1.4.2. Pore Length

The pore length of AAO template is proportional to the total amount of electrons and generally vary from tens of nanometer to hundreds of micrometer, which is precisely controlled by the working time during second anodization process. Under mild anodization condition, the growth rate of nanopores in AAO template is almost fixed from 1 to 10 $\mu\text{m}/\text{h}$ based on different electrolytes as shown in Table 1.1.

Table 1.1. Experimental conditions of aluminum anodization in sulfuric, oxalic and phosphoric acid electrolytes, and corresponding obtained interpore distance and pore diameters. Reproduced with permission from Ref. [39], copyright (2012) Elsevier.

<i>Electrolyte</i>	<i>Concentration</i>	<i>Voltage</i> (V)	<i>Temperature</i> (°C)	<i>1st</i> <i>anodization</i> <i>time (h)</i>	<i>Growth</i> <i>rate</i> ($\mu\text{m}/\text{h}$)	<i>Interpore</i> <i>distance</i> (nm)	<i>Pore density</i> (pores/cm ²)
<i>H₂SO₄</i>	<i>0.3 M</i>	<i>25</i>	<i>1~8</i>	<i>16~48</i>	<i>2.5</i>	<i>25~55</i>	<i>3 × 10¹⁰</i>
<i>H₂C₂O₄</i>	<i>0.3 M</i>	<i>40</i>	<i>1~8</i>	<i>16~48</i>	<i>1.9</i>	<i>40~85</i>	<i>1 × 10¹⁰</i>
<i>H₃PO₄</i>	<i>1 wt%</i>	<i>195</i>	<i>1~2</i>	<i>16~20</i>	<i>5</i>	<i>180~400</i>	<i>5 × 10⁸</i>

1.4.3. Interpore Distance

Interpore distance is governed by the applied voltage and it has a substantial linear relationship with anodizing potential. Typically, pore density of AAO template is ranging from 10^8 to 10^{10} cm^{-2} that could be obtained from three major pore-forming acid electrolytes, which are listed in Table 1.1. For instance, by using 0.3 M sulfuric acid as electrolyte under 25 V voltage, the interpore distance of formed AAO template is 25~55 nm and with a pore-density of 3×10^{10} pores/ cm^2 . On the other hand, when anodizing at 40 V in 0.3 M oxalic acid, a lattice of 40~85 nm is obtained, while the pore-density is decreased to 1×10^{10} pores/ cm^2 . Higher interpore distance of 180~400 nm are obtained in the presence of 1 wt% phosphoric acid at 195 V with a comparatively lower pore-density of 5×10^8 pores/ cm^2 . Besides, smaller interpore distance as low as 13 nm are accessible by combination of colloidal lithography strategy with general anodization.^[40]

1.4.4. Complex Internal Pore Architectures

It has been discussed above that the pore diameter and interpore distance are depended on the nature of the electrolyte solution and the applied voltage during the anodization. Hence, by manipulating the type of electrolyte, electrolyte concentration and varying the anodization voltage or current, or combining anodization and chemical etching, AAO templates with complex internal pore architectures can be prepared. Complex hierarchical AAO templates have great application prospective in the development of molecular separation membranes, sensing platforms as well as for the fabrication of baroque nanostructures.^[41]

In fact, Li *et al.* reported the fabrication of Y-shaped AAO template for the first time in the year of 1995. The first anodization was carried out in 0.3 M oxalic acid under 50 V for 15 h at 10 °C, after chemical etching, a second anodization step was carried out under the same condition to produce primary stem pores for 30min, followed by reducing the anodization voltage by a factor of $1/\sqrt{2}$ to 35 V. Because the pore diameter is proportional to the anodization voltage, by reducing the anodization voltage, twice as many pores appeared in order to keep the original surface area. The latter led to the formation of branched pores, thus Y-shaped pores were obtained. Additionally, have utilized the obtained Y-shaped AAO template for the fabrication of Y shaped carbon nanotubes, which paves the way for the development of molecular-scale electronic devices.^[42]

Based on this, Ajayan *et al.* discovered that by reducing the voltage with factor of $1/\sqrt{n}$, n -branched pores of AAO membrane will be obtained. Furthermore, by combination of Y-shape and multiple branches, more complex architectures can be further constructed. For example, as demonstrated in Figure 1.9, by reducing the voltage factor of $1/\sqrt{2}$ and then followed $1/\sqrt{n}$ reduction, AAO membrane with first Y shaped branch and then n shaped branch will be obtained. The sequences can be interchangeable and thus facilitating the design of versatile branched structures. However, as a limitation of the pore size of using oxalic acid, if the voltage needs to be reduced lower than 25 V, sulfuric acid could be used as replacement for further branching.^[43]

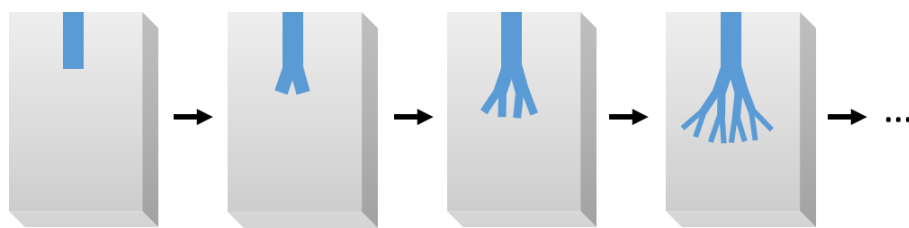


Figure 1.9. Schematic fabrication of branched AAO template. Reprinted with permission from Ref. [43], copyright (2005) National Academy of Sciences.

Except branched internal pore architectures, AAO membrane with periodic diameter-modulation in the pore structure could also be fabricated by varying the anodization condition. Lee *et al.* discovered the fabrication of highly uniform periodic modulations in pore diameter by alternatively utilizing low field (mild anodization, MA) and high field (hard anodization, HA) anodization process, so called “pulse anodization” (Figure 1.10 A). By means of applying low current pulses with consequent short high current pulses for two consecutive process, the periodic nanostructure of AAO membrane was prepared.^[44]

Similarly, by adopting the same alternative anodization process, Dusan *et al.* have prepared periodic modulated pore geometries with complex pore architectures. However, they slow down the change of anodization condition, which results in a transition anodization (TA) mode that is formed between MA and HA. During TA process, the current density and the slow variation of anodization mode allow for the controlled design of pore geometries (Figure 1.10 B).^[45] Although it has been wildly reported in the development of strategies for the design of complex pore architectures, the investigation for preparing sophisticated AAO template will not stop.

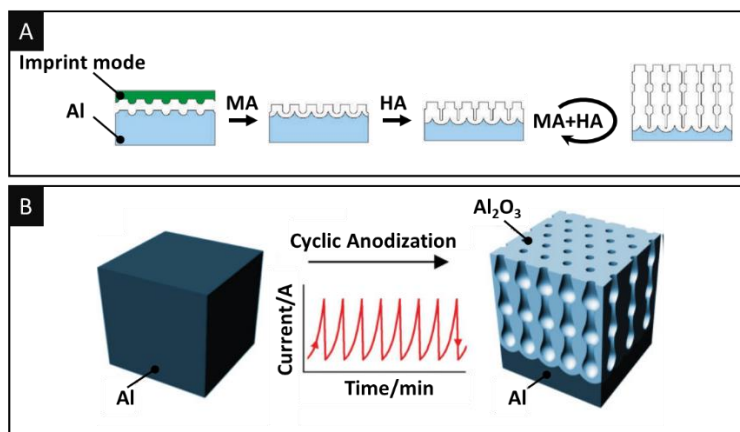


Figure 1.10. Scheme for fabrication of (A) AAO with modulated pore diameter by combination of MA and HA. Reprinted with permission from Ref. [44], copyright (2006) Springer Nature. (B) AAO membrane with shaped pore geometry from cyclic anodization strategy. Reprinted with permission from Ref. [45], copyright (2009) John Wiley and Sons.

1.5. AAO template Assisted Fabrication of Polymer Nanostructures

AAO templates bearing well-ordered porous structures and large surface areas with precise controllability over their dimensions allow for patterning of ordered nanostructures with relatively narrow diameter distribution. Additionally, as aforementioned, AAOs display high thermo-stability up to 600 °C without collapsing, on the other hand, they could be easily dissolved by acidic or alkaline solution to release the formed nanostructure without affecting the infiltrated materials. Thus, AAO templates are recognized as an attractive platform for fabrication of nanostructures.

Depending on the infiltration technique as well as the infiltration conditions, solid or hollow nanocylinders could be obtained which in turn results in the formation of nanorod, nanotube, nanosphere, nanocapsule or complicated nanostructures. Currently, the most commonly used methods for porous infiltration are template wetting, polymerization, layer-by-layer assembly, and electrochemical deposition, amongst others. Accordingly, some of these approaches will be described more in details within the following sub-chapters.

1.5.1. Melt Template Wetting

Melt wetting process was first raised by Steinhart *et al.* for the preparation of poly(tetrafluoroethylene) nanotubes.^[46] The basic operating principle of melt template wetting strategy is as follows: a porous membrane loaded with desired polymer film on top was preheated above the glass transition temperature of the given polymer. Upon heating, polymer chains are gaining enough mobility inducing long-range coordinated molecular motion, which in turn is leading to a capillary force polymer wetting into porous cavities, and accordingly nanostructures are formed and solidified upon cooling within the template cannula. The possibility of melt polymer wetting could be considered for the infiltration of precursor polymer films. From the research of Martin and Mijangos, it has been concluded that depending on the template pore diameter and precursor film thickness, the morphology of obtained nanostructure could be adjusted.^[47] If the thickness of the precursor film is larger than the nanopore radius, solid nanofiber or nanorod will be obtained. On the contrary, when nanopore radius is larger than polymer film thickness, hollow nanotubes are fabricated. Additionally, temperature plays a crucial role in tailoring polymeric nanostructures from nanorods to nanotubes in the melt wetting process. Zhang *et al.* had systematically studied the transition from partial to complete wetting of polystyrene (PS) melts via controlling annealing temperature for preparation of one dimensional PS nanorods and nanotubes.^[48] As a consequence, by varying the preparation condition, polymer nanostructures from solid to hollow structures could be fabricated through melt wetting. However, the melt wetting method has a limitation that all the polymers used for melt wetting should have a high thermo-stability.

1.5.2. Solution Template Wetting

As a complementary approach to melt wetting strategy, solution wetting has been developed. In fact, the solution wetting method is one of the simplest methods to achieve template polymer infiltration. The very first step of the solution wetting process is to dissolve the polymer in a proper solvent to form a homogenous solution. Subsequently, the AAO membrane is immersed into the polymer solution or the prepared polymer solution was deposited onto the AAO membrane, so that the polymer solution can penetrate into nanopores of AAO membrane due to the capillary force. Consequently, solvent evaporation occurs and desired nanostructures will be molded inside the

porous template. For instance, Wendorff *et al.* investigated the wetting approach for the preparation of cylindrical nanostructures from PS solution.^[49] Accordingly, they postulated that for the formation of nanostructures from AAO template via solution wetting method, the solvent of choice and the concentration of the polymer are of particular importance. Poor solvent media or low polymer concentrations result in instable cylindrical structures. Only upon good solvent conditions and sufficient polymer concentrations, stable cylindrical nanostructures are obtained. Additionally, polymer molecular weight influences the obtained types of structures. With low molecular weight polymers, nanotubes are accessible, while with high molecular weight polymers solid nanostructures are achieved.

In another example, it was shown that solution wetting method also enabled the preparation of versatile and complex nanostructures. Respectively, Chen *et al.* have demonstrated the fabrication of nanostructures varying from nanoparticle, to nanorods, nanowires, nanofibers, and hollow nanotubes by solution wetting of AAO template, as depicted in Figure 1.11.

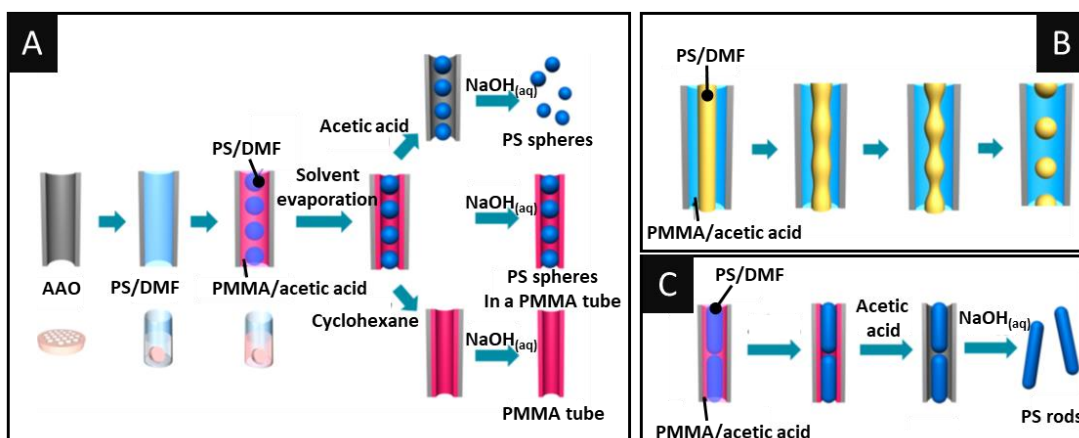


Figure 1.11. (A) Schematic illustration of preparation of PS/PMMA nanopeapots, (B) proposed model of mechanism during formation of PS/PMMA nanopeapots via double-solution wetting strategy, (C) graphical illustration of fabrication of PS/PMMA nanostructures with PS nanorods as core. Reproduced with permission from Ref. [50], copyright (2014) American Chemistry Society.

By infiltration of low concentration poly(methyl methacrylate) (PMMA)/acetic acid solution into AAO membrane, PMMA nanotubes could be obtained. Attributing to the high affinity of PMMA/acetic acid to the aluminum oxide wall and a fast solvent evaporation as well as appropriate polymer concentration promote the formation of nanotubes. Additionally, by controlling the

evaporation of polymer solutions within the nanopores, core-shell nanopods were obtained. In detail, PMMA/acetic acid solution and polystyrene/DMF solution were successively drop casted onto the AAO membrane. Compared with PMMA/acetic acid solution, PS/DMF solution revealed less affinity to the pore wall of AAO template, hence PS/DMF solution tends to isolate from PMMA/acetic acid solution. Subsequently, driven by the Rayleigh-instability transformation and the evaporation of the solvent, PS nanosphere or nanorods were formed inside the PMMA shell, resulting in a nanopods structure.^[50]

Nevertheless, the solution template wetting method is limited to the solvent that solubilize the polymers with appropriate viscosity, which further allows them to flow through the AAO nanopores. Therefore, in order to cope with all kinds of polymer materials, diverse methods besides wetting strategy have been raised for nanomaterials fabrication.

1.5.3. Polymerization in AAO Template

For the preparation of polymeric nanostructures from AAO template, the *in situ* polymerization of monomers in nanopores has been suggested as an efficient and convenient method. This approach also facilitates the possibility of investigating polymerization kinetics, and respectively modeling the reaction under confinement media. Dating back to 1994, *in situ* polymerization within the pores of porous template membrane for constructing polymeric nanostructure was first addressed.^[51] However, the kinetics of *in situ* polymerization, which is of particular important for well production of nanostructures, have only been recently studied. Sanz *et al.*, who had explored the free radical bulk and *in situ* polymerization of methyl methacrylate under ambient environment and confinement within the nanopores of AAO template, respectively.^[52] The results revealed that, compared with bulk polymerization, polymerization kinetics within the AAO nanopores during *in situ* polymerization are significantly faster, while the obtained corresponding molecular weight is lower. The reaction kinetics are schematically illustrated in Figure 1.12.

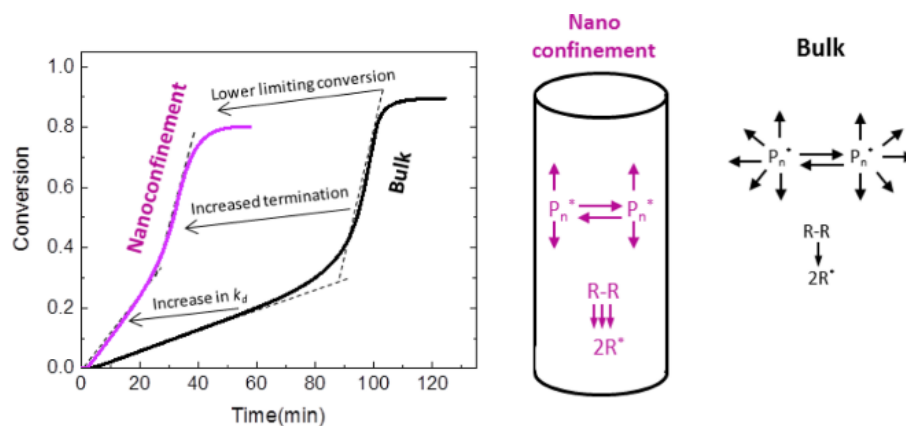


Figure 1.12. Schematic illustrating of reaction kinetics of MMA in bulk and under nanoconfinement (60 nm) at 60 °C. Reprinted with permission from Ref. [52], copyright (2017) American Chemical Society.

Owing to the high catalytic effect of AAO pore walls on decomposition of initiator, a faster polymerization rate is observed. Besides, unlike bulk polymerization, the decomposed initiators are restricted to move freely leading to a higher rate of termination. As a consequence, compared with polymer synthesized in bulk, the confined reaction volume and high rate of termination lead to lower molecular weight and reduced dispersity of polymers formed in AAO membrane.

Besides free radical polymerization, a large variety of polymerization methods, such as atom transfer radical polymerization (ATRP) could also be carried out within the nanopores of AAO template.^[53] For instance, Cui *et al.* had synthesized poly(*N*-isopropylacrylamide) (PNIPAm) nanotubes from AAO membrane via surface-initiated ATRP (SI-ATRP) strategy as illustrated in Figure 1.13. In detail, the ATRP initiator, 2-bromoisobutyrylbromide (BIBB), was firstly immobilized onto AAO membrane; further polymerization of NIPAm was carried out starting from the initiating site on the AAO wall. Meanwhile, in order to maintain the stability of obtained nanostructure, *N,N'*-methylenebisacrylamide (MBAA) was also introduced as crosslinking agent. Ultimately, after dissolving AAO membrane in aqueous sodium hydroxide, P(NIPAm-*co*-MBAA) nanotubes were obtained. Via tuning membrane pore size, nanotubes with diverse diameters are accessible. Additionally, shape variation of P(NIPAm-*co*-MBAA) nanotubes upon temperature transition enabled them to be applied as temperature-sensitive drug or catalysts carriers.^[54]

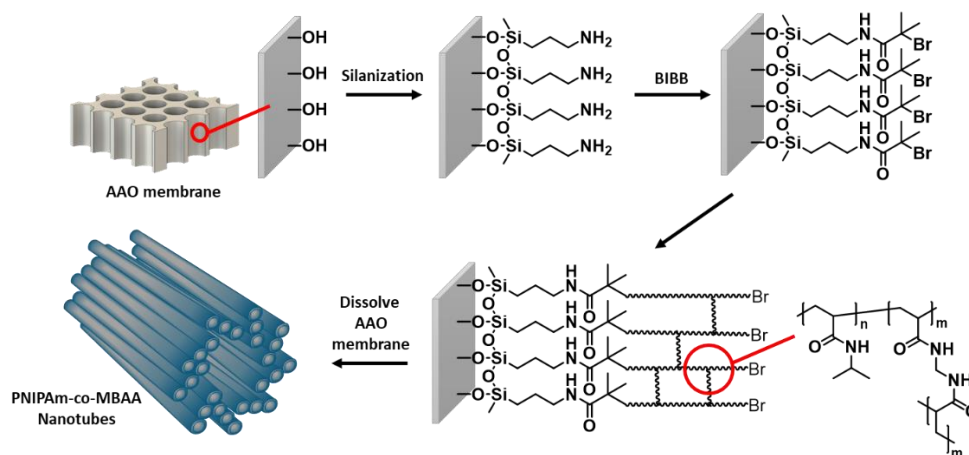


Figure 1.13. Synthesis of *P(NIPAm-co-MBAA)* nanotubes in AAO membrane via SI-ATRP. Reprinted with permission from Ref. [54], copyright (2005) John Wiley and Sons.

1.5.4. Layer-by-layer Assembly

Layer-by-layer (LbL) assembly of polymer materials within the cylindrical pores of AAO membrane is also a commonly used method for the preparation of nanostructures, especially nanotubes.^[55] The formation principle is based on multiple intermolecular interactions such as electrostatic contacts, hydrogen bonding and hydrophobic interactions.^[56] For instance, Li *et al.* had synthesized nanotubes by alternatively pressurized injection of negatively charged poly(sulfonated styrene) polyelectrolyte and positively charged poly(allylamine hydrochloride) polyelectrolyte solution into the nanopores of AAO membrane.^[57] Upon electrostatic adsorption, LbL deposition was realized and multilayers of polyelectrolyte were formed on the inner walls of the membrane as revealed in Figure 1.14.

Intriguingly, the nanostructure dimension could be tuned by the variation of polymer molecular weight and chain conformation; besides, owing to the charged characteristic of polymers used in LbL strategy, such as poly(ethyleneimine) (PEI), poly(allylamine) (PAH), poly-(diallyldimethylammonium chloride) (PDADMAC), poly(styrenesulfonate) (PSS), poly(vinylsulfate) (PVS), and poly(acrylic acid) (PAA),^[58] various functional molecules such as biomolecules and/or nanoparticles could be entrapped into the LbL assembled nanotubes, thus enabling the nanostructures to be applied as biosensors and catalytic membranes.^[59,60]

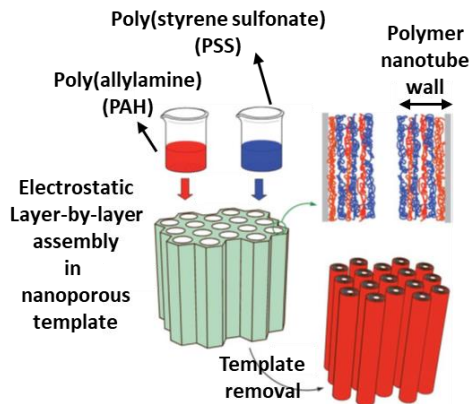


Figure 1.14. Simplified representation of the formation of polyelectrolyte nanotubes through sequential assembly of polycations and polyanions inside nanoporous template. Reprinted with permission from Ref. [61], copyright (2011) Royal Society of Chemistry.

1.5.5. Electrochemical Deposition

Compared with a chemical deposition method, the electrochemical deposition method is bearing an advantage since the growth rate and the dimension of nanomaterials could be easily adjusted. Nevertheless, the approach is generally restricted to fabrication of conductive polymer materials. Generally, for a typical electrochemical synthesis, the barrier layer and remaining Al layer on AAO membrane should be removed, and sputtered with conductive metal. Subsequently, the template is attached to cathode, and brought into contact with the deposition solution, in which the anode is placed in. When the electric field is applied, cations diffuse towards, and are reduced at the cathode, which in turn leads to the electrodeposition of polymers from the bottom. After dissolving of the template, free standing nanorods or nanotubes are obtained, which are attached on the conductive substrate.^[62] By adopting this electrochemical deposition strategy, Duay *et al.* had prepared polyaniline, polypyrrole and poly(3,4-ethylenedioxythiophene) (PEDOT) nanostructures from AAO membrane.^[63] Additionally, polymer-metal hybrid materials, segmented or core-shell nanostructures could also be fabricated via sequentially electrochemical deposition of desired materials in AAO membrane.^[64,65] As reported, the obtained conductive nanomaterials are showing great potential in the field of energy application.^[66]

1.6. Polymeric Nanoarrays via AAO Templating

Well defined and ordered nanostructures have gained tremendous attention owing to their potential application in preparing biomimic materials, electronic, optical and sensing devices, etc.^[67] AAO templates bearing well ordered nanopores as well as tunable pore size and pore architecture are found to be a non-negligible candidate for the use in template-assisted nanopatterning.^[68] The confinement effect of AAO membrane on nanostructures leads to a change in performance compared to bulk materials, such as the preferential orientations of crystals, tunable T_g , enhanced chain diffusion, etc., in consequence varying the application of obtained “patterned materials”. Additionally, as summarized in the last section the preparation methods can be adopted for the fabrication of one-dimensional nanostructures via AAO template and in similar way this is true for the preparation of polymeric nanoarrays. Hence, this section focuses on reviewing the application fields ranging from adhesion surface, optical device, smart responsive materials to bio-related applications of fabricated polymeric nanoarrays from AAO templating.

1.6.1. Dry Adhesion and Hydrophobic Surfaces

In general, AAO membranes offer the opportunity to fabricate highly aligned nanostructured films, which could be used as functional structured solid surfaces with super wettability for potential industrial applications. However, for the fabrication of high-performance films only unitary nanostructures are woefully inadequate, structural features such as pillar size, aspect-ratio, tip shape, tilting angle, and hierarchical structures should also be considered.^[69–73] For example, the aspect ratio and hierarchical structures are particularly important for enhancing the film adhesive and frictional properties. Jin *et al.* had reported for the first time on utilizing AAO template for patterning of aligned polystyrene nanotubes.^[74] Owing to the highly packed and well-arranged pores in AAO membrane, the obtained well-ordered film consists of more than 6 000 000 nanotubes per square millimeter, which in turn can generate higher van der Waals’ forces leading to a strong adhesive force against water droplets and thus demonstrate superhydrophobicity.

Another example is inspired by nature. As reported, geckos are able to freely climb on all kinds of surfaces owing to their unique feet which are composed of hundreds of spatula that covered with microscaled keratinous setae. In addition to their reversible solid-solid adhesion property, geckos’ feet also show a superhydrophobicity. The wetting behavior of solid surfaces is very important

leading to a wide variety of applications in all fields. Hence, in order to precisely re-create the architecture of geckos' feet, fabrication of a multi-branched porous AAO membrane as revealed in Figure 1.15 was considered.

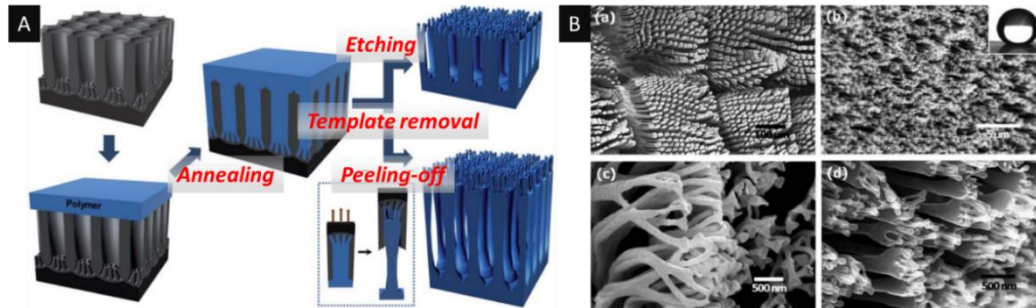


Figure 1.15. (A) Schematic illustration of the process for fabricating hierarchical nanohairs, (B) SEM images of (a, c) Tokay Gecko nanohairs and (b, d) hierarchical PS nanohairs peeling-off from AAO. Reprinted with permission from Ref. [75], copyright (2012) Royal Society of Chemistry.

The multi-branched AAO membrane was prepared by a typical two-step anodization, and subsequent barrier layer thinning process. Lee *et al.* had prepared hierarchical nanohair layers from the branched AAO membrane through a replica nanoyielding process. The fabrication procedure is depicted in Figure 1.15 A. Accordingly, the obtained hierarchical surface revealed substantial similarity to the geckos' feet structure (Figure 1.15 B). Consequently, AAO templating provides a simple and versatile route for the fabrication of artificial geckos' feet, which can be further used as dry adhesives.^[75]

Additionally, by altering the tip structures of nanoarrays, adhesion forces would also be controlled. In order to re-structure the terminal shape of nanopillars and further optimize the adhesion property, Xue *et al.* investigated a post-shaping strategy.^[76] In general, stiff polymer nanorods were fabricated via replication of AAO membrane, further the barrier layer was removed and a membrane with opened bottom was obtained. Subsequently, cold, hot or shear pressing was carried out in order to prepare nanopillar arrays with diverse tip architecture from flat to foot-like or pancake-like tips. After removing the whole template, films bearing different structured nanorod arrays were achieved as revealed in Figure 1.16 A. The results of adhesion force for obtained functional surfaces are illustrated in Figure 1.16 B, as a consequence, the flat surface shows the lowest adhesion force, foot-like tips exhibit moderate adhesion force and pancake-tip surface presents highest adhesion force.

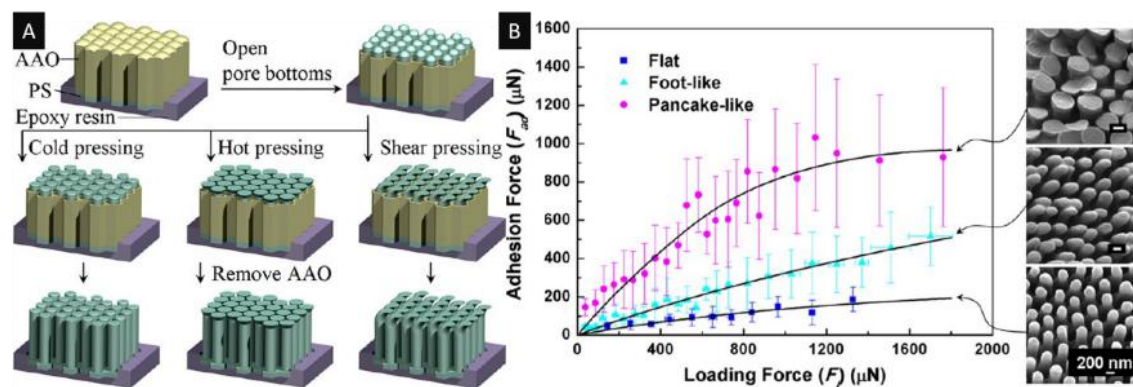


Figure 1.16. (A) Illustration of the shaping of PS nanorod tip, (B) adhesion force for nanorod arrays with different tips and the corresponding SEM images. Reprinted with permission from Ref. [76], copyright (2012) American Chemical Society.

1.6.2. Optical Applications

The overall performance of optical devices is highly dependent on their transparency. In addition, self-cleaning materials or coatings are highly desirable in optical applications. Generally, high performance self-cleaning surfaces are attributed to their superhydrophobicity which could be enhanced by increasing their surface roughness. However, surface roughness and transparency are competitive properties. Four major indices for optical devices are their transparency, clearness, dust-free and self-cleaning properties. However, increase of surface roughness could enhance self-cleaning property but sacrifice surface transparency, which may hinder the application as optical devices. Interestingly, roughness structures with dimensions lower than 100 nm will inversely increase the surface transparency. Hence, nanoimprinting techniques have been applied for constructing optical films with nanostructured roughness. AAO templates with tunable well-ordered pores are of particular importance among the nanoimprinting techniques profit for endowing optical devices with designed nanostructures from its simple and cost-effective nature.^[77,78] For instance, Lee *et al.* had reported fabrication of smart optical devices via AAO patterning. The fabrication process is illustrated in Figure 1.17 A.^[79] In detail, polydimethylsioxane (PDMS) prepolymer mixture was first cured in an AAO membrane, and after peeling off from the AAO, a nanopillar structured PDMS film was obtained. Further, the PDMS film was oxidized under uniaxially stretching upon ultraviolet-ozone radiation. Further, hydrophobic treatment was carried out via silanization with heptadecafluoro-1,1,2,2-tetrahydrodecyltrichlorosilane. After the

functionalization, PDMS surface with periodically wavy microstructures that are perpendicular to the pre-strain direction and studded with nanopillars were obtained. Upon stretching, the generated wrinkles are released and microscale structures have vanished leaving the nanopillars on the surface, hence revealing a transparent film. On the contrary, upon releasing, the microstructures were again generated, which in turn lead to an opaque surface as illustrated in Figure 1.17 B. This stimuli-responsive film could be further applied as a smart window in the field of microfluidic devices and biosensors.

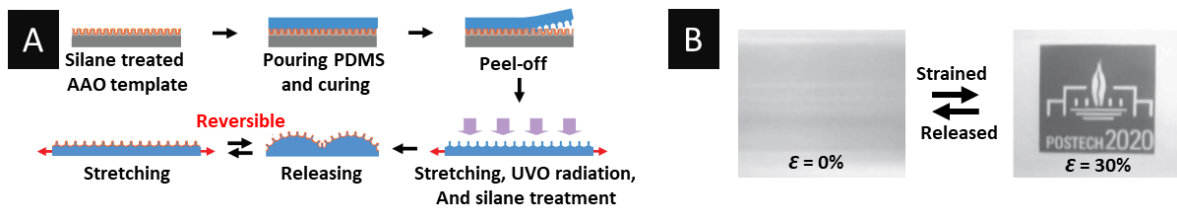


Figure 1.17. (A) Fabrication of hierarchically structured PDMS film and surface treatment, (B) optical image of PDMS film overlaying a printed paper before and after strain changes from 0 % to 30 %. Reproduced with permission from Ref. [79], copyright (2010) John Wiley and Sons.

1.6.3. Stimuli-Responsive Nanopillars

Stimuli-responsive polymers are capable to change their chemical or physical properties via exposure to specific stimulations.^[80] Such materials are divided into diverse categories depending on the stimulus, such as: pH,^[81] temperature,^[82] humidity,^[83] mechanical force,^[84] light,^[85] electric/magnetic field,^[86] or the presence of small molecules or biomolecules,^[87,88] etc. Accordingly, stimuli-responsive polymers are playing increasingly roles in the field of drug delivery,^[89] textiles,^[90] actuators,^[91] biosensors,^[92] coatings,^[93] and for many other applications.^[94–96]

Stimuli-responsive surfaces, also known as smart surfaces, can undergo a specific conversion, such as wettability transformation,^[97] adhesive property,^[98] or optical property^[99] variations, etc., in response to stimulations. For functional surfaces, the inherent composition and surface structures are of particular importance for the determination of a surface property. Therefore, AAO templates bearing hexagonally packed uniform nanocylinders are an ideal tool for the fabrication of micro/nanostructures on specific surfaces. Hence, by combining the AAO templating method and

stimuli-responsive polymers, smart surfaces with micro/nanostructures could be fabricated which have great potential in the application of cell adhesion, lossless drug transportation, batteries, etc.

1.6.3.1. Temperature Responsive Polymers and Nanopillars

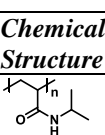
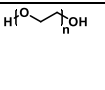
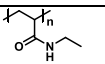
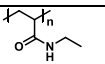
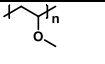
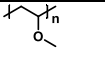
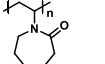
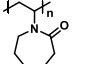
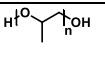
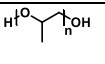
Temperature-responsive polymers, or also known as thermo-responsive polymers, are polymers whose physical properties undergo a drastic and discontinuous change with temperature. The critical solution temperature is one of the important features for temperature responsive polymers. Accordingly, thermo-responsive polymers can be divided into two categories: polymers with a lower critical solution temperature (LCST) or an upper critical solution temperature (UCST). In other words, a miscibility gap of polymers can be found to be lower or higher than the critical solution temperature. Polymers with a LCST are soluble in water at low temperature, while phase separation occurs between polymer chains and solvent while heating up. Until now, a wide variety of polymers are found to exhibit thermo-responsive properties with a LCST in aqueous solutions. LCST is determined by a balance between polymer-water interactions and polymer-polymer interactions.^[100]

Unlike LCST, UCST transition is mostly enthalpy-driven process, which leads to a broader transition in comparison to LCST.^[101] The most famous type of UCST polymer in water is polybetaine. Polybetaine is a zwitterionic polymer, which contains both negatively and positively charged groups in one repeating unit. At low temperature, the strong polymer-polymer electrostatic interactions lead to the collapse of polymer chains, which will reveal an insoluble state and vice versa. Besides, the UCST behavior can also be achieved by attractive hydrogen bonding interactions. Indeed, this kind of UCST polymers mostly contain primary amine groups.^[102] In addition to the above mentioned examples, Table 1.2 summarizes the commonly reported LCST and UCST polymers, and accordingly more information is accessible in the inserted references.

By incorporating temperature stimuli-responsive polymer into AAO templates, smart surfaces are obtained. For instance, Sanz *et al.* has reported thermally induced softening of PNIPAm-nanopillar-arrays, which were fabricated from SI-ATRP in AAO template and further transferred onto a coated substrate as illustrated in Figure 1.18.^[103] The PNIPAm nanopillar microstructure showed an increased stiffness as the temperature increased, which was in accordance with the crosslinked

network deswelling and expulsion of solvent. Furthermore, Giussi *et al.* had improved the responsiveness of PNIPAm-nanopillar-arrays through incorporating Fe₂O₃ nanoparticles into the PNIPAm nanopillars. Their smart films showed great potential as thermo-responsive magnetic surfaces in photonics, cancer therapy, tissue engineering among others.^[104]

Table 1.2. Common LCST and UCST polymers in water phase. Reproduced with permission from Ref. [105], copyright (2016) John Wiley and Sons.

Polymer with LCST	Chemical Structure	LCST (°C)	Ref.	Polymer with UCST	Chemical Structure	UCST (°C)	Ref.
Poly(<i>N</i> -isopropylacrylamide) PNIPAM		30-35	[106]	Poly(3-dimethyl (methacryloyloxyethyl) ammonium propane sulfonate) PDMAPS		60	[107]
Poly(ethylene oxide) PEO		100-175	[108]	Poly(6-(acryloyloxymethyl)uracil) PAU		80	[109]
Poly(<i>N</i> -ethylacrylamide) PEA		82	[110]	Poly(2-hydroxyethyl methacrylate) PHEMA		22	[111]
Poly(methyl vinyl ether) PMVE		34	[112]	Poly(<i>N</i> -acryloyl glycinamide) PNAGA		22	[113]
Poly(<i>N</i> -vinylcaprolactam) PVCL		32	[114]	Poly(<i>N</i> -acryloyl asparagineamide) Derivative of PNAGA		40.5	[115]
Poly(propylene glycol) PPG		15-42	[116]	Poly(methacrylamide) PMAAm		60	[107]

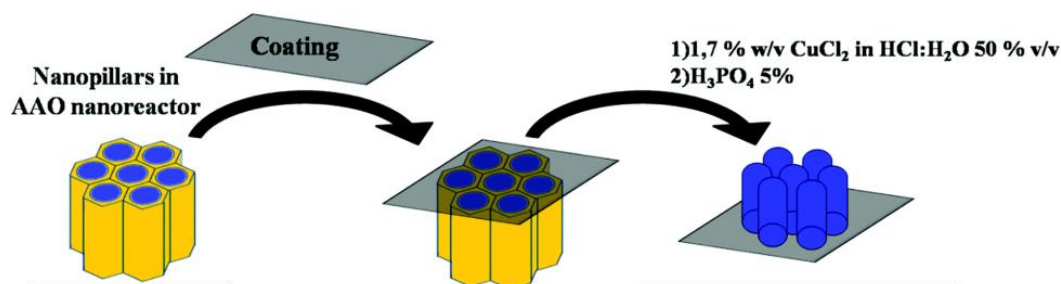


Figure 1.18. Preparation of PNIPAm nanopillars from AAO template. Reprinted with permission from Ref. [103], copyright (2017) Royal Society of Chemistry.

1.6.3.2. pH Responsive Polymers and Nanopillars

The pH responsive polymers are able to undergo manipulation of solubility, volume or chain conformation via external pH change.^[117] The adjustment of pH causes changes in ionic interaction, hydrogen bonding and hydrophobic interaction within polymer chains, which result in reversible microphase separation or self-organization.^[118] Therefore, pH responsive polymers pave the way in preparation of smart functional materials for controlled drug delivery, industrial coatings, oil manipulation, biological and membrane science, water remediation, etc.^[94,119]

The pH responsive polymers can be mainly categorized as: acidic and basic pH responsive polymers. Generally, polymers with weak acidic group or basic residues, such as: carboxylic groups, sulfonic acid, phosphonic acid, amino acid and boronic acid, are classified as pH response acidic polymers. Such acidic polymers are able to accept protons at low pH media while release protons when pH value is high. On the contrary, polymers with weak polybases, which capable to undergo ionization and deionization transitions from $\text{pH} \approx 7 \sim 11$, are called pH responsive basic polymers. The pH responsive basic polymers accept protons at low pH value while releasing them at basic conditions. Polymers that contain tertiary amine groups, morpholino, pyrrolidine, piperazine, pyridine, imidazole groups are the common pH responsive basic polymers.^[120]

Ma *et al.* had prepared poly(acrylic acid) (PAA) decorated pH responsive soft/hard composite surface from AAO templating as illustrated in Figure 1.19. This functional surface offered a high load bearing and tunable friction properties. The PAA/AAO nanopillar composite with a thin gel substrate exhibited higher resistance to friction than bulk hydrogel, attributed to the porous AAO template, which strongly strengthened the interfacial bonding of the gel to the substrate, thus preventing the gel arrays from peeling off. Besides, high-density gel nanoarrays produced high counter-ion osmotic pressure, which in synergy result in ultralow friction. Additionally, owing to the hydrating and dehydrating property of PAA polymer upon pH stimulation, PAA/AAO composite surface can undergo friction switching by tuning the pH value from acidic to basic. These findings have paved the way towards design of pH stimulus friction-tunable devices for the use of mass transportation and chemical actuation.^[121]

Additionally, combining both pH and temperature stimuli-responsive polymers with AAO templating, Du *et al.* had synthesized PAA nanopillar arrays grafted with PNIPAm nanobrushes, which they named as a micro/nanobrush dual structural surface. Pillar arrays endowed the surface

with an underwater superoleophobic property, while the stimuli-responsive PNIPAm brushes induced switchable oil adhesion. By replacing PNIPAm brushes with zwitterionic polymer brushes, the surface exhibited antifouling ability with excellent inhibition of algal attachment, which turned to be of great usage in marine environment.^[122]

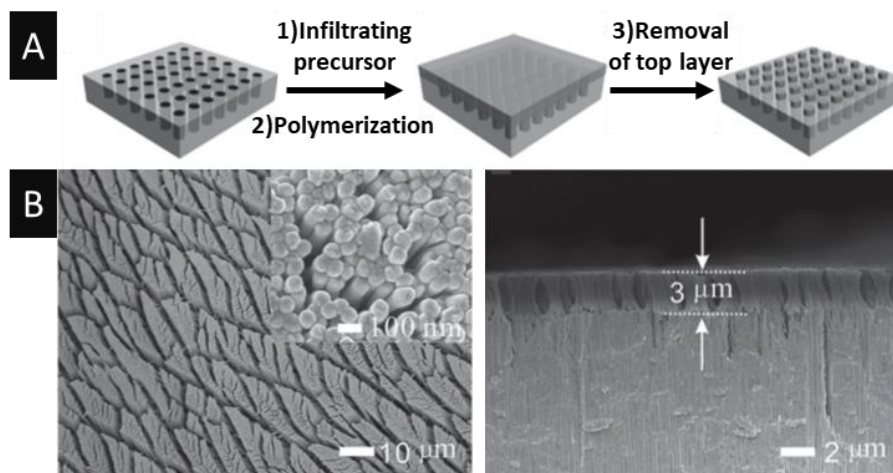


Figure 1.19. (A) Schematic fabrication illustration and (B) SEM images of PAA/AAO soft/hard composite. Reprinted with permission from Ref. [121], copyright (2015) John Wiley and Sons.

1.6.3.3. Light Responsive Polymers and Nanopillars

Upon exposure to light, the photoresponsive polymers can undergo changes in their properties such as, conformation, charge, polarity, amphiphilicity, optical chirality, conjugation, etc. Furthermore, those molecular changes are reflected in a macroscopic variation of material properties like shape, conductivity, wettability, optical properties, adhesion, etc.^[123–126] Chromophores are the main functional groups, which endow polymers with photoresponsive properties. Among all the chromophores, azobenzene is the most studied chromophore. The thermodynamically stable rod-like *trans*-isomer is transformed to the metastable bend *cis*-isomer, upon absorption of a photon by an azobenzene molecule. On the contrary, the inverse process *cis*-to-*trans* isomerization can be initiated by the absorption by the *cis*-isomer of another photon of suitable energy or can proceed spontaneously in darkness driven by heat.^[127] Incorporation of azobenzene groups into polymer chains enabled tuning polymer hydrophilicity, chirality or optical properties, etc.^[128] Besides,

spiropyran group is another widely used chromophore, as it shows a reversibility between an unconjugated spiroheterocycle form and charged planar merocyanine upon irradiation.^[129,130]

As an example, Jo *et al.* had fabricated ultraviolet responsive nanoarrays by adopting post-polymerization modification process with AAO templating. First, the active ester bearing poly(pentafluorophenyl acrylate) (PPFPA) nanorods were fabricated from AAO template via in situ polymerization of PFFPA monomer, then *N*-(2-aminoethyl)-3-(3',3'-dimethyl-6-nitro-spiro[chromene-2,2'-indoline]-1'-yl)propanamide molecules were grafted onto the nanoarray through the transesterification reaction between pentafluorophenyl acrylate and amine group of spiropyran. The new formed nanoarray-film reveals wettability variation owing to the photoisomerization of spiropyran group into a merocyanine form upon UV treatment. The combination of post-polymerization and AAO templating concept provided a facile and widespread method for the fabrication of smart surfaces.^[131]

In addition to the above mentioned categories, other stimuli-responsive polymers are also of rising interest, such as mechano-responsive and gas stimuli-responsive polymers.^[132–135] They are all of great importance for the fabrication of multifunctional smart structures and materials at various scales ranging from microcosmic to macroscopic.

1.6.4. Bio-related Applications

Beside the aforementioned applications, nanopillar surfaces are also capable to be used in the field of tissue engineering by benefitting from their high surface energy for retention of nucleic acid, immobilization of enzymes, proteins or cells.^[67] The AAO templating approach enables variation of obtained pillar arrays in chemistry, geometry, pillar height, diameter and spacing, and consequently the adjustable morphologies are utilized for mimicking diverse bio-related materials. Additionally, fabrication of polymeric nanopillars via AAO template with a controllable aspect ratio facilitates productive, high output and low cost methodology for bio-related applications.^[136–138]

For instance, Chen *et al.* had prepared free standing poly(methyl methacrylate) (PMMA) nanopillars via photo-polymerization in AAO template, which was subsequently solution-phase freeze-dried.^[139] After the releasing the PMMA pillars from the template, the PMMA nanopillars

were integrated into microfluidic channels, which were used in sorting of deoxyribonucleic acid. In addition, Liu *et al.* had demonstrated the fabrication of patterned nanotube arrays from AAO to be used as cell-capture materials.^[140] The fabrication process is illustrated in Figure 1.20.

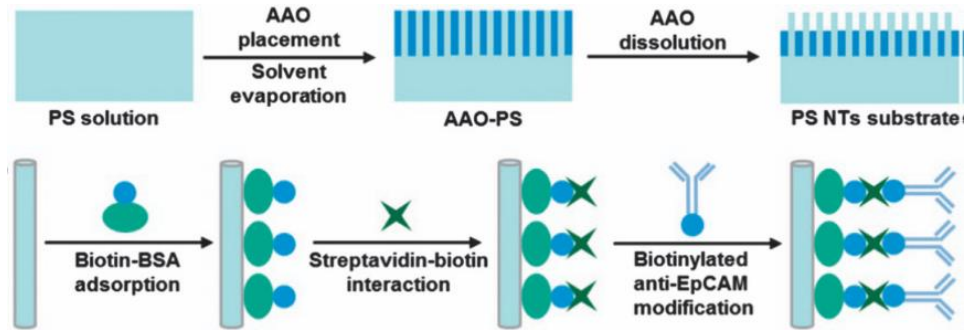


Figure 1.20. Fabrication and modification of polystyrene nanotube substrate for cell adhesion. Reprinted with permission from Ref. [140], copyright (2013) Springer Nature.

As revealed, polystyrene nanotube arrays are first prepared by replication from the AAO membrane via solvent wetting. Subsequently, after obtain the PS nanotube substrate, post-modification is carried for combining biotinylated anti-human epithelial cell adhesion molecule onto PS pillars. The integrated soft nature of PS nanotubes, as well as specific capture agents provide potential optimal application in high-quality cancer-cell capture. The functional arrays showed ca. 80 % cell capture efficiency, which was 30 % higher than bulk PS substrate. As a consequence, the PS nanotube substrate were utilized as novel candidates for cell isolation platform.

AAO templating method is generating not only pillar arrays but also hierarchical topography with different scale grades for the application of bio-related materials. Du *et al.* had reported the fabrication of hierarchical poly(ϵ -caprolactone) (PCL) nanowire micropattern by adopting AAO-assisted templating.^[141] The double template method was illustrated here by using aluminum grid, as the first template for the fabrication of micropattern-island, while AAO membrane as the second template in order to generate nanowire-structures on top of the micropattern. The inserted SEM images demonstrate attained morphology of prepared material. The obtained PCL films are demonstrated for protein retention. The coexistence of nano- and micro-scale structures as revealed in Figure 1.21 provide a more preferable environment for cell seeding in comparison to smooth surfaces.

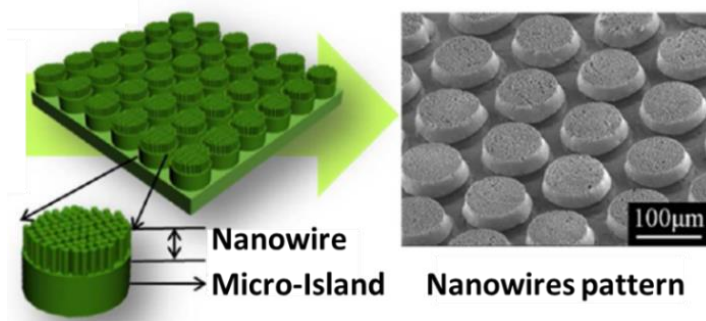


Figure 1.21. Highly ordered hierarchical PCL nanowire patterns by the double template method. Reprinted with permission from Ref. [141], copyright (2012) American Chemical Society.

As mentioned above, the AAO templating strategy enables the production of a large variety of polymeric nanoarrays. Compared with bulk materials, their nanostructured counterparts showed obvious advantages as nanodevices attributed to the high aspect ratio, uniform arranged microstructure and adjustable surface morphology accompanying surface properties. As such, there is no doubt that AAO membranes play an all-important role in preparing functional surfaces.

1.7. Direct Functionalization of AAO Membrane

AAO templates bearing well ordered nanochannels are not only useful for patterning nanostructures, but the AAO template itself can also be used for specialized transport processes in the field of protein gating, water purification, photonic device, battery and sensor, etc., or able to be constructed into composite devices for substance storage and delivery.^[29] As it has been already mentioned, AAO membrane is inherently insulating, it lacks stability in acidic and basic environment, which hinders their potential application. However, AAO membranes are enriched with hydroxyl groups on the membrane surface, which allows them to be further modified via nine tenths of existing modification approaches. This, in turn, expands the applications of AAO templates as functional membranes. In this section, the possible methods for the preparation of organic materials functionalized AAO membrane are reviewed and their potential applications are discussed. Figure 1.22 lists a variety of possible modification methods, such as self-assembly process, chemical vapor deposition, polymer grafting, etc., for the preparation of smart AAO membrane.^[111,112]

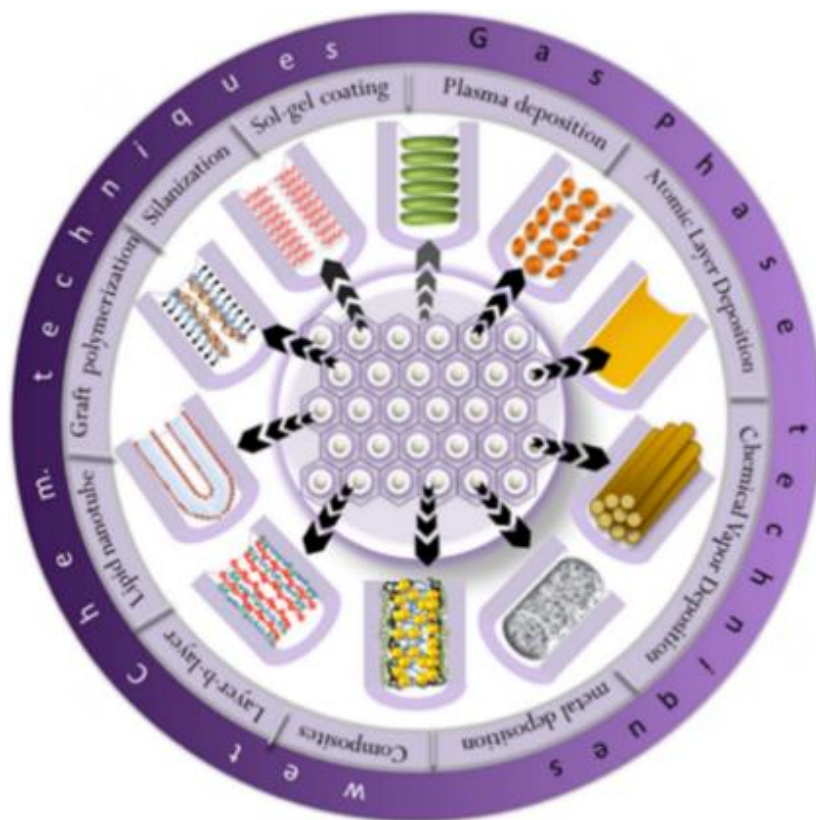


Figure 1.22. A wide range of approaches applicable to modify AAO surfaces. Reprinted with permission from Ref. [29], copyright (2013) Elsevier.

1.7.1. Self-Assembly

The self-assembly strategy refers to organic assemblies formed from liquid phase onto solid surfaces via spontaneous adsorption, rearrangement or chemical reaction.^[29] Self-assembly of desired functionality is straightforward for AAO modification. The regulation of surface wettability and adsorption properties of AAO membrane could be easily realized by silanization with diverse silanes.^[20] Indeed, by adopting silanization, Liu *et al.* had prepared amphiphilic AAO membranes for water dry condensation.^[144] The amphiphilic AAO membrane was fabricated by modifying one side of the AAO membrane with dodecyltrichlorosilane to increase its hydrophobicity, while maintaining the other side hydrophilic. The hydrophobic surface prevented the accumulation of water droplets, hence exhibiting a self-cleaning property. The authors showed that this membrane was capable of processing “dry condensation” in such a way that water droplets are rapidly driven from the hydrophobic surface to the hydrophilic side through the hydrophilic porous channel.

Therefore, this material has the potential to be applied to different fields ranging from water-harvesting and phase-change-based desalination to energy generation and transfer.

Besides, in order to incorporate multi-functionality in one template, combinations of anodization and silanization cycles with different silane derivatives were carried out by Jani *et al.*^[145] Stepwise procedures are illustrated in Figure 1.23. In detail, after the first anodization step, the oxidized layer was removed to leave behind only the barrier layer. Subsequently, functionalization was carried out in order to deliver the first layer of silane assembled on the template surface. Starting from the first silanized layer, a second anodization step was further accomplished to generate pores that were immobilized with second silane derivative. Consequently, a two-layered AAO membrane was obtained. Notably, according to the presented strategy, numerous layers could be achieved in one template via continuous anodization and silanization steps, hence different functionality and wettability could be added onto AAO membrane.

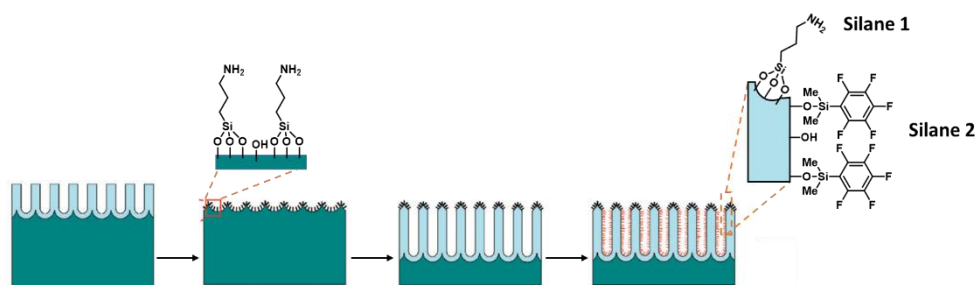


Figure 1.23. Producing layered surface chemistries in AAO membrane. Reprinted with permission from Ref. [145], copyright (2009) Royal Society of Chemistry.

In addition to the above mentioned self-assembly of silane, LbL assembly of polymer materials onto AAO membrane can also control the membrane surface wettability, thus endowing AAO with the potential applications in the field of molecular separation, drug release and bio-sensing. Indeed, Cho *et al.* had decorated AAO membrane with multi layers of poly(styrene sulfonate) and poly(allylamine hydrochloride) by alternatively dipping AAO membrane into charged polyelectrolyte solutions.^[146] The pore size of AAO membrane was reduced in accordance with the addition of polymer layers, hence, LbL assembly of polyelectrolytes in AAO is capable to be used as simplified size-exclusion chromatography.

1.7.2. Initiated Chemical Vapor Deposition

Initiated chemical vapor deposition (iCVD) is one gas phase technique from reactive monomer and initiator for synthesizing of polymeric film onto desired substrates.^[147] During a typical iCVD polymerization process in AAO, monomers are first adsorbed onto membrane surfaces, in the meantime, initiators are decomposed by thermal or plasma excitation and formed into reactive radicals. Further monomer molecules are initiated via reactive radicals and polymerization on membrane surface is eventually accomplished. Ultrathin and evenly distributed polymer layers are achieved via iCVD methodology.^[148–150] For instance, Losic *et al.* had deposited *n*-heptylamine via plasma enhanced iCVD AAO membrane.^[151] By adjusting the deposition time, the thickness of polymer layers could be controlled within nanometer precision. As a result, the pore size of AAO membrane were simultaneously adjusted. Additionally, attributing to the introduction of amine groups on the membrane surface, the biocompatibility of the modified membrane enabled its potential application in the field of biotechnology. Besides, Tufani *et al.* had decorated AAO membrane via thermally initiated iCVD strategy with thin layer of pH sensitive poly(methylacrylic acid-*co*-ethylene glycol dimethacrylate).^[152] Attributing to the pH responsive property of grafted polymer chains, the pore size of AAO membrane can be adjusted through swelling and de-swelling of grafted polymer chains under pH variations. Consequently, the variations in pore size facilitated the functionalized AAO membrane to be utilized for size dependent molecule selective separation. Simultaneously, protonating and de-protonating stimulations of polymer brushes in response to pH could alter the membrane charge. As a result, the charge interactions between membrane and permeates will thus affect membrane permeability.

1.7.3. Polymer Grafting

Referring to the modification of AAO membranes with polymeric materials, researchers have developed a variety of methods for endowing AAO with adjustable functionalities and surface topography. Polymeric materials are easy to be modified and exhibit specific recognition and selectivity. Additionally, grafted polymer chains equip the membrane with diverse properties via altering grafting parameters ranging from degree of polymerization, dispersity, grafting density to distributions along membrane channels.^[153] Mainly, the polymer grafting method consists of “grafting to” and “grafting from” approaches. End-functionalized polymer chains are able to be

“grafted to” a solid substrate while the “grafting from” approach is accomplished by polymerization from pre-immobilized initiating point from the solid substrate. For instance, Kim *et al.* had demonstrated typical “grafting to” method for the fabrication of PNIPAm grafted AAO membrane.^[154] In detail, catechol-tethered PNIPAm chains were first synthesized and thereafter, owing to high affinity between catechol groups and aluminum oxide, catechol end-functionalized PNIPAm chains were grafted onto membrane pore walls, as illustrated in Figure 1.24.

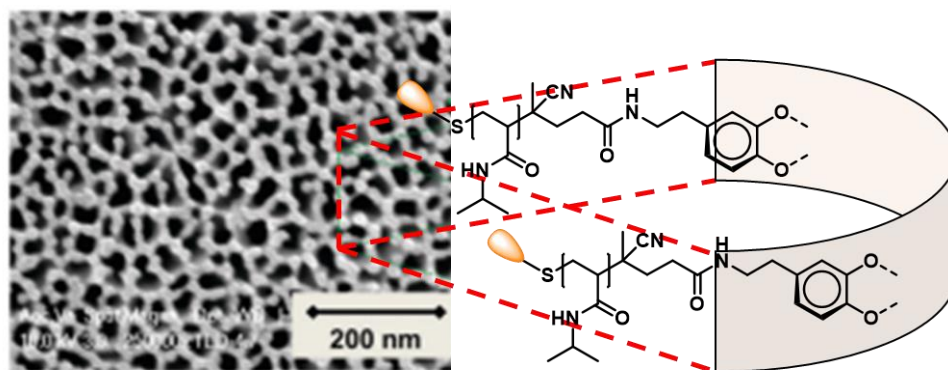


Figure 1.24. Schematic illustration and SEM image of catechol end-functionalized PNIPAm grafted AAO membrane. Reprinted with permission from Ref. [154], copyright (2012) Royal Society of Chemistry.

In addition, another example of “grafting to” method for decorating AAO membrane has been reported by Lu *et al.* In detail, pre-prepared poly(styrene)-*block*-poly(4-vinylpyridine) (PS-*b*-P4VP) polymers were anchored onto the bromide group pre-modified AAO template through quaternization reaction.^[155] The pH responsive P4VP endowed the modified AAO membrane with adjustable surface wettability upon pH stimulations. In acidic media, protonation happened in the P4VP segment, thus enhancing the membrane hydrophilicity and resulting in a high affinity to water droplets, while when immersed membrane into basic media, deprotonation of grafted P4VP chains occurred, which resulted in the increase of membrane hydrophobicity and showed a strong affinity to oil droplets. This smart membrane has the potential to be utilized for oil/water emulsion separation and sewage purification as schematically illustrated in Figure 1.25.

Beside, Jiang *et al.* had prepared PNIPAm grafted AAO membrane through “grafting from” method via SI-ATRP.^[156] As aforementioned, after immobilization of an ATRP initiator onto the AAO membrane, polymerization of NIPAm was carried out resulting in a PNIPAm functionalized AAO membrane. Attributing to the thermo-responsive property of grafted PNIPAM chains,

wettability of PNIPAm-grafted AAO membrane could be tuned by controlling the temperature below or above LCST of PNIPAm. This thermo-responsive membrane can be further used as thermo-responsive water transport devices, and the strategy could then be carried out for the fabrication of different functional AAO membrane devices.

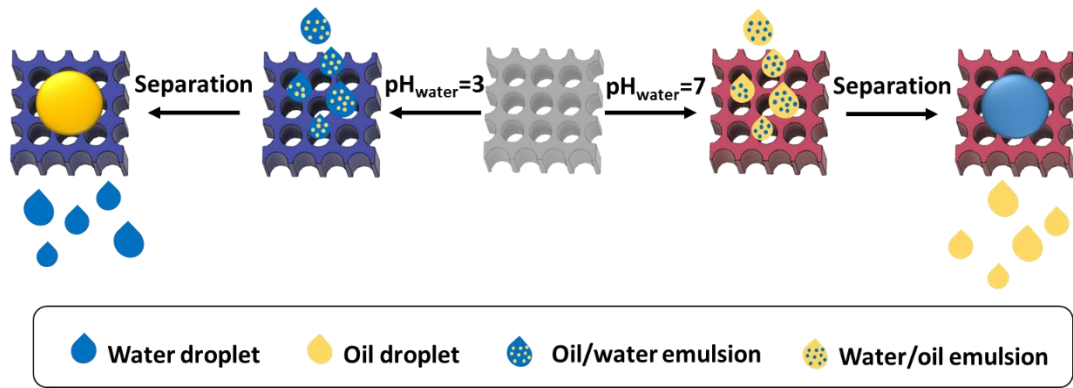


Figure 1.25. Schematic illustrating of poly(styrene-block-4-vinylpyridine) grafted AAO membrane for selective separation of oil/water emulsions. Reprinted with permission from Ref. [155], copyright (2018) Elsevier.

By adopting the same fabrication method and same polymer, Szuwarzyński *et al.* transformed an AAO membrane into a pulsatile releasing platform.^[157] Accordingly, they used AAO template with only one side opened, and grafted the PNIPAm brushes via SI-ATRP onto the top surface of AAO template. Since, the PNIPAm could change the conformation upon temperature stimulation, the PNIPAm brushes can serve as thermally responsive valves that can control on/off function of the membrane pores in order to realize controlled pulse releasing of dye molecules. When the temperature is increased above PNIPAm's LCST, PNIPAm brushes are dehydrated and coiled, thus leaving the pores open, and the pre-entrapped Calcein molecules are released. On the contrary, when the temperature is decreased below LCST, rehydration of PNIPAm brushes took place. PNIPAm polymer chains stretched and further blocked the membrane pores, and accordingly the release of Calcein is stopped. By further adjusting the temperature, reversible control of releasing could be achieved. The loading capacity and releasing rate could be easily controlled via regulating the pore diameter and length of AAO membrane, and the modified membrane showed potential application in the field of nano/microfluidic system.

Although SI-ATRP strategy has been widely adopted for decorating AAO membranes with polymer brushes, the request for rigorous de-oxygenated atmosphere and indispensable addition of toxic metal catalysis constitute harsh reaction conditions which limit the universality for membrane modification. In addition to simplify working conditions while maintaining grafting efficiency, surface-initiated reversible addition-fragmentation transfer polymerization were applied. It has been addressed by Song *et al.* via the SI-RAFT approach for AAO membrane modification.^[158] Through surface immobilized chain transfer agent, RAFT polymerization of poly(3-(methacrylamidomethyl)-pyridine) was thereafter carried out, thus accomplishing grafted chains on AAO membrane.

Additionally, through grafting with diverse polymer chains in a single AAO membrane, asymmetric templates could be further fabricated. The complicated membrane exhibits superior multifunctionality, which could not be obtained otherwise. Lee *et al.* had grafted AAO membrane with PNIPAm and PAA on each side of membrane surface via polymer grafting approach.^[159] The grafted polymer chains act as pH or thermal stimuli-responsive gates of membrane channels, which could be further utilized for controlled water flux. As demonstrated in Figure 1.26 A, PNIPAm gates opened when temperature was below 32 °C and closed above 32 °C; while for the PAA gates, unclosed gates are revealed when pH lower than 4.25 while gates closed when pH value above 4.25. Synchronized controlling of temperature and pH, permeance of water was capable to be adjusted through the asymmetric membrane. Under the condition of 40 °C and pH 3, all the polymer brushes are dehydrated and both gates are opened for water fluxing through; while either lower temperature to 20 or increase pH to 6 membrane pores are closed and water is prevented from eluate. Further, the independent on and off gating membrane revealed controllability in store and release of compounds such as BSA, which illustrate enormous potential of obtained asymmetric membrane in mimicking cell membrane.

Supplementary, for expanding the fabrication of asymmetric polymer grafted membrane, different polymerization strategies could be processed in the same AAO membrane. Ma *et al.* had demonstrated that by adopting a half-cell reactor, simultaneous chemical polymerization, such as ATRP, DOP-SP (dopamine self-polymerization) and ROMP (ring-opening metathesis polymerization), are able to be conducted on each side of AAO, thus resulting in asymmetric polymer functionalization.^[160] Polymers distinct from categories, wettabilities or responsive

properties were respectively grafted onto AAOs and resulted in anisotropic membranes with multifunctionalities.

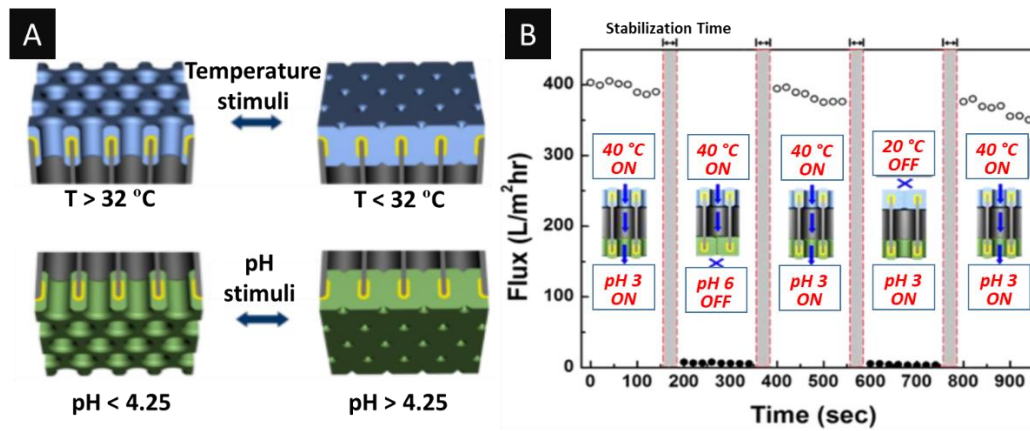


Figure 1.26. (A) Temperature-controlled PNIPAm gate and pH-controlled PAA gate, (B) change of water flux depending on temperature and pH. Reprinted with permission from Ref. [159], copyright (2016) American Chemical Society.

AAO templates featuring well-arranged cylindrical pores are considered as 3D-architected membrane. By taking advantage of their unique nanostructure, adjustable geometrics, superior biocompatibility, low fabrication cost, high output as well as good thermal, mechanical and organic chemical resistance, AAO is widely used as fundamental material for the preparation of functional nanocomposites. Although a variety of preparation methods have been proposed, feasibility and widespread availability need further enhancements to meet the actual demand. Moreover, numerous challenges are required to be solved in order to realize laboratory work to yield in commercial products. Indeed, more efforts should be devoted in the field of basic research of AAO on optimizing the existing methodology and materials for promoting the development of nanotechnology.

2. Scope and Objectives

Motivation of the work presented herein is to utilize a self-made laboratory AAO setup for fabrication of diverse AAO membranes differing in their architecture. Thereafter, based on obtained AAOs polymeric-nanostructured-materials, from one dimensional nanorods, to two dimensional hierarchical films, and further to three dimensional porous gating membranes shall be prepared.

Morphological adjustment is essential for controlling chemical and physical properties of nanoscaled materials. A comprehensive study of AAO template fabrication will be carry out in Chapter 3 based on a typical two-step anodization method. The working condition at each step during fabrication are tailored in order to obtain templates with desired structures. The fundamental study demonstrated in Chapter 3 will pave the way for further investigations on nanomaterial-fabrication via AAO templating.

Chapter 4 focuses on the preparation of polymeric Janus nanorods from as-prepared AAO templates. The polymeric nanostructures will be synthesized via *in situ* polymerization under confinement with styrene, NIPAm, PFPA, MMA and/or pyrrole. By stepwise polymerization of different monomers in AAO template, segmented polymer nanorods are formed. In addition, photo crosslinker 4-acryloylbenzophenone will be inserted in each polymer block in order to achieve chemical connection between each polymer block after post-photo-crosslinking to prevent any disassembly. In this chapter, Janus nanorods differ from chemistry and/or shape will be constructed and composition of polymeric Janus nanorod will be investigated.

The emphasis of Chapter 5 moved from above mentioned one dimensional nanostructures to two dimensional nanomaterials. Via using AAO template as pattern platform, well-arranged polymeric pillar arrays will be built on a polyester substrate. Owing to the inherent active groups from poly(pentafluorophenyl acrylate), amine end-functionalized poly(methacrylic acid) brushes are capable grafted onto pillar-arrays via post-polymerization modification forming hierarchical surfaces. Attributing to hierarchical morphology, the obtained film will exhibit underwater superoleophobicity. In addition, pH responsive poly(methacrylic acid) brushes will enable the surface reversible pH responsibility. Ultimately, the wettability transformation on oil manipulating will be further studied.

Chapter 6 will combine AAO templating with carbon dioxide stimuli-responsive polymers for preparing smart filtration membrane. Via surface initiated reversible addition fragmentation chain

transfer polymerization, poly(methyl methacrylate-*co*-2-(diethylamino)ethyl methacrylate) brushes are grown onto through-hole AAO membrane. Owing to the CO₂ stimuli-responsive property of grafted polymer chains, surface wettability as well as pore diameter of obtained membrane are adjustable. Taking advantage of this phenomenon, the smart membrane is tested for controllable water flux and emulsion separation.

3. Manufacturing of AAO Templates

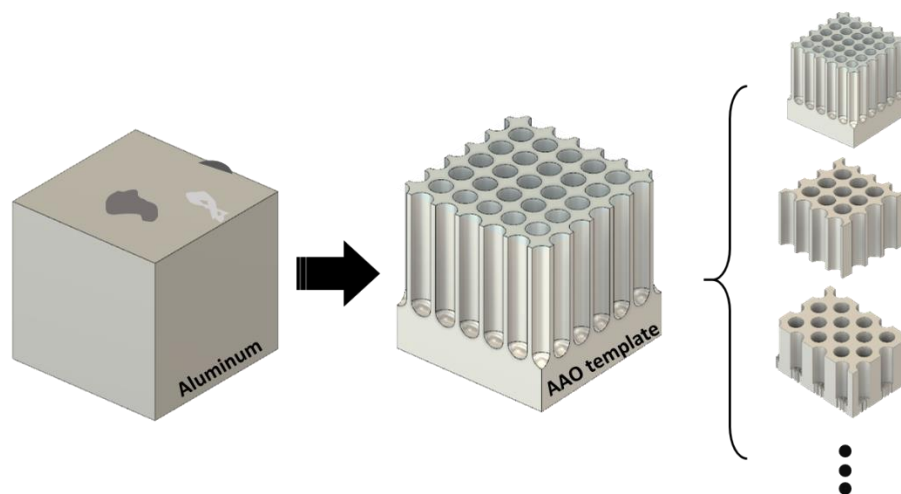


Table of content graphics of chapter 3.

3.1. Introduction

Since its invention in 1995, the two-step anodization method has been widely adopted in manufacturing of hexagonally arranged porous anodic aluminum oxide templates.^[13] The well-packed porous structure of AAO are formed during electrochemical reaction via self-assembly, therefore, by varying the working parameters during electrochemical reaction, such as electrolyte, voltage, anodization time, etc., enabled further control of template geometric construction like interpore distance, pore size, pore length, etc.^[161] Adjustable parameters bring numerous benefits to AAO template, for instance, the customized pore size and interpore distance, high pore density and controllable aspect ratio. Moreover, AAO fabrication conditions are easy to be obtained and large scale manufacturing are also attainable with relatively low costing. Although, nowadays AAO membranes are commercially available, the limited template selectivity, high irregularity and exorbitant price of the products hindered the massive usage in laboratory for the preparation of functional materials. Hence, establishing a laboratory AAO fabrication setup is essential to fulfill the demand for the preparing AAO membrane with defined geometry in order to be used as template for the production of smart nanomaterials.

Here in this chapter, it is the aim to utilize self-made laboratory AAO setup for the fabrication of variety AAO membranes with different geometric structure, and further to apply it in the preparation of polymeric nanomaterials. The main fabrication process consists of four main procedures, electro-polishing, first anodization, chemical etching and second anodization. Additionally, pore widening, aluminum substrate removing and backside opening process are the common post-treatments to fulfill diverse requirements of membrane structure on demand. All the solvents which have been used for template fabrication were listed in Table 3.1.

Table 3.1. *Solution recipe.*

<i>Solution</i>	<i>Application</i>	<i>Recipe</i>
<i>Polishing agent</i>	<i>Electro-polishing</i>	<i>100 mL HClO₄ (70 %), 300 mL EtOH (96 %)</i>
<i>Phosphoric acid electrolyte</i>	<i>Phosphoric acid anodization</i>	<i>0.688 mL H₃PO₄ (85 %) in 100 mL H₂O</i>
<i>Oxalic acid electrolyte</i>	<i>Oxalic acid anodization</i>	<i>3.78 g (COOH)₂·2H₂O in 100 mL H₂O</i>
<i>Etching agent</i>	<i>Alumina etching</i>	<i>1.8 g CrO₃ and 7.1 g H₃PO₄ in 100 mL H₂O</i>
<i>Pore widening agent</i>	<i>Pore widening</i>	<i>6.88 mL H₃PO₄ (85 %) in 100 mL H₂O</i>
<i>Aluminum removing agent</i>	<i>Aluminum removing</i>	<i>13.4 g CuCl₂ and 166 mL HCl (37 %) in 334 mL H₂O</i>

3.2. Electro-polishing

As aforementioned, high surface roughness is easy to cause membrane breakdown or burning during anodization process owing to the current localization phenomenon, which will further lead to irregular arranged membrane structures. Therefore, electro-polishing before anodization is indispensable for achieving regularly aligned porous AAO. Figure 3.1 A and B reveals a laboratory setup for electro-polishing. In detail, Al discs are mounted on a reaction chamber which consists of a PVC cell and a copper plate, the electro-polishing agent was added into the PVC chamber, further a PVC lid with a stir and woven Pt wire net was covered on top. Pt wire was connected to cathode, while copper plate, which is connected with Al discs was linked to anode. Upon electro-polishing, the applied voltage was increased to 20 V and kept at 5 °C for 5 min under vigorous stirring. During electro-polishing process, hydrogen gas bubbles were generated at the cathode, which further dispersed in the electrolyte or stick on the aluminum surface. Continuous stirring can effectively prevent the bubbles from sticking on the aluminum surface thus to restrain the forming of etch pits.^[162] Electro-polishing electrolyte consisted of perchloric acid (HClO₄) and ethanol. HClO₄ provides a low pH condition to ensure ionization of aluminum into Al³⁺ cations, while

ethanol acted as shielding molecules that are able to decrease ion-flux and stabilize surface aluminum atoms.^[163] Additionally, voltage is set at 20 V which forestall the forming of swarming bubbles at higher voltage and guaranteed stability of whole working system.^[164] After electro-polishing process, shiny Al discs are obtained (Figure 3.1 C). Although the pristine Al disc had a relatively high purity, thin alumina layer was easily formed on the surface, additionally high roughness can be observed from SEM image of pristine Al disc, as illustrated in Figure 3.1 D, after electro-polishing high roughness are found to be diminished and the Al disc demonstrate a relative smooth appearance.

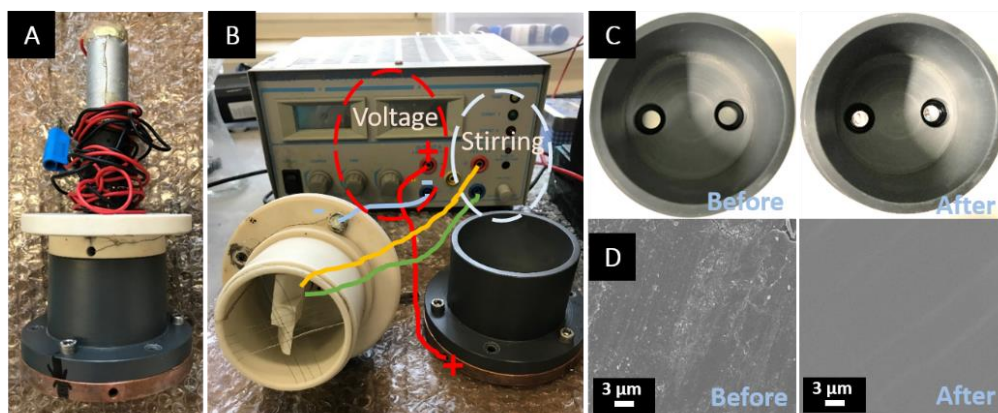


Figure 3.1. Optical images of (A) electro-polishing reaction chamber and (B) laboratory setup, (C) Al discs before and after electro-polishing and (D) SEM image of Al discs before and after electro-polishing.

3.3. First Anodization

After electro-polishing, Al discs are processed to the first anodization in 1 wt% aqueous phosphoric acid or 0.3 M oxalic acid. Figure 3.2 A shows the working setup for anodization. The working chamber here also contains two parts, a PVC chamber which mounted with Al discs and a metal lid embedded with stirrer, Pt wires and enfolded with an insulation foam layer. The working chamber is placed on a cooling system while anodization and temperature is kept constantly at 1 °C. During anodization process, the whole working chamber is manipulated by computer controlled voltage supplier that the Pt wire is connected to cathode while copper plate that connected with Al discs is linked to the anode. Anodization is carried out at 40 V for 20 h for oxalic acid anodization.

While for the phosphoric acid anodization was processed at 175 V for 3 h and then increased to 195 V for additionally 20 h. Several chambers could be installed in series, thus generating a high productivity. During the first anodization, electric field was distributed over the aluminum surface at the beginning building up a uniform and compact alumina layer, once it is accomplished, the electric field localizing and producing strong joule heat that forces the production of localized grooves. These pits act as nuclear sites and pores are formed during further anodization.^[29] Top view and cross section of AAO membrane after first anodization from oxalic acid is characterized by SEM and exhibit in Figure 3.2 B and C, from which, irregularly arranged pores are observed.

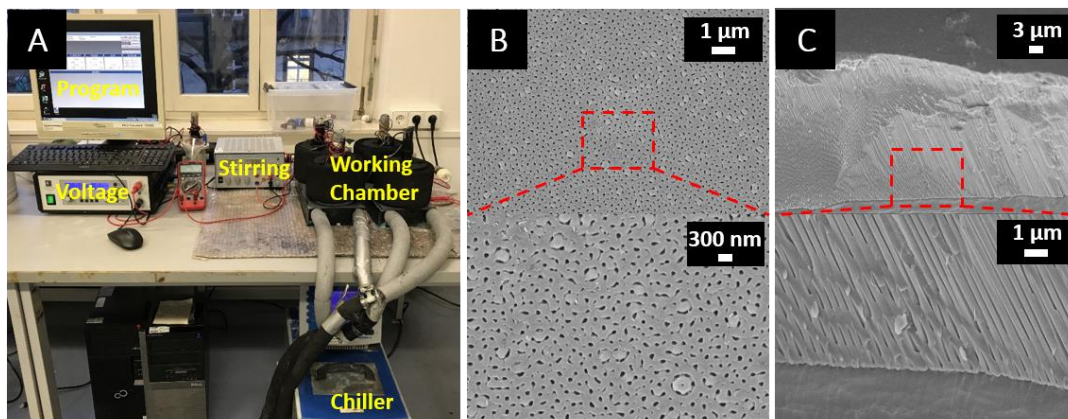


Figure 3.2. The optical image of (A) anodization set up and the SEM image of aluminum discs after first anodization (B) top view and (C) cross section.

3.4. Chemical Etching

Followed, a chemical etching process was carried out in etchant, which consists of chromic oxide, phosphoric acid and DI water. The etching agent was directly poured into the PVC chamber after first anodization and then placed into drying oven at 45 °C for 36 h and 12 h respectively for phosphoric acid and oxalic acid anodized AAO membrane in order to remove the irregularly formed porous alumina layer and remain only the well-arranged dimple array on the aluminum surface.^[165] The SEM images in Figure 3.3 reveal that after selectively removed the porous structure, ordered concave pits emerged on the Al discs.

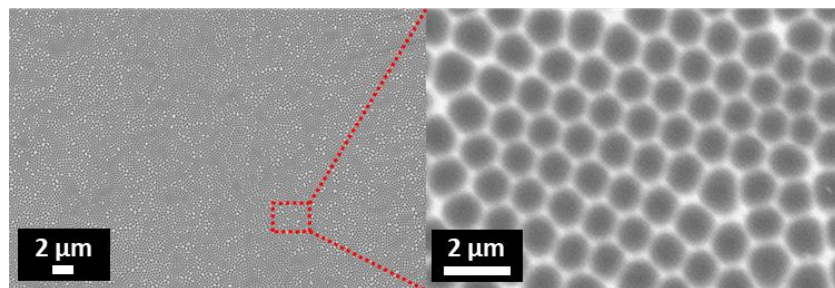


Figure 3.3. SEM image of phosphoric acid anodized AAO membrane after chemical etching.

3.5. Second Anodization

The second anodization was processed using the same working system as the first anodization. The voltage of oxalic acid anodization was kept at 40 V and the sample was anodized for 2 h. The obtained AAO membrane was characterized by SEM, and the results in Figure 3.4 reveal that the pore size of AAO template fabricated from oxalic acid was approximately 30 nm and after 2 h anodization, the length grows to $\approx 10 \mu\text{m}$. For phosphoric acid anodization, the voltage was kept at 195 V, under this condition the template with pore size of $\approx 200 \text{ nm}$ was obtained (Figure 3.5).

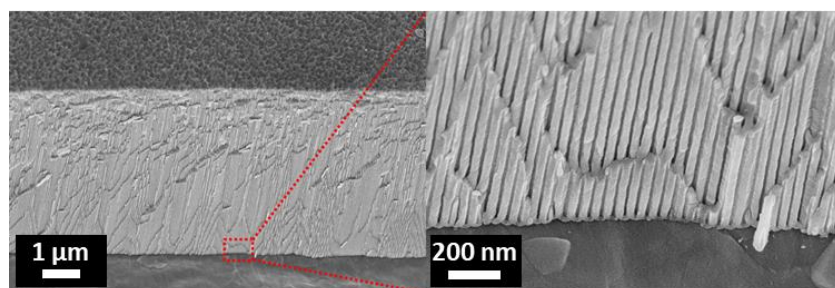


Figure 3.4. SEM image of AAO template fabricated from oxalic acid.

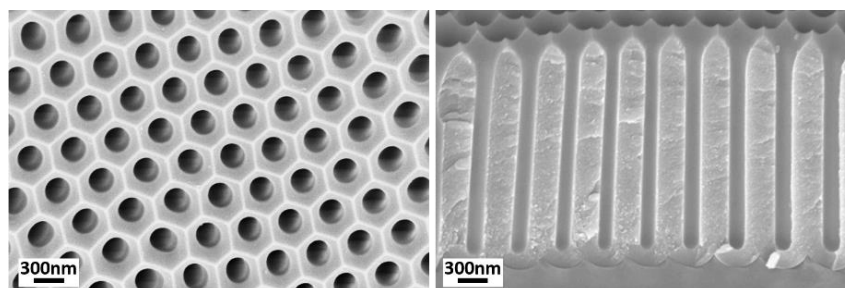


Figure 3.5. Top view (left) and cross-sectional (right) SEM images, respectively, of AAO template anodized with a phosphoric acid electrolyte.

As reported before, the anodization time determined the pore length of formed porous structure, therefore, according to various demand for template pore length, taking phosphoric acid anodization template as an example, second anodization was carried out for 30 min, 1 h, 90 min, 5 h, 6 h, and 20 h, respectively. The obtained SEM images in Figure 3.6 exhibit cross section views of obtained AAO templates after different anodization time. By fitting the experimental data, pore lengths of phosphoric acid anodized AAO membrane are liner dependent on the anodization time. The growing rate is $3.34\pm 0.05 \mu\text{m}/\text{h}$. By adopting the fitting curve, the length of porous structure vs time, pore lengths can be predicted, which is beneficial for the fabrication of various templates on demand.

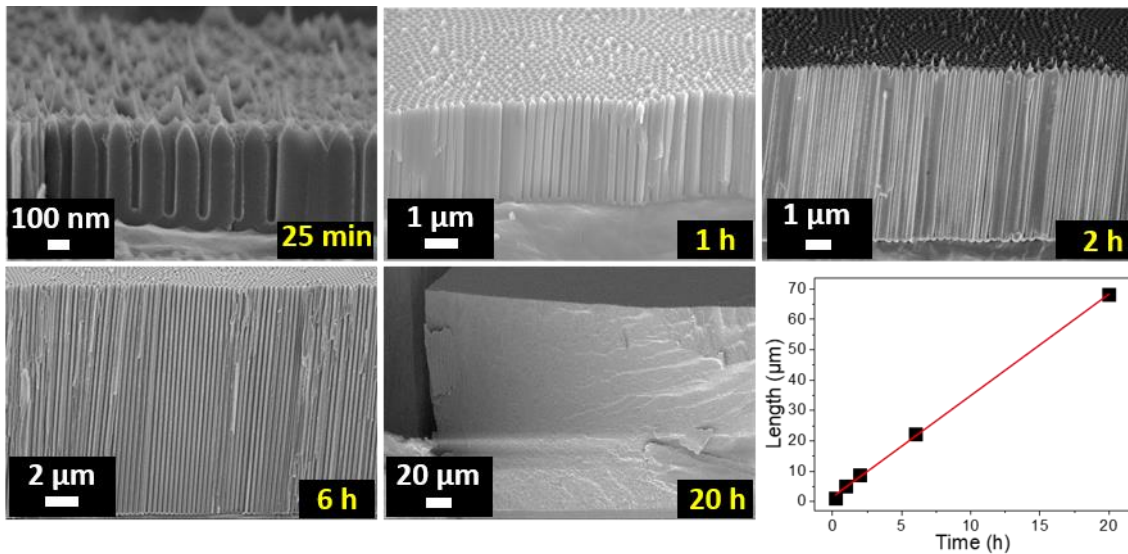


Figure 3.6. SEM image of AAO membrane upon different anodization time and the plotted figure for the relation between pore length and treatment time.

Despite the fabrication of isotropic AAO membranes, rationally design of hierarchically branched nanopores inside the AAO template was also achievable. In the following, AAO membranes with branched porous structure are fabricated. The primary pore structure was first fabricated from phosphoric acid under 195 V for 18 h, subsequently a barrier layer thinning step was processed by consecutively reduced of applied voltage from 195 V to 80 V with a speed of $-0.02 \text{ V}/\text{s}$. Then the electrolyte was changed against oxalic acid and the applied voltage was continuously reduced with the same speed from 80 V to 0 V. In order to further thinning the barrier layer, a pore widening process was carried out under the condition of 10 wt% aqueous phosphoric acid at room temperature for 1 h. Further a secondary second anodization process was processed in 0.3 M oxalic

acid under 40 V for 2 h. Further in order to clearly compare the pore structure of the phosphoric layer and the oxalic layer, aluminum substrate and barrier layer were removed resulting in a free stand AAO membrane. The morphology obtained AAO membrane is illustrated in Figure 3.7 by SEM characterization. As illustrated, branched pore architectures are observed in which larger pore sized structures are fabricated from phosphoric acid while the small sized channels are obtained from anodization in oxalic acid.

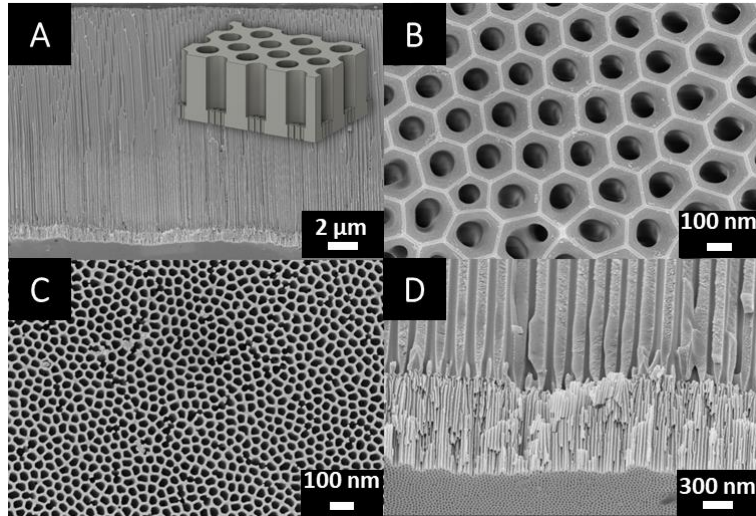


Figure 3.7. SEM images and inserted schematic figure of branched AAO membrane.

3.6. Pore Widening

The utilized electrolyte during anodization determined the initial pore diameter of the obtained AAO membrane. However, the size remains constant if the electrolyte is kept unchanged. Under this circumstance, a post-pore-widening process is an alternative facile option for the preparation of template with different pore sizes. The pore widening agent used here was 10 wt% aqueous phosphoric acid and operating temperature was kept at 45 °C. Figure 3.8 shows the surface morphology of an AAO membrane that obtained from phosphoric acid and processed to pore widening for different time periods.

As demonstrated, the pore sized increased as the pore widening time extended, but when treatment time reached 55 min, the barrier layer of template was sharply etched. While increasing pore widening duration to 60 min, the channels of the porous structure started to collapse and adjacent

pores merged together. From that moment on, membrane pores are not able to be further widened, i.e. the pore to pore distance determines the pore widening limit. From the plot in Figure 3.8, it could be concluded that before the collapse happened to AAO membrane, pore sizes increased at a speed of 3.93 ± 0.31 nm/min. It is observed that upon pore widening at 45 °C in 10 wt% phosphoric acid, pore size and pore widening time are in a linear relationship. This is of particular importance for the prediction of pore sizes during pore widening process, hence in order to achieve tailor-made fabrication of templates varied in apertures.

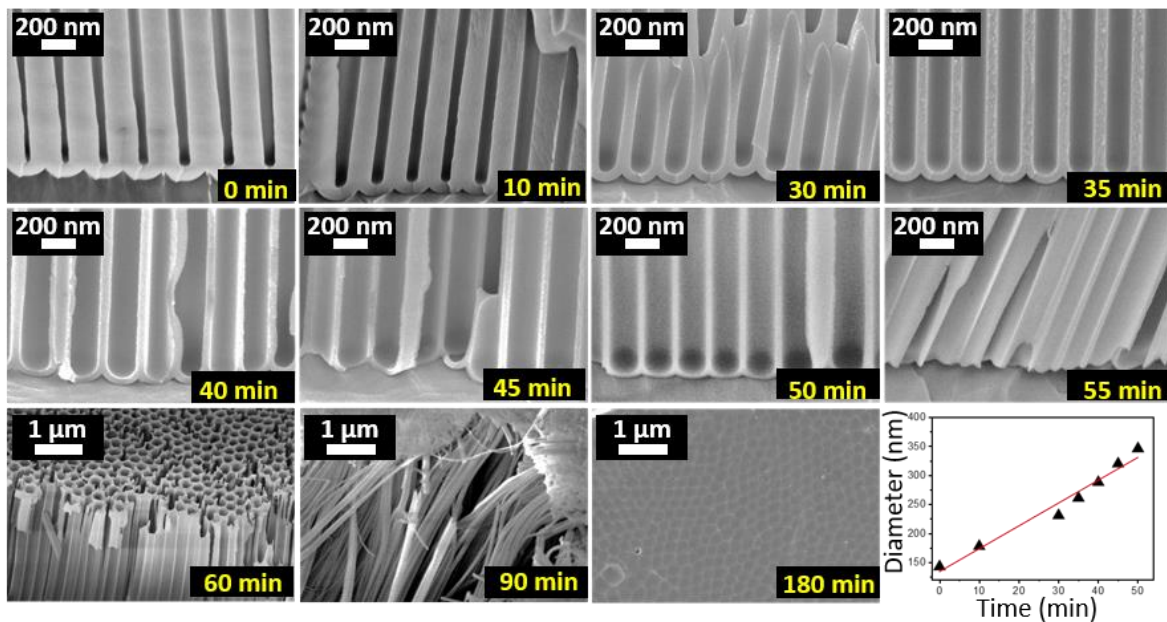


Figure 3.8. SEM image of AAO membrane upon different pore widening times and the plotted figure for the relation between pore diameter and treatment time.

3.7. Aluminum Removing

The length of fabricated AAO membranes was maximum 60 μm in the conducted experiments, however the thickness of aluminum disc was 0.5 mm. Hence a thick aluminum layer remained as substrate of the obtained AAO membrane. For some applications, the aluminum layer has to be removed and, in this case, a CuCl₂ and HCl aqueous solution was used for the dissolving of aluminum substrate at room temperature. After entirely removal of the Al layer, the left alumina displayed colorless or light white appearance.

3.8 Backside Opening

Additionally, in order to prepare the through-hole AAO membrane, an aluminum removing process and barrier layer wet etching process was essential to be applied. The AAO sample was mounted into PVC chamber with the aluminum layer exposed and the aluminum layer was removed in CuCl_2 and HCl aqueous solution for 30 min at ambient temperature. Further the barrier layer was removed by treated with 10 wt% phosphoric acid, at 45 °C for 20 min, 50 min, 100 min, 150 min, 180 min and 200 min, respectively. As illustrated in Figure 3.9, the pore starts to open after 100 min, but reveals uneven pore sizes. When further extending the etching time, uniform perforated pores can be obtained after 150 min. At 180 min, the pore sizes are further enlarged to ≈ 300 nm. As the treating time reached 200 min, some defects of the membrane pores started and collapsed indicating the maximum backside pore opening had been reached. The optimized backside opening time was between 150 min and 180 min, depending on the different requests for the through hole pore size, the etching time could be tuned with in this period. After the success backside pore opening process, through-hole AAO membranes were obtained which could be further used as filtration membranes.

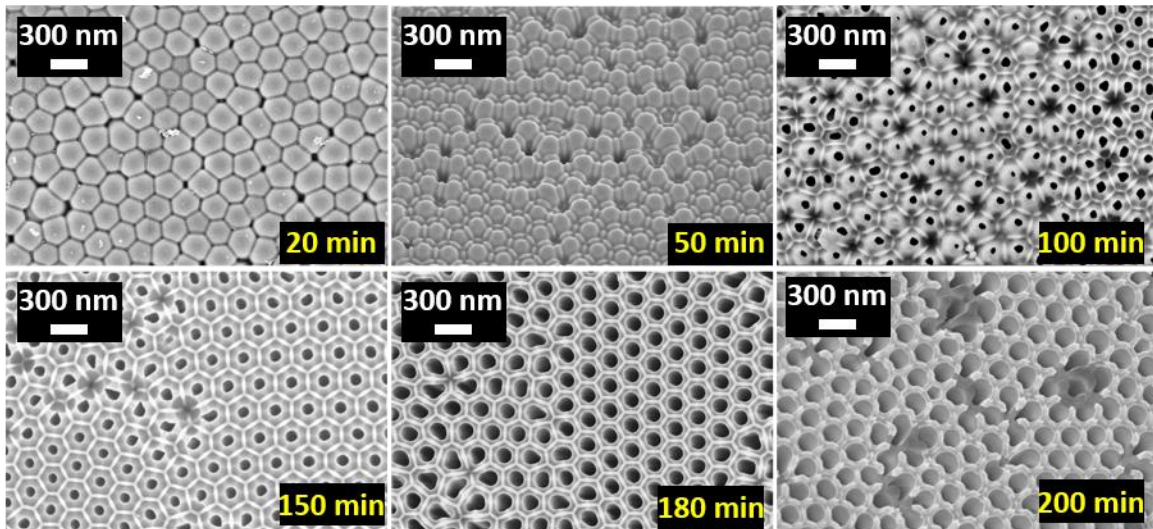


Figure 3.9. SEM images of backside surface of AAO membrane after wet etching for 20 min, 50 min, 100 min, 150 min, 180 min and 200 min.

3.9. Conclusion

According to the two-step anodization method, in this chapter, AAO membranes with uniform self-ordered cylindrical-pores have been fabricated. The pore size of AAO membranes fabricated from oxalic acid was ≈ 30 nm, while phosphoric acid was ≈ 200 nm. Furthermore, taking phosphoric acid anodization as an example, a series of AAO membranes were fabricated upon diverse anodization time, the results revealed that pore length of obtained membrane is linearly proportional to the second anodization time. Besides, the post modification process can be used for adjusting the pore diameter. Under 45 °C in 10 wt% aqueous phosphoric acid, the pore size of AAO membrane is also proportional to the treatment time with an increment speed of 3.93 ± 0.31 nm/min. However, extended treatment above 1 h, the pore structures are no longer maintained. The method mentioned above for controlling the pore size and diameter could be combined for the fabrication of AAO membranes with customized aspect ratios. Additionally, AAO membranes with different geometric structures were also obtained from sequential anodization with different electrolyte, furthermore, by selectively removing the aluminum substrate and backside barrier-layer, through-hole membrane with various channel sizes were prepared which enabled the templates to be used in the field of filtration, sieving and separation. This chapter builds a solid foundation for the next chapters, which expand the possibility of versatile smart AAO membranes.

4. Polymeric One-dimensional Janus Nanorods via AAO Templating

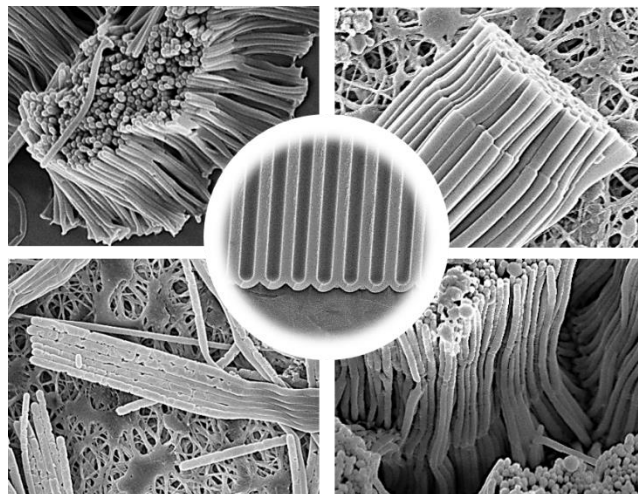


Table of content graphics of chapter 4.

4.1. Introduction

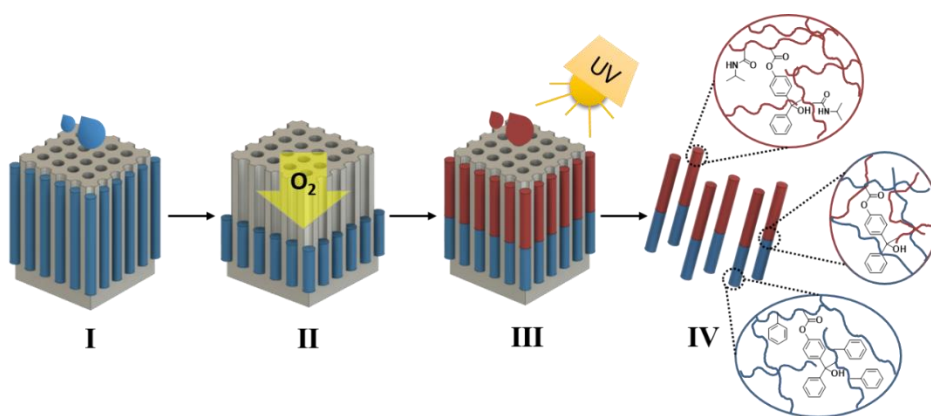
Janus nanoparticles, named after a Roman god who has two opposite and distinct faces, are asymmetry nanoparticles that consist of distinct chemical or physical properties. Indeed, the dual nature of Janus nanoparticles offers them diverse properties to target complex self-assembled structure or response to multiple stimuli or distinct surface properties which are inconceivable for homogenous particles.^[166] Multifunctional Janus nanoparticles show potential applications as solid surfactant,^[167] drug delivery,^[168] self-propelled nanomotors,^[169] or building blocks towards specific superstructures,^[170] etc. Owing to their bright perspective for application, in the past few decades, fabrication of Janus nanoparticles has been extensively reported. Thus, plenty of Janus nanoobjects have been attained, from the simplest spherical to different heterotype such as dumbbell-form or disk-shaped, or even cylindrical-shaped. In fact, nanorods, nanotubes, and nanowires have high aspect ratio and offer superior applications to build two- or three-dimensional nanostructures.^[171] For instance, via a seeded emulsion polymerization, Park *et al.* has fabricated a dumbbell-shaped Janus nanoparticle that consists of hydrophobic polystyrene and hydrophilic poly(styrene-*co*-trimethoxysilypropylacrylate) patches.^[172] This amphiphilic Janus nanoobject provided new

building blocks for three-dimensional photonic crystals. So far, many techniques have been used to fabricate Janus nanoparticles, such as Pickering emulsion polymerization, surface-initiated polymerization, fluidic nanoprecipitation and template method.^[173,174] In the midst of nanostructure fabrication method, template synthesis method is a cost-effective method for preparing one-dimensional nanostructures with a high throughput.^[131] As aforementioned, AAO template is one of the widely used templates which is applied in preparation of nanoobjects. Indeed, Choi *et al.* fabricated asymmetric nanopillars by coating polyurethane acrylate nanopillar obtained from AAO template with gold.^[175] While Hurst *et al.* reported that by means of AAO template synthesis, metal-polymer Janus nanorods could be prepared. The latter Janus nanoobject consisted of two components, an Au block and a polypyrrole block, which could self-assemble into different superstructures.^[171] Although substantial research has been performed for the preparation of one-dimensional Janus nanostructures, majority of these works is focusing on inorganic-inorganic or polymer-inorganic nanostructures. Interestingly, seldom research has been reported about the preparation of polymeric Janus nanostructures via AAO templating. As a matter of fact, polymers are good candidates to replace heavy metals that are utilized in the fabrication of Janus particles. Particularly, due to the fact that polymeric materials have better processability that may facilitate the nanostructure fabrication. In addition, polymeric materials may possess additional functional groups which could even facilitate post-polymerization modification.^[176–178] In this regard, preparation of multicomponent polymeric nanostructures is of particular interest. By infiltrating polymer or monomer into hexagonally well-ordered pores of AAO template, nanostructures can be obtained. The infiltration can be accomplished by wetting with either melts or solutions.^[179] Additionally, owing to the tunable pore dimensions of AAO template, nanostructures differ from length and diameter easy to be achieved.

On this account, a generally applicable strategy for the fabrication of diverse polymeric Janus nanorods was developed by alternating chemical components via sequential polymerization in AAO template. As a reference, amphiphilic polystyrene-*block*-poly(*N*-isopropylacrylamide) (PS-*b*-PNIPAm) Janus nanorods were first fabricated. Since the two blocks are chemically bonded, Janus nanorods can maintain their shape after dissolving out of the template. In fact, the known anisotropic property of Janus nanorod has potential applications in the field such as drug delivery. In addition, this method can be widely spread for the preparing multi-component nanorods.

4.2. Strategy

In this work, a simple and efficient route for fabricating polymeric Janus nanorods bearing a poly(*N*-isopropylacrylamide) (PNIPAm) block and a polystyrene (PS) block is proposed. Styrene monomer is selected owing to its easy to synthesize and PNIPAm vs PS blocks are distinguishable via TEM. By using low cost anodic aluminum oxide (AAO) as template, the nanorods can be prepared uniform in shape together with a high throughput. Following the process illustrated in Scheme 4.1, the PS nanorods were first formed via *in situ* polymerization. In detail, a stock solution, which consists of styrene monomer, crosslinker, photo-crosslinker (i.e. 4-acryloylbenzophenone) and thermal radical initiator (i.e. 2,2'-azobis(isobutyronitrile), was prepared in anhydrous 1,4-dioxane. Accordingly, the prepared stock solution was drop casted onto AAO template followed by thermo-initiated polymerization.



Scheme 4.1. Proposed route for the fabrication of polystyrene-*b*-poly(*N*-isopropylacrylamide) (PS-*b*-PNIPAm) Janus nanorod. (I) *In situ* polymerization of first polystyrene block; (II) oxygen plasma treatment; (III) *in situ* polymerization of second poly(*N*-isopropylacrylamide) block and post-UV-crosslinking; (IV) dissolution of AAO template and release of polystyrene-*b*-poly(*N*-isopropylacrylamide) (PS-*b*-PNIPAm) Janus nanorod.

Subsequently, oxygen plasma treatment was conducted in order to eliminate the partially formed PS nanorods, and crucially to generate sufficient space for the polymerization of second block. Thereafter, PNIPAm nanorods were formed in AAO template on the top of each PS nanorod by adopting similar conditions. Ultimately, post-crosslinking was induced under UV treatment in/between PS and PNIPAm nanorods, Janus nanorods were obtained after dissolving the AAO template. With the introduction of 4-acryloylbenzophenone, the formed two blocks are chemically

connected into a single Janus nanorod. Importantly, the two blocks could be replaced by using different functional monomers, thus building various functionalized Janus nanorods.

4.3. Results and Discussion

In order to monitor the transformation of morphologies during fabrication process, SEM images of nanostructure samples were recorded at each step. From Figure 4.1 A, it can be seen that nanorod structures were formed which filled completely the nanocavities of AAO template, thus indicating the successful fabrication of PS nanorod via *in situ* free-radical polymerization. Further, oxygen plasma treatment was carried out to partially remove parts of the formed PS nanorods. During oxygen plasma treatment, generated oxygen plasma induced polymer etching that led to vanishment of PS nanorod. By adjusting the treatment time to 30 min, approximately 1 μm of PS block was removed as recorded in SEM image shown in Figure 4.1 B.

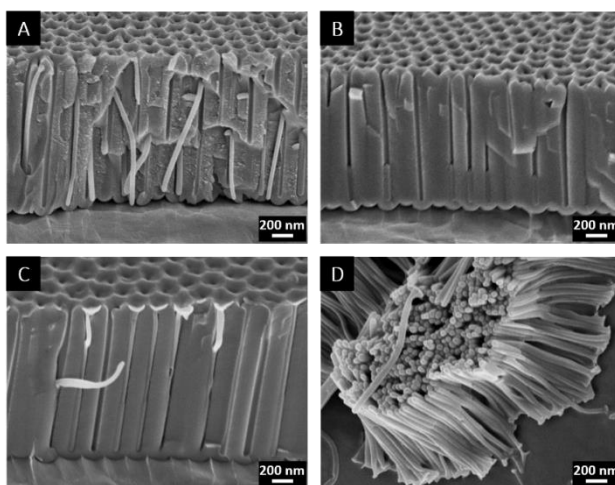


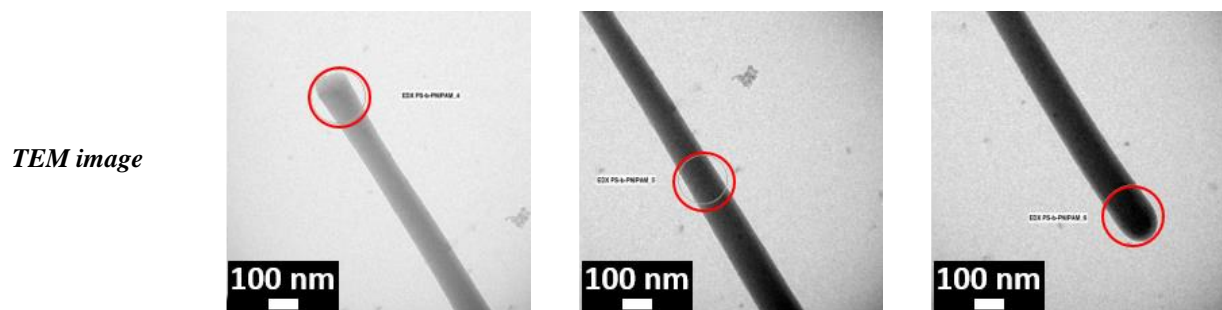
Figure 4.1. SEM images of (A) PS nanorods completely filled AAO template, (B) half-filled PS nanorods in AAO template, (C) PS-*b*-PNIPAm Janus nanorods in AAO template, (D) bundles of crosslinked PS-*b*-PNIPAm Janus nanorods.

Afterwards, a second free-radical polymerization was processed in the template, resulting in the formation of PNIPAm block in the membrane nanocavities above PS block. UV irradiation was then applied. Upon UV irradiation, benzophenone units present in both PS and PNIPAm blocks led to a crosslinking between the PS block and PNIPAm block.^[180] Figure 4.1 C illustrates the SEM image of PS-*b*-PNIPAm Janus nanorods within the AAO template. A small junction between PS

block and PNIPAm block could be observed. After dissolving AAO templates in 10 wt% aqueous H_3PO_4 , the samples were filtered and washed thoroughly with DI water, images of the collected Janus nanorods are recorded in Figure 4.1 D. As revealed, bundles of Janus nanorods were observed and all samples maintained a distinct junction, which demonstrated the successful fabrication of Janus nanorods. Subsequently, TEM measurement as well as energy-dispersive X-ray (EDX) spectroscopy were carried out to further depict the composition of Janus nanorods and the results are recorded in Table 4.1. As illustrated, the top part of PS-*b*-PNIPAm Janus nanorod contained highest amount of nitrogen along the Janus nanorod. This phenomenon is in accordance with the fact that the top block of Janus nanorod consisted of PNIPAm, which contains nitrogen atoms in the polymer chains. However, smaller amount of nitrogen can also be found in the middle and bottom of the nanorods. This could be attributed to the nitrogen atmosphere in TEM sample chamber or the nitrogen resulting from the initiator. Additionally, it could be distinguished from the TEM images that the PS block is represented darker than the PNIPAm block, owing to the higher electron density of PS than that of PNIPAm. As a consequence, the formation of Janus nanorods has been successfully demonstrated.

Table 4.1. Comparison of element component at top, middle and bottom point of PS-*b*-PNIPAm Janus nanorod.

<i>Element</i>	<i>Top</i>		<i>middle</i>		<i>bottom</i>	
	<i>Weight %</i>	<i>Atomic %</i>	<i>Weight %</i>	<i>Atomic %</i>	<i>Weight %</i>	<i>Atomic %</i>
<i>N</i>	66.7	69.7	24.9	27.5	27.0	29.7
<i>O</i>	32.7	30.0	74.8	72.3	72.7	70.2
<i>P</i>	0.6	0.3	0.2	0.1	0.3	0.1



Supplementary, the fabrication method is capable to prepare diverse Janus nanorods by varying monomer species. Indeed, via adopting the same strategy, Poly(*N*-isopropylacrylamide)-*b*-Poly(pentafluorophenyl acrylate) (PNIPAm-*b*-PPFPA) nanorods were then prepared. The obtained

reactive Janus nanorods were also characterized by SEM to record their morphology and the results are illustrated in Figure 4.2. However, unlike PS-*b*-PNIPAm, the junctions between PNIPAm-*b*-PPFPA nanorods are hard to be distinguished.

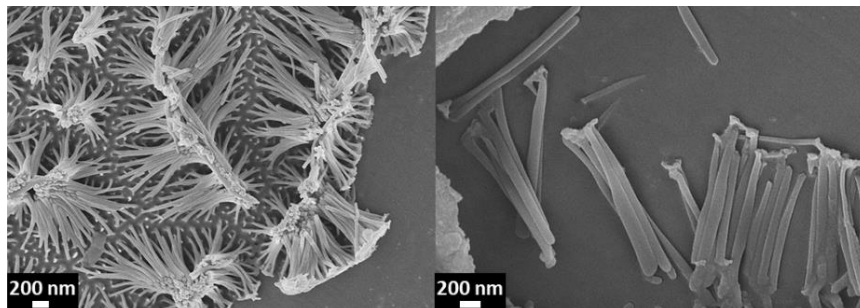


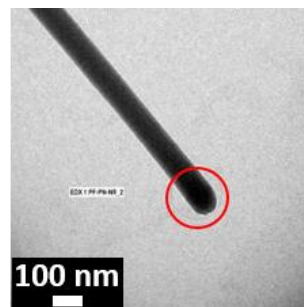
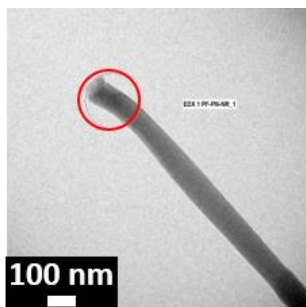
Figure 4.2. SEM images of PNIPAm-*b*-PPFPA Janus nanorods.

Furthermore, in order to prove the strict composition in PNIPAm-*b*-PPFPA nanorods, compositional TEM and EDX analysis of PNIPAm-*b*-PPFPA Janus nanorods was carried out. The obtained results are illustrated in Table 4.2.

Table 4.2. Comparison of element component at top and bottom point of PNIPAm-*b*-PPFPA Janus nanorod.

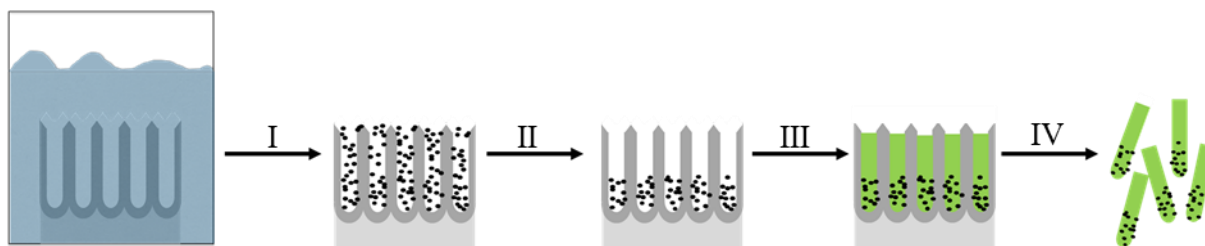
<i>Element</i>	<i>Top</i>		<i>bottom</i>	
	<i>Weight %</i>	<i>Atomic %</i>	<i>Weight %</i>	<i>Atomic %</i>
<i>N</i>	57.0	60.5	11.6	13.5
<i>O</i>	41.5	38.5	66.7	68.0
<i>F</i>	0.9	0.7	21.2	18.2
<i>Al</i>	0.2	0.1	0.1	0.1
<i>P</i>	0.2	0.1	0.2	0.1
<i>S</i>	0.3	0.1	0.2	0.1

TEM image



Obviously, the content of nitrogen in the top block is much less than that in bottom block, which was in accordance with the composition of each block; in other words, the bottom PNIPAm block contains nitrogen while the top PPFPA block doesn't. However, residual small amount of nitrogen may again be attributed to the atmosphere of sample chamber or remains of the thermal initiator. On the contrary, fluorine was found 21.2 wt% in the top PPFPA block, while only traces of fluorine element content are found in PNIPAm block. Which confirmed the composition of each block in Janus PNIPAm-*b*-PPFPA nanorods. In addition, electron density differences as well as the junction between two blocks are clearly distinguished in the TEM images, ultimately proving that PNIPAm-*b*-PPFPA Janus nanorods were obtained.

As mentioned above, Janus nanorods bearing chemical compositional difference are easy to be fabricate via AAO templating strategy. In order to prepare Janus nanorods, which not only differ in chemical composition but also in shape morphology, complex Janus nanorods which composed of polypyrrole nanoparticle (PPYNP) block and poly(methyl methacrylate) (PMMA) block are fabricated. The detailed fabrication process is illustrated in Scheme 4.2.



Scheme 4.2. Schematic illustration of preparing PPYNP-*b*-PMMA Janus nanorods.

In detail, the as-prepared AAO membrane was first immersed into an aqueous solution which consisted of NaOAc, FeCl₃ and pyrrole, and subsequently the mixture was sonicated for 1 h at room temperature. During sonication, pyrrole was polymerized under oxidation of FeCl₃ and transformed into polypyrrole nanoparticles, which were spread on the template surface and in the membrane pores, respectively. Upon cleaning, SEM analysis was performed of AAO template, and subsequently an optical image was recorded, as shown in Figure 4.3. It could be observed that after the sonication, polypyrrole nanoparticle are formed and distributed homogenously on AAO surface as well as inside of membrane channels (I in Scheme 4.2).

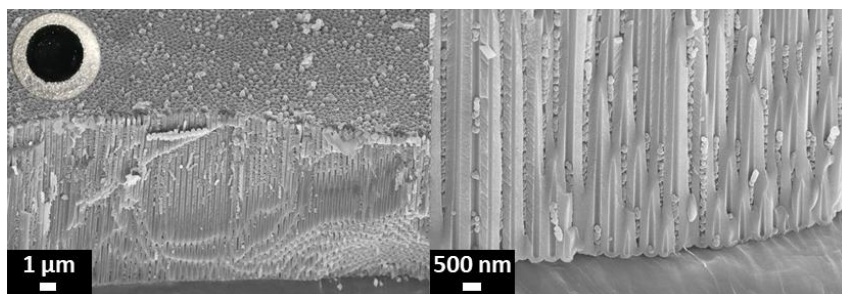


Figure 4.3. Optical image and scanning electron micrographs of PPYNP in AAO template.

Afterwards, the PPYNPs filled template was exposed to oxygen plasma in order to remove the redundant PPYNPs and leave space for the polymerization of second block in the AAO channels (II in Scheme 4.2). Following, a PMMA block was then synthesized under confinement in AAO template (III in Scheme 4.2), and dispersed Janus nanorods were obtained after dissolving the AAO template (IV in Scheme 4.2). SEM images of polypyrrole nanoparticle-*block*-poly(methyl methacrylate) (PPYNP-*b*-PMMA) Janus nanorods were recorded as shown in Figure 4.4. It can be clearly observed from the Figure 4.4 that Janus nanorods are composed of distinct two part, as expected; the rough block is stack by polypyrrole nanoparticle, while the smooth block consisted of PMMA.

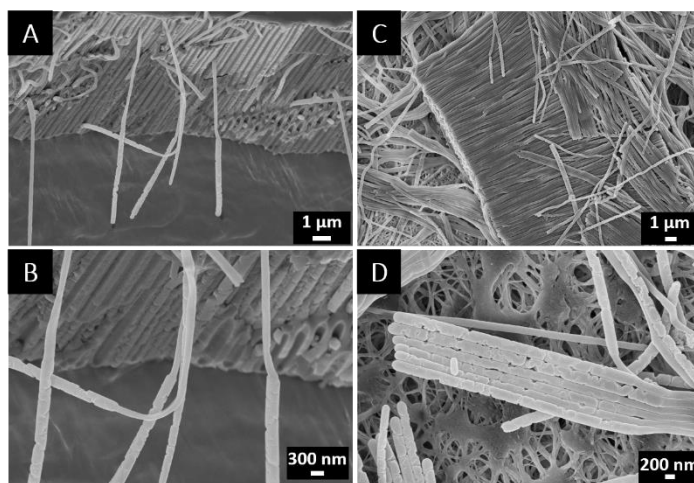
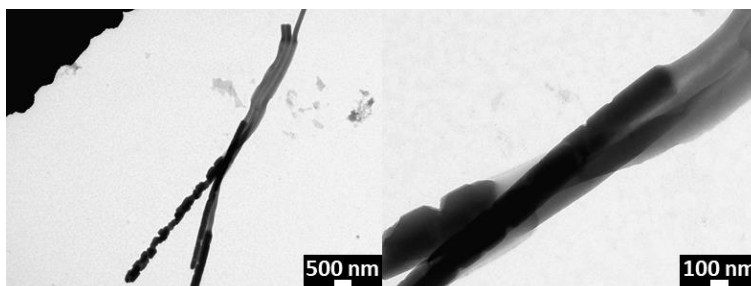


Figure 4.4. Scanning electron micrographs of PPYNP-*b*-PMMA Janus nanorods (A, B) in AAO template and (C, D) free dispersed.

Moreover, in order to further visualize the compositional structure of PPYNP-*b*-PMMA Janus nanorods, TEM was carried out and shown in Figure 4.5. From the TEM image, two distinguishable

blocks could be observed in one single nanorod, which confirmed the successful Janus fabrication. The formed Janus nanorods do not only differ in chemical composition, but also reveal different morphology.



*Figure 4.5. Transmittance electron micrographs of PPYNP-*b*-PMMA Janus nanorods.*

4.4. Conclusion

To conclude, three kinds of polymeric Janus nanorods have been successfully fabricated via AAO templating. The PS-*b*-PNIPAm and PNIPAm-*b*-PPFPA nanorods differed in chemical composition, additionally, Janus nanorods bearing stimuli-responsive polymer blocks have potential application in controlled drug release. Besides, PPYNP-*b*-PMMA nanorods depict difference in composition and shape are also achievable. Additionally, due to specific optical performance of PPYNP, this kind of Janus nanorods are able to be used as self-propelled nanomotors.

The results demonstrate that various kinds of Janus nanorods which differ in chemical composition or/and shape can be produced by employing a simple template-based strategy. Clearly, benefits of the approach presented here are not limited to the materials mentioned above, thereby opening up a plenty of new possibilities for fabricating complex nanostructures with potential applications in surfactant, building blocks for self-assembling or optical devices.

5. Hierarchical Superoleophobic Film with Reversible pH Response from AAO Patterning

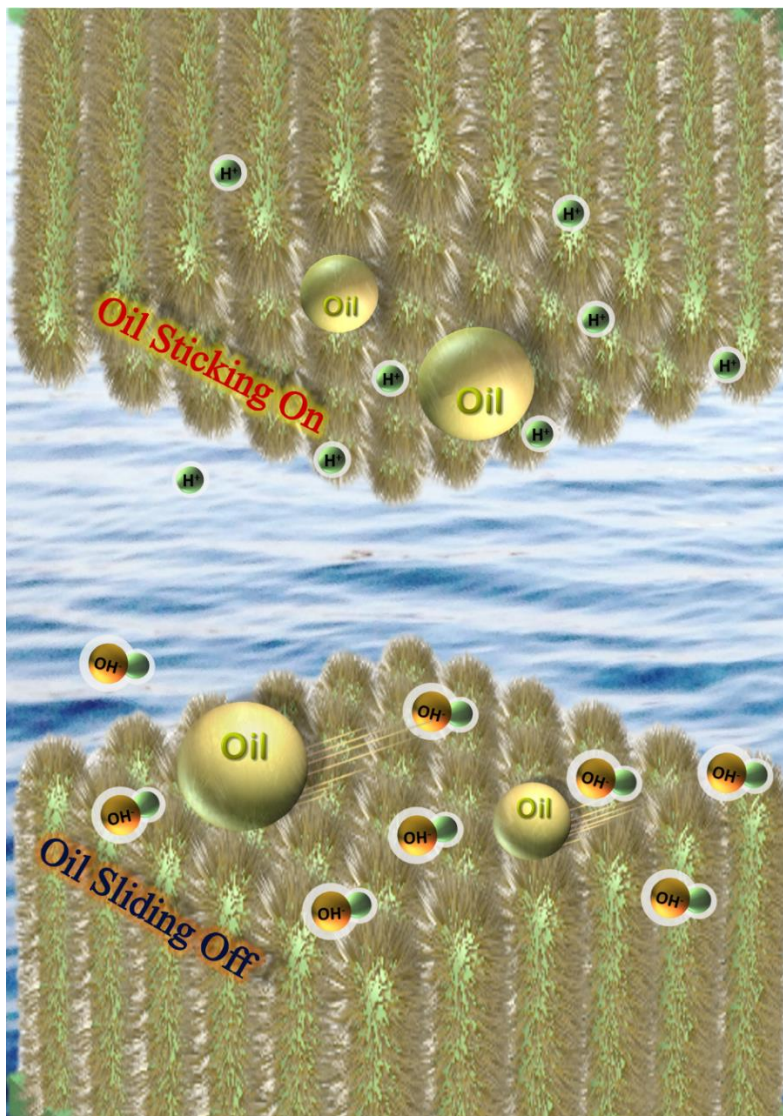


Table of content graphics of Chapter 5.

Adapted with permission from Ref. [181], copyright (2020) John Wiley and Sons.

Part of the current chapter are adapted or reproduced from reference^[181]: Xia Huang, Hatice Mutlu, Patrick Théato*. *A bio-inspired hierarchical anti-oilfouling surface with reversible pH response. Advanced Materials Interfaces*, with permission from Ref. [181], copyright (2020) John Wiley and Sons.

5.1. Introduction

Nature offers many biological materials that consist of ordinary compositions, but possess more than one function, owing to their inherent hierarchical structuring ranging from nano- to micro- to macro-dimensions.^[182] For instance, seabirds are endangered by polluting from waste oil, submarines and boats are contaminated by plankton but fish can keep clean in oil polluted water. Scales provide fish the ability of swimming freely in oil contaminated water from being soiled which showed an underwater superoleophobic performance. This behavior owing to the chemical composition and hierarchical morphology of fish scales. Fish scales are mainly composed of protein and calcium phosphate which forming a micropapillae bestrewed surface, further covered with a mucus thin layer on top. It's worth nothing that, skin of filefish is endowed with high oil repellence property due to the binary cooperation of hydrophilic chemical composition (e.g. calcium phosphate and protein) and fine-scaled rough microstructures (e.g. oriented micropillar arrays with length of 100~300 μm and width of 30~40 μm), which are distributed homogenously on the surface of the scales.^[183]

Nowadays, artificial superoleophobic surfaces which display contact angle greater than 150° against organic liquids in aqueous environment are widely studied in the past decades owing to their underwater excellent oil-repellent ability.^[184–186] Such materials have potential applications in the field of droplet manipulation in microfluidics,^[187] anti-oil contamination,^[188] resistance reducing of oil transportation,^[189] anti-biofouling,^[190] industrial metal cleaning^[191] and oil/water separation.^[192] Inspired by nanostructured fish scale, Ma *et al.* prepared an artificial underwater superoleophobic surface via layer-by-layer assembly of poly(acrylic acid) and poly(ethylene imine) on poly(methyl methacrylate-*co*-*N*-(3,4-Dihydroxyphenethyl) methacrylamide) substrate. Oil droplet reveal sphere on the achieved surface with contact angle of $\approx 163.1^\circ$ underwater.^[193] Besides, Liu *et al.* created a low-adhesive superoleophobic surface on a solid substrate through a double template replica method, this functional surface shows high oil repellent and the fabrication approach had opened new avenues for facilitating the introduction of oleophobic properties to common substrates.^[194]

Despite a high oil contact angle, the control of oil-adhesion property endows superoleophobic surfaces smart superior performance. Superoleophobic surfaces with low oil adhesion demonstrating strong anti-oil ability; on the contrary, with high oil adhesion the oil droplet can stick onto superoleophobic surfaces at any titled angle which is able be used to non-loss droplet

transport without any oil contamination, and further demonstrate great application prospect in the field of bio-adhesion, microfluidic technology, etc.^[195–197] Consequently, application of superoleophobic materials will be expanded if the oil-adhesion ability of could be adjusted on demand. Indeed, contradictory proposal can be realized with the aid of stimuli-responsive polymers. To date, multifunctional superoleophobic surfaces with adjustable oil adhesion have been achieved by means of electrochemical deposition,^[198] laser ablation,^[199] self-assembly,^[200] chemical etching,^[201] spray/dip coating,^[184] the template method,^[122] lithography,^[202] electrochemical anodization,^[203] and the hydrothermal method,^[204] etc.

Of varied methods, template method is of particular ideal option for mimicking nanostructured superoleophobic surfaces. Noteworthy, porous anodic aluminum oxide (AAO)^[205] with high areal density (up to 10^{11} pores per cm^2) and narrow size distribution has received much attention for its precise size control on preparation of nanostructures, as well as their excellent thermal and mechanical stability during templating nanoimprinting. Over the past decades, AAO template has been widely used for nanopatterning in various fields, including energy storage and conversion,^[206] sensors,^[207] optical devices,^[208] molecular separation,^[209–211] catalysis,^[59] tissue engineering,^[212] drug delivery^[213] as well as other applications and aspects.^[214–217]

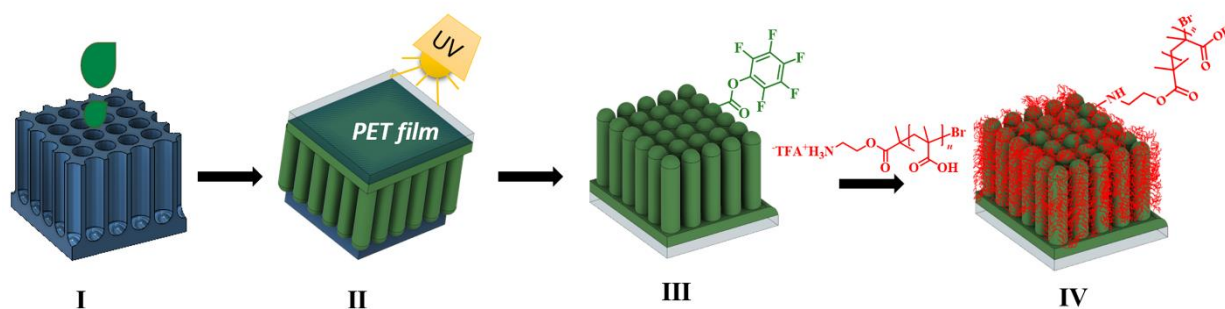
As this regard, AAO patterning has been adopted for constructing of superoleophobic surface.^[218] Moreover, in order to simplify fabrication process and broaden applicability of the AAO template method for the fabrication of smart superoleophobic surfaces, post-polymerization modification, an emerged powerful tool for polymer chemists to construct complex macromolecular structures has been proposed. In particularly, it is an irreplaceable strategy for the fabrication of smart surfaces from reactive precursor polymers while dispense complicated polymerization synthesis process.^[219–221] Previously, our group had presented that polymer materials embellished with pentafluorophenyl (PFP) ester groups are promising precursors for post-polymerization modification, owing to their high reactivity with diverse amines under a very mild reaction condition and yielding versatile functionalized polymer materials, which could not be accessible otherwise.^[58,59] As a consequence, we are particularly interested in constructing nanostructured superoleophobic surfaces with smart reversible property via synergy of AAO template methodology and post-polymerization modification strategy.

In this project, it was aimed to prepare an underwater superoleophobic surface with pH switchable oil adhesion property by the combination of AAO template method and post-polymerization

modification strategy. The active ester bearing poly(pentafluorophenyl acrylate) (PPFPA) micro-pillar arrays are firstly prepared from *in situ* polymerization in porous aluminum oxide template, and subsequently, amine ended poly(methacrylic acid) (PMAA) brushes are grafted on to free PPFPA pillars via catalyst free esterification between amine groups and PFP units. The morphology and surface property of the formed hierarchical surface are comprehensively investigated. Results demonstrated obtained surface featured with underwater superoleophobicity and reversible pH-switchable oil-adhesion property. Furthermore, it is presumed that this facile approach paves the way for the designing of smart oil-manipulating surfaces for the potential application in marine environment.

5.2. Strategy

Scheme 5.1 schematically illustrates the fabrication procedure for PMAA nanobrushes grafted PPFPA pillar (pillar-PPFPA-g-PMAA) hierarchical surfaces. Initially, highly ordered AAO template featuring hexagonal porous structure was pre-prepared via conventional two-step anodization process.^[205] In order to enlarge the nanocavities of the porous structure, pore-widening process was then carried out, delivering an AAO template which consists of homogenous cylinder pores.



Scheme 5.1. Schematics of fabrication procedures (I) drop casting the precursor liquid onto beforehand AAO template; (II) UV initiated polymerization in nanopores; (III) dissolution of AAO template and release of pillar-PPFPA texture free stand on the substrate of PET; (IV) grafting of PMAA nanobrushes onto pillar-PPFPA via post-polymerization modification. Adapted with permission from Ref. [181], copyright (2020) John Wiley and Sons.

For smart surface fabrication, pillar structured PPFPA were firstly fabricated by replicating nanopores of AAO template (I in Scheme 5.1). In detail, monomer stock solution that contains monomer, crosslinker as well as photoinitiator was drop casted onto the as prepared template and then immediately covered with silanized PET substrate above; thereafter, photo-initiated polymerization was carried out (II in Scheme 5.1), PPFPA pillar arrays were solidified under confinement. Subsequently, AAO template that contains PPFPA pillars was processed to be dissolved in acidic solution, afterwards PPFPA pillars were released out of AAO template (III in Scheme 5.1). Upon thoroughly washed and dried, PPFPA pillar arrays on PET substrate were obtained. The whole film was then immersed into amino-ended PMAA polymer/dimethylsulfoxide solution, and post-polymerization modification^[223] for the synthesis of the tethered PMAA brushes onto PPFPA pillars (IV in Scheme 5.1) was carried out. Once modification process reached equilibrium, pillar-PPFPA-g-PMAA films were obtained after thoroughly washed against ethanol, water and subsequently dried.

5.3. Results and Discussion

Morphology of pristine AAO membrane was recorded via SEM characterization and obtained images were illustrated in Figure 5.1. As revealed, after anodization and pore widening in H_3PO_4 , hexagonally arranged cylinder nanopores were acquired with an average pore length of $\approx 3 \mu m$ and pore diameter of $\approx 300 nm$.

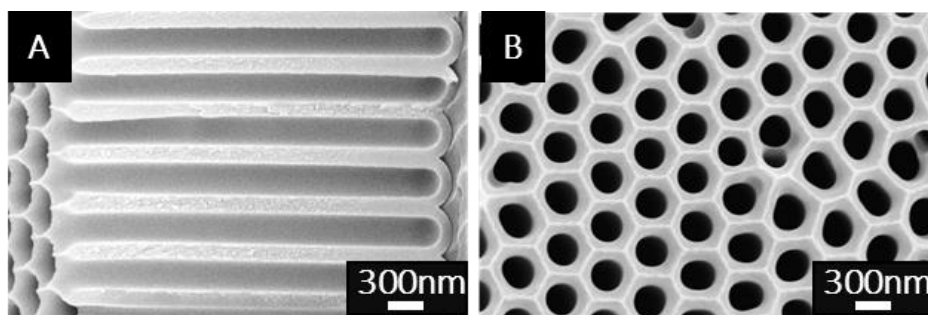


Figure 5.1. The SEM images of fabricated AAO template with (A) cross section and (B) top view, respectively. Adapted with permission from Ref. [181], copyright (2020) John Wiley and Sons.

The obtained AAO membrane was further utilized for nanopatterning. For constructing cylindrical nanorods with $\approx 300 nm$ in diameter and $\approx 3 \mu m$ in length. Benefit from suitable length-to-diameter

ratio, the formed nanorods are stable enough from collapsing. Indeed, after *in situ* polymerization of PFFPA in AAO membrane, the pillar array structure was obtained via template replicating. According to the SEM images (Figure 5.2 A and B), the free PFFPA pillars are with identical contour of the pore structure from the pre-prepared AAO template, manifesting the successful duplication of pillars by a template imprinting approach. Besides, the pillar-PFFPA shows free stands countenance, which confirmed an appropriate surface structure. Afterwards, post-polymerization modification process was carried out; pre-synthesized amine-ended-PMAA brushes were mounted onto the pillar-PFFPA arrays. In order to monitor the transformation of morphology, SEM was carried out after the modification process, as showed in Figure 5.2 C and D, respectively. The SEM images depict that pillar-PFFPA-g-PMAA remained and kept free-stand on the substrate, thus revealing the maintenance of pillar structures after post-polymerization modification.

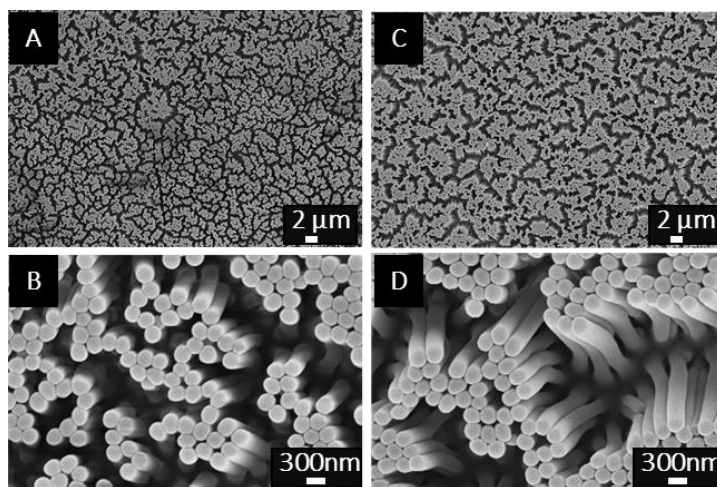


Figure 5.2. The SEM and magnified images of: (A, B) PFFPA-micro-pillars, (C, D) PFFPA-g-PMAA, respectively. Reprinted with permission from Ref. [181], copyright (2020) John Wiley and Sons.

During post-polymerization modification process, esterification occurred between amine groups from PMAA brushes and ester groups from PFFPA pillars; efficiency reaction conversion has been monitored by complementary FT-IR measurement at various reaction time intervals. The results are illustrated in Figure 5.3. As revealed, IR spectra of pure PFFPA pillar is labeled as 0 h, the characteristic bands at 1784 cm^{-1} (highlighted in blue) and 1517 cm^{-1} (highlighted in green) are ascribed to the PFP ester from PFFPA-pillars. Furthermore, upon post-polymerization modification

for 24 h, carbonyl stretching at 1724 cm^{-1} (highlighted in red) is observed which relevant to grafted PMAA brush.^[224] With the time increasing, the newly arising peak at 1724 cm^{-1} enlarged, simultaneously, the characteristic peaks belonging to PPFPA at 1784 cm^{-1} and 1517 cm^{-1} are diminished. After 36 h reaction, the esterification reached equilibrium, all characteristic peaks from IR spectra remained constant even after prolonging the reaction time to 48 h. Although the reaction reached equilibrium, carbonyl group stretching vibrations of PFP ester still remained with low intensity, disclosing an incomplete conversion even after 48 h reaction. This phenomenon can be attributed to the crosslinked molecular structure of the micropillars, which hindered reaction between the amino-end polymer brushes and the interior PPFPA pillars. However, since the superoleophobicity and oil adhesion properties of the pillar-PPFPA-g-PMAA surfaces should depend only on the conversion on the pillar surface, the incomplete esterification should have unneglectable impact on the results. As a consequence, based on above mentioned SEM results and FT-IR spectra, successful fabrication of PMAA grafted PPFPA pillar has been proved.

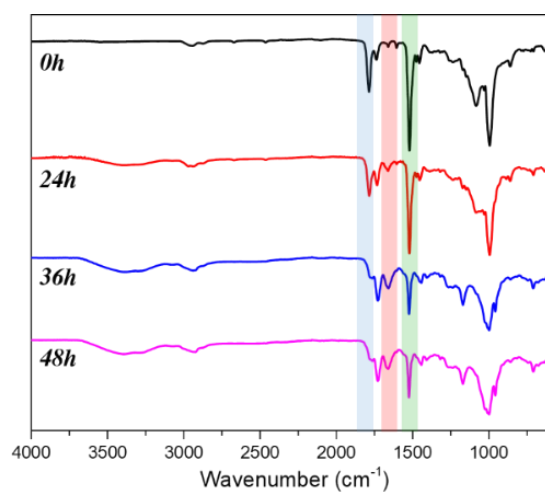


Figure 5.3. Comparative FT-IR spectra of pillar-PPFPA-g-PMAA via post-polymerization modification upon various reaction time intervals. Adapted with permission from Ref. [181], copyright (2020) John Wiley and Sons.

Moreover, in order to comprehensively investigate the influence of hierarchical structures on the surface wettability, a controlled group was also prepared with the same composition of pillar-PPFPA-g-PMAA but on a flat surface. The flat-PPFPA was first prepared via spin coating, and subsequently post-polymerization modification was carried out under the same condition for constructing of flat-PPFPA-g-PMAA film. The FT-IR spectra of flat-PPFPA and flat-PPFPA-g-

PMAA are shown in Figure 5.4 which demonstrated the successful preparation of flat-PPFPA-g-PMAA surface after esterification.

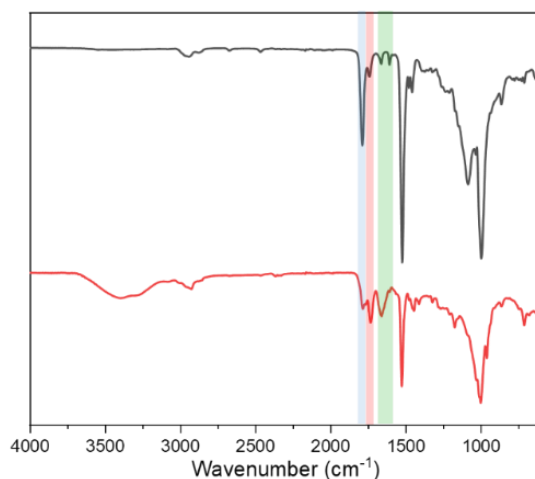


Figure 5.4. Comparative FT-IR spectra of flat-PPFPA (black line) and flat-PPFPA-g-PMAA (red line) after 36 h post-polymerization modification. Adapted with permission from Ref. [181], copyright (2020) John Wiley and Sons.

Thereafter, contact angle (CA) measurements of pillar(flat)-PPFPA and pillar(flat)-PPFPA-g-PMAA surfaces were evaluated in order to evaluate their surface wettability. The results are illustrated in Figure 5.5 and 5.6. As revealed from Figure 5.5, pillar-PPFPA surfaces depicting non-wetting properties with an elliptical geometry of the water droplet. Static water CA of pillar-PPFPA surface is $124\pm 4^\circ$ which exhibit inherently hydrophobicity. However, water CA of flat-PPFPA reveals only $\approx 85^\circ$. Indeed, the surface of flat-PPFPA is hydrophobic, but surface pillar structure increases hydrophobicity of PPFPA surfaces. Besides, from oil CA measurements, oil droplet spread fast in seconds on both the pillar-PPFPA surface and flat-PPFPA, thus revealing oleophilic characteristic both PPFPA film, as shown in Figure 5.5, B and D.

Noteworthy, after grafting PMAA brushes onto pillar-PPFPA surface, the water droplet can spread fast on pillar-PPFPA-g-PMAA surfaces with a final static contact angle of $20\pm 3^\circ$ as it is illustrated in Figure 5.6 A. The phenomena could be attributed to the wettability transformation of PPFPA pillar arrays from hydrophobic to hydrophilic after introduction of hydrophilic PMAA brushes through post-polymerization modification. In addition, oil droplet could also diffuse on the pillar-PPFPA-g-PMAA surface result in oil contact angle of $\approx 15^\circ$ as illustrated in Figure 5.6 B. Therefore, the surface maintains oleophilic in air. Besides, on flat-PPFPA-g-PMAA surface, water droplet

remains $\approx 45^\circ$ as shown in Figure 5.6 C. As a consequence, the aforementioned results demonstrate the ability of pillar-array nanostructures to enhance the hydrophilicity of hydrophilic materials.

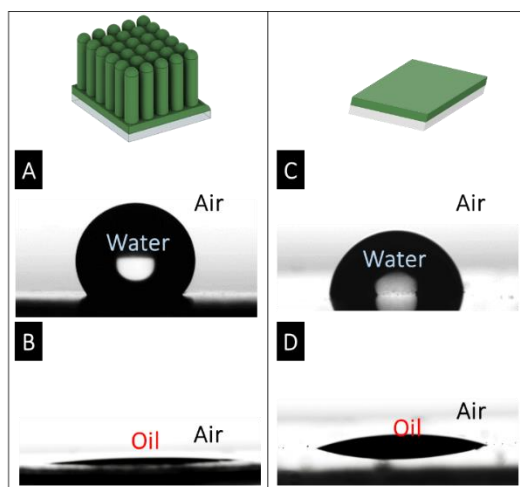


Figure 5.5. Images of CA measurements: (A) water CA of pillar-PPFPA surface, (B) oil CA of pillar-PPFPA, (C) water CA of flat-PPFPA surface, (D) oil CA of flat-PPFPA surface (water droplet $2\ \mu\text{L}$ and oil droplet $15\ \mu\text{L}$). Reprinted with permission from Ref. [181], copyright (2020) John Wiley and Sons.

Although, pillar structures enable wettability variation of obtained surfaces, the transformation reveals seldom practical application in air. In order to extend the application of the hierarchical membrane, further underwater properties of the fabricated surfaces have been studied. In fact, pH responsive polymers are able to undergo physical or/and chemical property transformation upon pH change. The weak polyelectrolyte brushes reveals pH-induced swelling and collapse, in similar manner to PMAA brushes. PMAA has a pK_a of ≈ 4.8 , at aqueous media with pH lower than 4.8, the pendant carboxylic acid groups from PMAA are protonated and coiled up forming intermolecular hydrogen bonds. On the contrary, when media pH is higher than 4.8, the PMAA polymer chains are stretched and form exclusively hydrogen bonds with the water molecules in the reaction medium. As a consequence, pH variations are capable lead to roughness transformation of PMAA grafted surfaces.^[225]

Accordingly, underwater oil wettability of flat-PPFPA-g-PMAA changed from oleophobic to superoleophobic as the pH value was increased, as illustrated in Figure 5.7 A. However unexpectedly, underwater oil contact angle of pillar-PPFPA-g-PMAA surface remained constant, when the pH value of the surrounding media was gradually added from pH 3 to pH 11. In this way

the pillar-PPFPA-g-PMAA surface maintained its superoleophobicity at any pH media by virtue of its hierarchical structuring (Figure 5.7 B). Indeed, when the pillar-PPFPA-g-PMAA surface is immersed under water, the pillars tend to be freely standing on the surface, and due to the high degree of surface roughness, water could be trapped forming an underwater Wenzel to Transition to Cassie state. Hence, the system is revealing constant superoleophobicity, which allows the utilization of pillar-PPFPA-g-PMAA surfaces in applications where mitigating oil fouling is crucial.^[218,226]

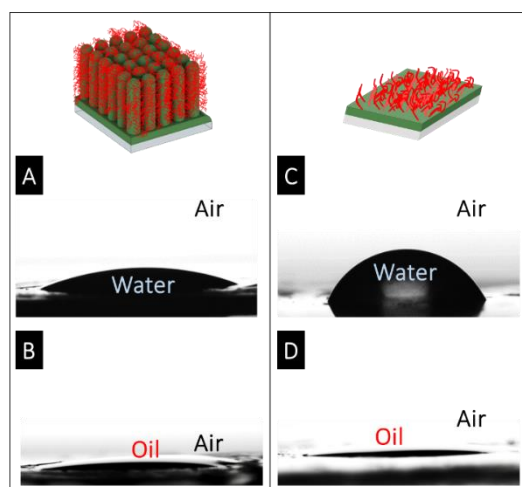


Figure 5.6. Images of CA measurements: (A) water CA of pillar-PPFPA-g-PMAA surface, (B) oil CA of pillar-PPFPA-g-PMAA surface, (C) water CA of flat-PPFPA-g-PMAA surface, (D) oil CA of flat-PPFPA-g-PMAA surface (Water droplet 2 μL and oil droplet 15 μL). Reprinted with permission from Ref. [181], copyright (2020) John Wiley and Sons.

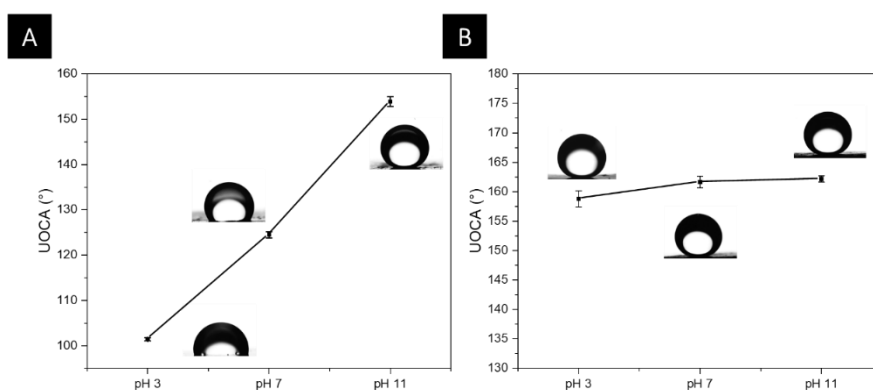


Figure 5.7. Underwater oil CA values and the corresponding images of (A) flat-PPFPA-g-PMAA and (B) pillar-PPFPA-g-PMAA surface at different pH values (oil droplet 15 μL). Reprinted with permission from Ref. [181], copyright (2020) John Wiley and Sons.

For the pillar-PPFPA-g-PMAA surface, although oil contact angle did not change critically within the examined pH range, their oil adhesion property altered dramatically in different pH media, as illustrated in Figure 5.8. Consequently, under acidic condition (pH=3), oil droplet adhered strongly to the hierarchical surface and did not slide off when the tilting angle reached 45°. The reason is that, when pH value is lower than pK_a of PMAA, polyelectrolyte brushes tend to collapse and dehydrate which in reverse results in generation of strong interaction and large contact area between surface and oil droplet. Accordingly, oil droplet fills the valleys of rough surface, therefore resulting in an underwater Wenzel state and showing high oil adhesion (schematic illustrated in Figure 5.8 B).^[218]

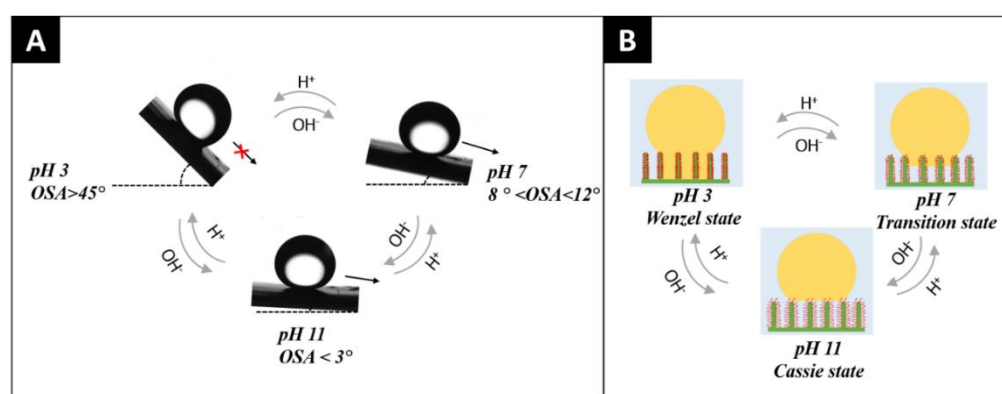


Figure 5.8. (A) Oil sliding angle images of pillar-PPFPA-g-PMAA at different pH conditions, and (B) schematic illustration of underwater Wenzel state, Transition state and Cassie state of oil droplet on the pillar-PPFPA-g-PMAA surface. Adapted with permission from Ref. [181], copyright (2020) John Wiley and Sons.

However, when pH value is increased above pK_a of PMAA and reached 7, oil droplet slid off already at a tilting angle of 8°. Moreover, with further increment of pH value, oil droplet started to with tilting angle of 3° slide at pH=11 media. The phenomena could presumably be ascribed to the fact that by increasing the pH values of aqueous media (e.g. higher than the pK_a of PMAA), the hydration of PMAA brushes was induced and accompanied by the stretching of the brushes which prevents the interacting between the oil droplet and the surface, hence results in a lower oil adhesion. However, at pH 7, the PMAA brushes are partially stretched, the oil droplet maintains partial penetration into the valleys of the rough surface, thus revealing an underwater transition state as it is implemented by the hysteresis of oil sliding. With further increase of the pH value, it is presumed that a full range extension of PMAA brushes will be observed, and the micro/nano-structured

roughness of the surface would tend to be pre-wetted by water, and trapped by a water layer underneath the oil droplet. Thus the pillar-PPFPA-g-PMAA film formed an underwater “Lotus” state (Cassie state) which results in an ultra-low oil adhesion of freely oil sliding property.^[122,227] The above-mentioned results are demonstrating the opportunity of tuning oil adhesion property of superoleophobic surfaces by varying pH value of media.

For comparison, the oil sliding angles of flat-PPFPA-g-PMAA surface were also measured, which are illustrated in Figure 5.9. Intriguingly, the oil droplet remained on the flat-PPFPA-g-PMAA even after reaching a tilting angle of 45°. Therefore, the results indicate indispensability of pillar structures with nanobrushes for the preparation of underwater superoleophobic surfaces with switchable oil adhesion property.

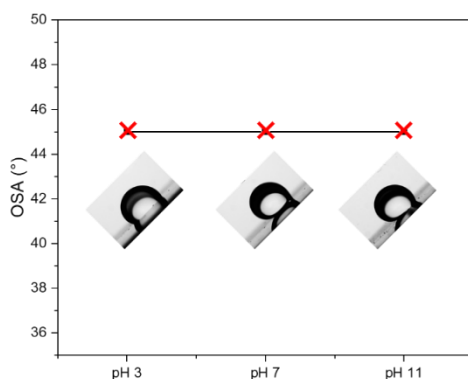


Figure 5.9. Oil sliding angle of flat-PPFPA-g-PMAA and inserted oil contact angle images with a tilting angle of 45° at different pH conditions (oil droplet 15 μ L). Reprinted with permission from Ref. [181], copyright (2020) John Wiley and Sons.

In order to further investigate the reversibility pH responsive oil adhesion properties of pillar-PPFPA-g-PMAA hierarchical surface, alternatively oil sliding angle measurement in solutions with pH value of 3, 7 and 11, was respectively carried out. As a model study, in total 5 consecutive cycles were processed. On trial, samples were immersed into the test solution and kept for 1 min to reach equilibrium prior the model study. Between each test, the sample was washed with ethanol and then rinsed with the test solution to eliminate any oil contamination. As illustrated in Figure 5.10, hierarchical superoleophobic surface shows good reversibility of oil sliding angle. In detail, while as the pH increased, the oil adhesion declined, hence manifesting the decrease of oil sliding angle. On the contrary, when the pH value was further decreased, the oil droplet was capable to stick onto the pillar-PPFPA-g-PMAA surface. After 5 measurements, the pillar structure

maintained on the surface without any damage, which demonstrated the durability of the functional surface, as it was confirmed via SEM measurements, depicted in Figure 5.11.

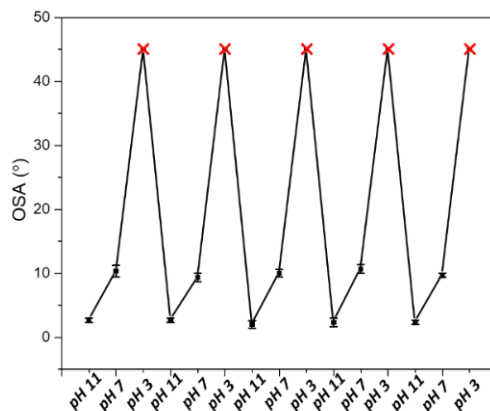


Figure 5.10. Cycling switchable oil sliding angle of pillar-PPFPA-g-PMAA upon pH stimulation. Adapted with permission from Ref. [181], copyright (2020) John Wiley and Sons.

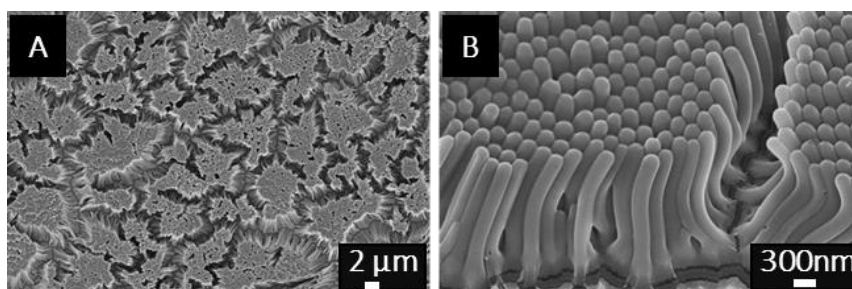


Figure 5.11. The SEM and magnified images of pillar-PPFPA-g-PMAA after 5 cycles of oil sliding angle measurement at pH 3, 7 and 11, respectively. Adapted with permission from Ref. [181], copyright (2020) John Wiley and Sons.

5.4. Conclusion

To sum up, hierarchical surface which consists of PPFPA micro-pillar arrays with grafted PMAA polymer brushes was fabricated by combining *in situ* AAO template polymerization methodology and post-polymerization modification strategy. As a result, the obtained micro/nano-dual hierarchical structural surface reveals tunable oil adhesion property while capable keep underwater superoleophobicity. Explicitly, under acidic conditions an oil droplet can be retained on the surface at any tilted angle which depicting a Wenzel state on the hierarchical surface. While upon neutral

and basic pH values, a Transition state to Cassie state is evolving, i.e. oil droplet is able to slide free on hierarchical surface. In addition, the pH stimulated oil sliding property reveals high reversibility. Correspondingly, the obtained hierarchical film exhibits great perspective in constructing oil-repellent and manipulate materials in marine industry. Furthermore, the proposed facile methodology paves the way for fabrication of various dynamic surfaces.

6. Carbon Dioxide Gated AAO Based Nanocomposite Membrane

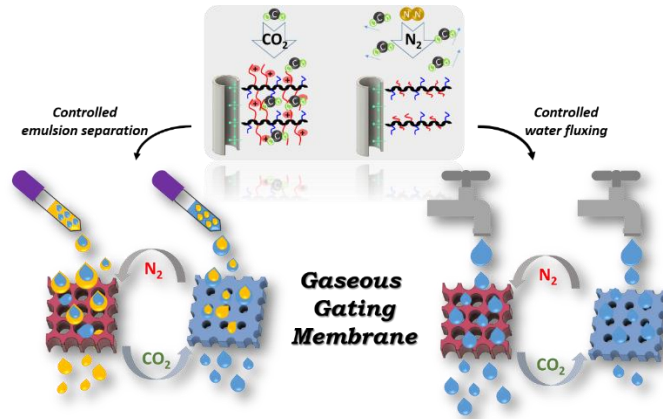


Table of content graphics of chapter 6.

6.1. Introduction

Biological cell membrane exists ubiquity in living systems which capable to segregate intracellular from extracellular environment. Additionally, it controls movement of substances in and out of cells and organelles.^[228] Inspired by biological cell membrane, artificial membrane chromatography, which is mainly based on a thin layer of well-organized porous stationary phase, has been extensively investigated for controllable matter permeance.^[229,230] The artificial membrane act as a barrier separator, filtrates are forced to pass through the membrane while undesired substances are retained. Permeability and stiffness are essential elements for membrane materials. Additionally, materials with well-uniformity, controlled pore diameter and length as well as surface chemistry are of particular important for constructing smart artificial membrane chromatography.^[231] Amongst, anodic aluminum oxide (AAO) membrane stands out from the choices attributed to its well-arranged and adjustable porous structures.^[232] Additionally, AAO pore walls rich in hydroxyl groups which are accessible for further functionalization via general modification method.^[233] As a consequence, AAO has been exclusively used as filtration membrane for molecule separation,^[234–237] water purification,^[238–240] or desalination,^[241] etc. For

instance, Song *et al.* had decorated AAO membrane with polyrhodanine via vapor deposition polymerization. The obtained polyrhodanine functionalized AAO membranes are capable utilized for the selective removal of ions i.e. Hg(II), Ag(I) and Pb(II) from contaminated water.^[242]

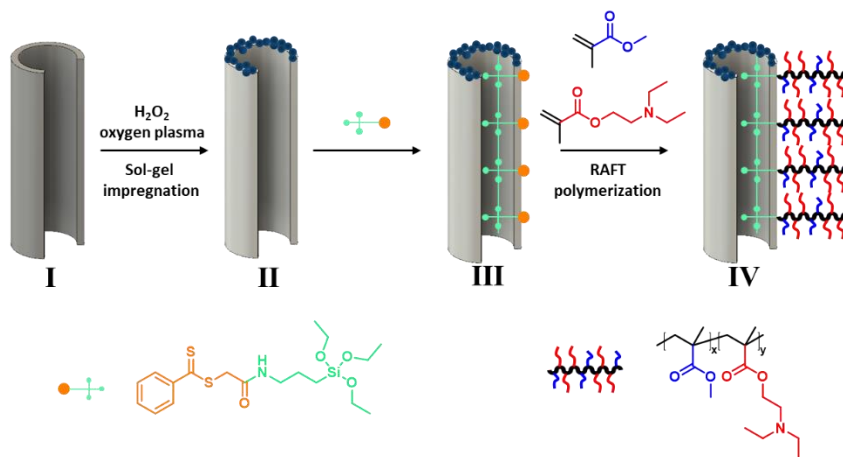
Supplementary, in order to enable artificial membrane with smart gating property, stimuli-responsive polymers are generally incorporated with fundamental membrane materials.^[243,244] Attributing to reversible transformation of chemical or physical properties of stimuli-responsive polymers, membrane permeability and selectivity are able to be adjusted upon diverse stimulations, such as temperature, pH, light, magnetic field or redox agents, etc. Indeed, stimuli-responsive polymer synergistic artificial membranes are widely applied for water purification,^[245] bioprocessing,^[246,247] energy devices,^[248] molecule sieving,^[249] etc. On this account, via surface-initiated atom transfer radical polymerization (SI-ATRP) methodology Chu *et al.* had prepared thermo-responsive gating membrane from grafting of poly(*N*-isopropylacrylamide) (PNIPAm) chains onto AAO membrane, the achieved composite membrane exhibits reversible thermo-responsive permeation property.^[250] Besides, Tufani *et al.* had immobilized pH-responsive poly(methylacrylic acid-*co*-ethylene glycol dimethacrylate) brushes on AAO, the filtration performance of attained membrane can be tuned through pH variations.^[152]

Although stimuli-responsive polymers and derivatives have been widely applied in preparation of smart gating on AAO membrane, there are still certain drawbacks that limit their applications.^[251,252] For instance, regardless of benefit brought by pH responsive polymers, addition of acids and bases are inescapable while triggering its reversibility; which causes salt accumulation in the working system.^[253,254] Therefore, in order to eliminate by-products that are generated during repeated-stimulation processes, “sustainable triggers” are crucial to be explored.^[255] Certainly, literature survey discloses the recent tendency in supplementation of smart membrane technologies, which are controlled by manipulation of surface wettability via gaseous stimulations, such as carbon dioxide (CO₂) triggering.^[134,256] Incontrovertibly, CO₂ is a nontoxic, inexpensive, benign and abundant gas, it has been emerged as the most studied gas trigger during the past decades.^[257] Specially, polymers feature amine and/or amidine groups are able to react with carbonic acid generated by CO₂ under wet conditions and yielding hydrophilic compounds; upon removal of CO₂, original state of polymer conformation, polarity and wettability are recovered. The noninvasive stimulations and has attracted great interests and explorations on constructing of CO₂ gated membranes.^[258,259] Nevertheless, fabrication of smart AAO membranes

with CO₂ gating properties is still unexplored, particularly, for specific targeted applications, such as emulsion separation. Therefore, in this chapter we are aiming to develop a “sustainable gas” (i.e. CO₂) gated AAO membrane for controlled permeation. Accordingly, by adopting surface-initiated reversible addition-fragmentation chain-transfer (SI-RAFT) polymerization strategy, poly(methyl methacrylate-*co*-2-(diethylamino)ethyl methacrylate) (poly(MMA-*co*-DEAEMA)) brushes were “grafted from” AAO membrane. The synthesized composite membrane features uniform porous structure and a thin layer of stimuli-responsive copolymer-brush. The grafted PDEAEMA chain attains the system with a gas switchable hydrophobic–hydrophilic surface. Additionally, combined with volume variation of polymer chains under gaseous stimulation, the functionalized membrane is beneficial to switchable permeation properties and capable to be applied for gaseous controlled water flux and emulsion separation.

6.2. Strategy

Scheme 6.1 illustrates fabrication procedures of poly(methyl methacrylate-*co*-2-(diethylamino)ethyl methacrylate) (poly(MMA-*co*-DEAEMA)) grafted AAO (AAO-*g*-PMD) composites. Prior main fabrication process, surface chain transfer agent and through-hole isotropic AAO membranes were prepared. Based on obtained through-hole AAO membrane, essential post-processing procedures for constructing of functional AAO were carried out. To start, as-prepared AAO membranes (I in Scheme 6.1) were pre-treated by immersing into H₂O₂ solution for 30 min and subsequently processed to oxygen plasma treatment in order to increase the amount of active hydroxyl groups on membrane surface.^[260] Subsequently, a sol-gel impregnation process was carried out. A thin layer of silica nanoparticles was deposited on membrane surface via spin coating to further improve the surface activity as well as enhance surface roughness of AAO membrane (II in Scheme 6.1). Afterwards, pre-synthesized surface chain transfer agent, 2-oxo-2-((3-(triethoxysilyl)propyl)amino)ethyl benzodithioate, was immobilized onto modified AAO through silnalization (III in Scheme 6.1). Thereafter, polymer brushes were grown on the AAO surface in anhydrous 1,4-dioxane in the presence of 2,2'-azobis(isobutyronitrile) as initiator at 70 °C for 4 h. After thoroughly rinsed with ethanol and THF, poly(MMA-*co*-DEAEMA) grafted AAO membrane (AAO-*g*-PMD) was obtained.



Scheme 6.1 Schematically illustration for the preparation of poly(methyl methacrylate-co-2-(diethylamino)ethyl methacrylate) grafted AAO membrane (AAO-g-PMD). (I) Pristine AAO membrane; (II) AAO-silica membrane (AAO-g-SiO₂); (III) chain transfer agent attached AAO membrane (AAO-g-CTA); (IV) AAO-g-PMD.

6.3. Results and Discussion

As aforementioned, pristine AAO on aluminum membrane was obtained via two-step anodization process using aqueous H₃PO₄ as electrolyte.^[181] Followed, the backside of aluminum substrate and aluminum oxide barrier layer of pristine AAO membrane were partially removed result in a through-hole isotropic AAO membrane on the supporting of circumferential connected aluminum and alumina substrate. The optical, SEM images as well as schematic illustrations of obtained AAO membrane are shown in Figure 6.1. As reported in literature, pure free standing through-hole AAO membrane only consists of alumina, which has low mechanical strength. Alumina is brittle and fragile, which brings challenges during post-modification process.^[261,262] In order to solve the problem and increase mechanical property of through-hole AAO membrane, in this work, we fixed the backside trepanning position and opened the inner circle of AAO membrane, as marked as red dotted-line in Figure 6.1. Besides, a bigger concentric circle was left that retained barrier alumina layer and aluminum substrate underneath (green dotted-line). The obtained AAO membrane is composed of through-hole channels that are responsible for fluxing and build-in supporting layer that guarantee maneuverability during post-processing. SEM images that depict the morphology of both channel and substrate structures are collected in Figure 6.1, which indicate the successful fabrication of through-hole AAO membrane.

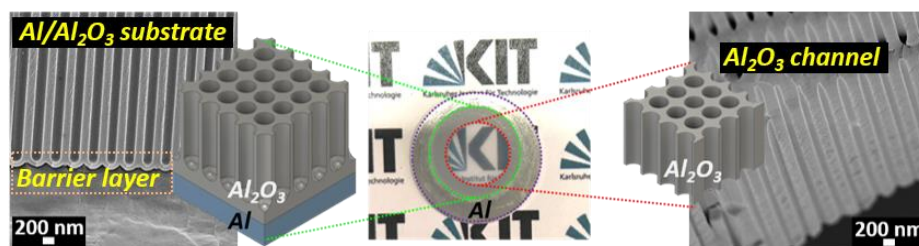


Figure 6.1. Optical image, SEM images and corresponding schematic illustrations of through-hole AAO membrane.

Further, based on obtained through-hole AAO membrane post-processing procedures were carried out according to Scheme 6.1. Surface morphologies of pristine AAO and AAO-g-PMD were characterized by SEM. In Figure 6.2 A and B, hexagonally packed pores with narrow size distribution over the whole aluminum sheets were observed on pristine AAO, the surface was found smooth and with average pore size of ≈ 261 nm. While after depositing with SiO_2 nanoparticles and grafting with poly(MMA-co-DEAEMA) brushes, the membrane pore size decreased to ≈ 213 nm. Additionally, as shown in Figure 6.2 C and D, the surface roughness was found to be increased and the silica nanoparticles were homogeneously distributed on membrane surface.

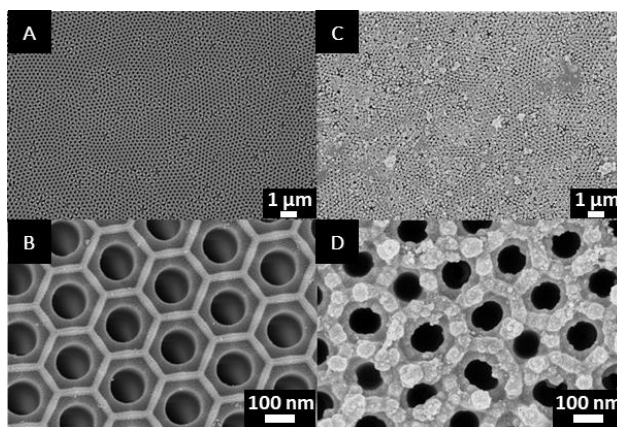


Figure 6.2. Comparative SEM images of (A, B) pristine AAO, (C, D) AAO-g-PMD.

Followed, FT-IR measurement were conducted in order to monitor surface component variation of AAO membrane during sequential modification process. The FT-IR spectra of pristine AAO (a), SiO_2 deposited AAO (b), AAO-g-CTA (c), and AAO-g-PMD (d) are shown in Figure 6.3. By comparing with spectrum of pristine AAO, new band arose at 1090 cm^{-1} after depositing of SiO_2 nanoparticles, which was ascribed to the Si-O-Si asymmetric stretching vibration of silica.^[263] Subsequently, upon anchoring of surface CTA onto the SiO_2 nanoparticles deposited AAO

membrane, bands that assigned to symmetric C-N stretching vibration, N-H deformation and C=O stretching, were observed at 1445 cm^{-1} , 1533 cm^{-1} and 1647 cm^{-1} , respectively. Accordingly, the successful immobilization of surface CTA was confirmed.^[158] Accordingly, FT-IR analysis facilitated to certify SI-RAFT polymerization. A peak attributed to carbonyl vibration of PDEAEMA was observed at 1730 cm^{-1} .^[264] Besides, a strong absorption band was detected in the range of 2821 cm^{-1} to 3005 cm^{-1} , that was referred to stretching vibrations of $-\text{CH}_2$ and $-\text{CH}_3$ groups from the polymer backbone.^[265]

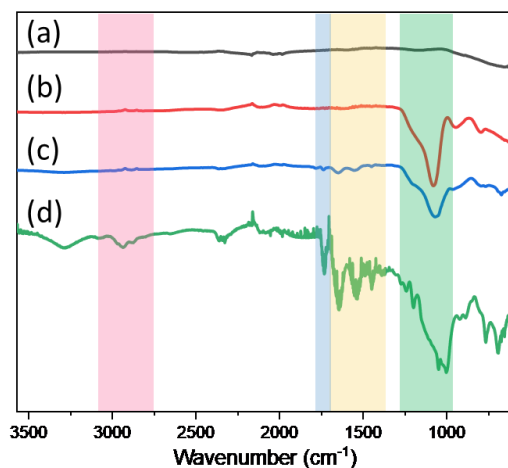


Figure 6.3. FT-IR spectra of (a) pristine AAO membrane, (b) AAO-g-SiO₂, (c) AAO-g-CTA and (d) AAO-g-PMD.

Supplementary, static water contact angle (WCA) measurements could also guarantee the successful AAO functionalization. Therefore, changes in the wettability of membrane at each modification step were tracked, and the obtained optical images were illustrated in Figure 6.4. The pristine AAO membrane was converted from hydrophilic (WCA: $\approx 30^\circ\text{C}$) to hydrophobic (WCA: $\approx 100^\circ\text{C}$) after deposition with SiO₂ nanoparticles. Subsequently, hydrophobicity of AAO membrane was further increased (WCA: $\approx 130^\circ\text{C}$) when surface CTA was immobilized. Upon SI-RAFT polymerization, grafted polymer chains induced additional enhanced surface hydrophobicity of AAO (WCA: $\approx 141^\circ\text{C}$), which was revealed by the enhanced surface roughness after polymerization.

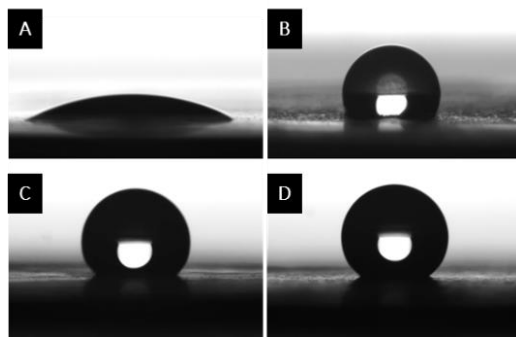


Figure 6.4. Water droplet on different surfaces: (A) Pristine AAO, (B) SiO₂ nanoparticle deposited AAO, (C) AAO-g-CTA and (D) AAO-g-PMD.

Furthermore, the reversible wettability variations of AAO-g-PMD membrane upon CO₂ stimulations were also recorded by static WCA measurements. As illustrated in Figure 6.5 A, upon exposure to a CO₂-purged aqueous solution for 5 min, the water contact angle of AAO-g-PMD membrane shows a drastic decrease from 140.38±0.88° to 12.80±3.77°, indicative of polymer brush hydration.^[266,267] Whereas, after purging with N₂ gas for 10 min, the initial contact angle of AAO-g-PMD membrane was recovered, which suggests the deprotonation of PDEAEMA results in loss of water from polymer brushes and form collapsed polymer brushes. The experiments were repeated for ten times (Figure 6.5 B), showing excellent reversibility of membrane wettability upon alternate bubbling with CO₂ and N₂ gases.

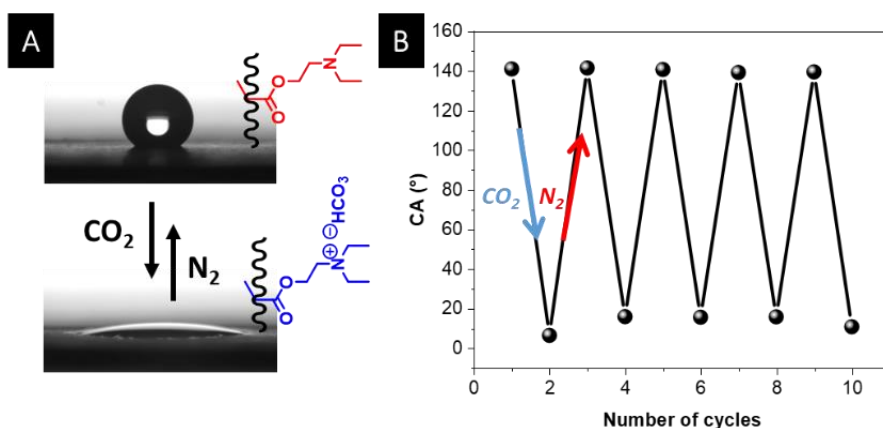


Figure 6.5. (A) Optical images, chain transformation illustrations and (B) reversible contact angle (CA) of AAO-g-PMD triggered by CO₂ and N₂.

The responsive mechanism is typically a variation of pH control and is the result of reaction between carbonic acid generated by CO₂ and tertiary amine groups. In the initial state, AAO-g-

PMD membrane surface is hydrophobic. By exposure CO₂, the tertiary amine groups in PDEAEMA react with CO₂ derived carbonic acid in an aqueous medium, forming charged ammonium bicarbonate salts.^[268,269] Thus promoting hydration of PDEAEMA brushes in water and adopting a chain-extended state. Thereafter, entrapped CO₂ are able to be expelled by purging with N₂, that inducing recover of PDEAEMA brushes back to original collapsed state. As mentioned above, this CO₂ switchable wettability variation are able to be repeated many times without the addition of any chemicals that could remain in the solution. Certainly, the advantage of gas responsive membranes compared to a conventional pH-responsive membrane is that it functions without using strong chemicals (such as acid and base) to change pH and generally requiring repeated addition of these chemicals into the solution, producing chemical wastes such as excessive salts.

In addition, it has been reported that the molecular weight of surface initiated polymers is equal to that of free polymers synthesized in bulk.^[270] Therefore, the grafted polymers are often characterized by polymerizing the same monomers under bulk condition utilizing free CTA. In order to further investigate the influence of polymer molecular weight on membrane permeability, a series RAFT and SI-RAFT polymerizations of MMA and DEAEMA were processed. Upon synthesis, different amount of free CTA, *S*-(thiobenzoyl)thioglycolic acid, were added into each reaction system to control the polymerization degree of poly(MMA-*co*-PDEAEMA)s in bulk and on AAO surface. As a reference, the free copolymer chains were used to estimate the molecular weight and molecular weight distribution of surface grafted polymer chains. Detailed feed ratios and characterization data are illustrated in Table 6.1. As expected, lower feed ratio between CTA and reactive monomer resulted in a higher molecular weight of obtained polymers.

Table 6.1. Experimental conditions and properties of Poly(MMA-*co*-DEAEMA)s.

Code	MMA	DEAEMA	CTA	AIBN	$M_{n, theo}$	$M_{n, H NMR}^a$	$M_{n, GPC}^b$	M_w/M_n^b
	(Ratio between the reagents)				(g mol ⁻¹)	(g mol ⁻¹)	(g mol ⁻¹)	
AAO-g-PMD-1	200	300	10	1	7762	2320	20300	1.94
AAO-g-PMD-2	400	600	10	1	15312	6480	33300	2.04
AAO-g-PMD-3	2000	3000	10	1	75712	17820	85000	2.27

^a Calculated by ¹H NMR in CDCl₃ and ^b Obtained from GPC in DMAc

Grafting of polymers differ in molecular weights on porous AAO membranes lead to the variation of membrane permeability. The membrane permeability of diverse polymer grafted AAO was recorded by water flux measurements. As illustrated in Figure 6.6, it can be seen that higher molecular weight of the grafted polymer chains resulted in a relatively lower water flux. For instance, the molecular weight of polymer chains from AAO-g-PMD-1 membrane is 2320 g mol^{-1} and AAO-g-PMD-1 exhibited average water flux of $510 \text{ L/m}^2\text{h}$; however, when the molecular weight of grafted polymer increases to 17820 g mol^{-1} (AAO-g-PMD-3), the average water flux decreases to $462 \text{ L/m}^2\text{h}$.

Besides, it has been mentioned above that grafted PDEAEMA chains could undergo transition of polymer conformation between collapsing and stretching state.^[269] Volumetric variations of polymer layer is capable to control the membrane pore sizes thus adjust water permeance of AAO-g-PMD membrane. Figure 6.6 shows the change of water flux through AAO-g-PMD-(1, 2, 3, from Table 6.1) membrane rely on gaseous stimulation. In neutral media, AAO-g-PMD membrane exhibit water flux of $461\sim 510 \text{ L/m}^2\text{h}$. Upon purging with CO_2 , water flux decreases sharply to $187\sim 69 \text{ L/m}^2\text{h}$. However, when further triggering with N_2 to expel CO_2 , the recovering of permeability for all AAO-g-PMD membranes were observed. As expected, permeability of AAO-g-PMD membrane also showed good CO_2 -reversibility when alternatively triggering with CO_2 and N_2 . Furthermore, it is worthy pointing out that the molecular weight of the grafted polymer chains also effected the stimuli-triggered variations of the membrane permeability. As shown in Figure 6.6, AAO-g-PMD-3 that grafted with higher molecular weight polymer result in a broader variation of water flux ($392 \text{ L/m}^2\text{h}$) upon stimulation; on the contrary, AAO-g-PMD-1 with shorter polymer chains exhibit narrower water flux variation of $323 \text{ L/m}^2\text{h}$.

The AAO-g-PMD membranes are able to conduct gaseous controlled reversible change in membrane pore size and wettability which are demonstrated to be useful for selective separations.^[155] Therefore, AAO-g-PMD membranes were tested for oil/water emulsion separation. Under neutral condition, AAO-g-PMD membranes were hydrophobic ($\text{WCA} \approx 141^\circ$), when filtrate with water-in-oil emulsion, continuous oil phase with higher affinity to hydrophobic surface was preferred to spread over the membrane while water droplets were repelled from attaching. As a consequence, oil phase was selectively filtered through the AAO-g-PMD membrane and water droplets were rejected from filtration. Correspondingly, upon bubbling with CO_2 , protonating of PDEAEMA brushes occurred result in a hydrophilic AAO-g-PMD membrane. Therefore, AAO-

g-PMD membrane was able to separate water from water-in-oil emulsion. During filtration, a continuous water phase was preferentially invaded hydrophilic membrane and penetrate through the membrane while oil droplets were retained. Whereupon, AAO-*g*-PMD membrane could be used for selective separation of oil-in-water and water-in-oil emulsion under CO₂ regulation. The filtration setup is depicted in Figure 8.11 and all the percolations were carried out under a pressure of 0.11 MPa, the eluate were collected for further characterizations. Exemplary for AAO-*g*-PMD-1, the results for toluene/water emulsion separation are illustrated in Figure 6.7 and Figure 6.8, respectively.

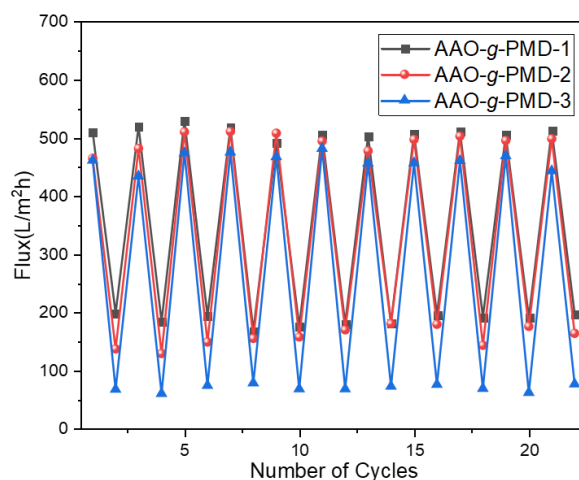


Figure 6.6. Reversible behavior of water flux of AAO-*g*-PMD 1, 2 and 3 (Table 6.1), respectively, upon triggering with CO₂ (Bottom) and N₂ (Top).

Correspondingly, from the optical image (Figure 6.7 A), it can be seen that prior filtration, water-in-toluene emulsion revealed a milky but homogenous state with dispersed water droplet in oil continuous phase; while after passing through AAO-*g*-PMD membrane, the eluate exhibits translucent appearance. Which in accordance with the revealed optical microscope images of emulsion before and after filtration. Accordingly, the sizes of water-in-oil emulsion droplet before and after filtration were analyzed by dynamic light scattering (DLS) measurement. From the DLS spectra in Figure 6.7 B, the droplet size distribution of water-in-toluene emulsion ranging from 2 μm to 4 μm with a maximum of 3 μm. While after filtration, the droplet size decreased to tens of nanometers. Further, the continuous emulsion separation of water-in-toluene emulsion is conducted, in order to verify the stability and recover capacity of as-prepared membrane. The results were depicted in Figure 6.7 C, as shown, the initial flux of emulsion is 300 L/m² h while

over time the flux decreased owing to the accumulated water droplet which partially block the membrane channels for fluxing. After rinsing with ethanol, the permeability is recovered to 82 %, and kept decline upon further filtration of emulsion. However, when washed membrane again with ethanol, the emulsion flux ability is capable to be recovered. Nevertheless, the results mentioned above indicate reversibility of membrane for water-in-oil separation under neutral working condition.

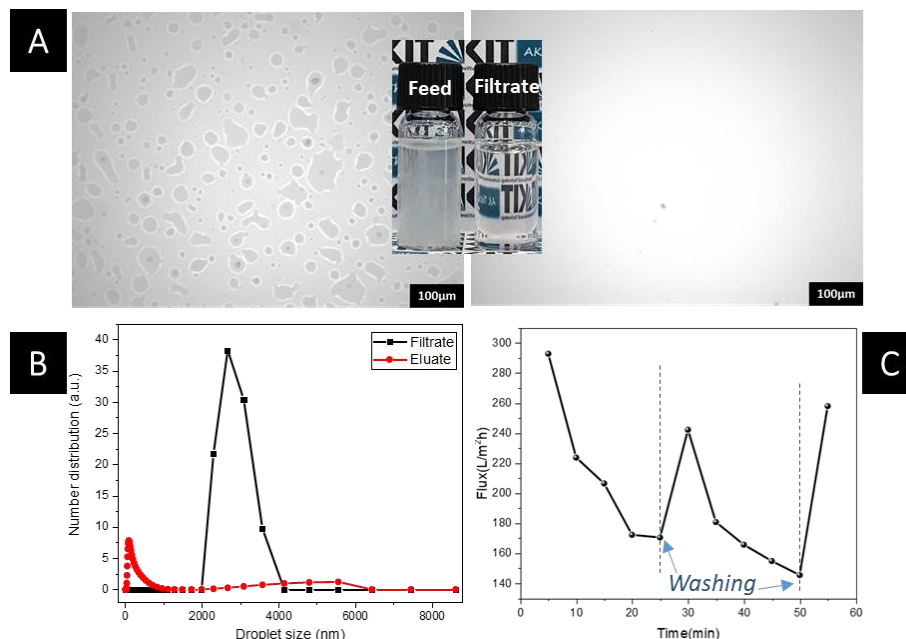


Figure 6.7. Water-in-oil emulsion separation of AAO-g-PMD-1. (A) Optical images and (B) droplet size distribution from DLS of water-in-toluene emulsion before and after filtration, (C) permeation of water-in-toluene emulsion.

On the contrary, AAO-g-PMD membranes were able to separate water phase from toluene-in-water emulsion upon triggering with CO₂. The results are showed in Figure 6.8. Similarly, from the recorded optical image, milky emulsion turned into clear eluate after passed through the CO₂ triggered membrane. From DLS measurement, the particle size of origin toluene-in-water emulsion was observed ranging from 3 μm to 6 μm, while after filtration, the residual emulsion particles with size of few to tens nanometers were observed which can be ascribed to the existed of surfactant in solution.^[271] In addition, the permeability and separation reversibility of CO₂ triggered membrane were investigated via continuous filtration over toluene-in-water emulsion. The initial fluent is 100 L/m² h, which apparently lower than the flux of water-in-toluene emulsion. Indeed,

upon purging with CO₂, protonating of grafted polymer chains lead to configuration transition from a collapsed state to an extended state which induce the increase of grafted polymer volume hence reduce membrane permeability. As expected, over filtration time, the permeability of the as-prepared membrane declined due to the blocking of oil droplet on the membrane pores. Nevertheless, further washing and CO₂ stimulation treatment resulted in 90 % recovery of the membrane permeability.

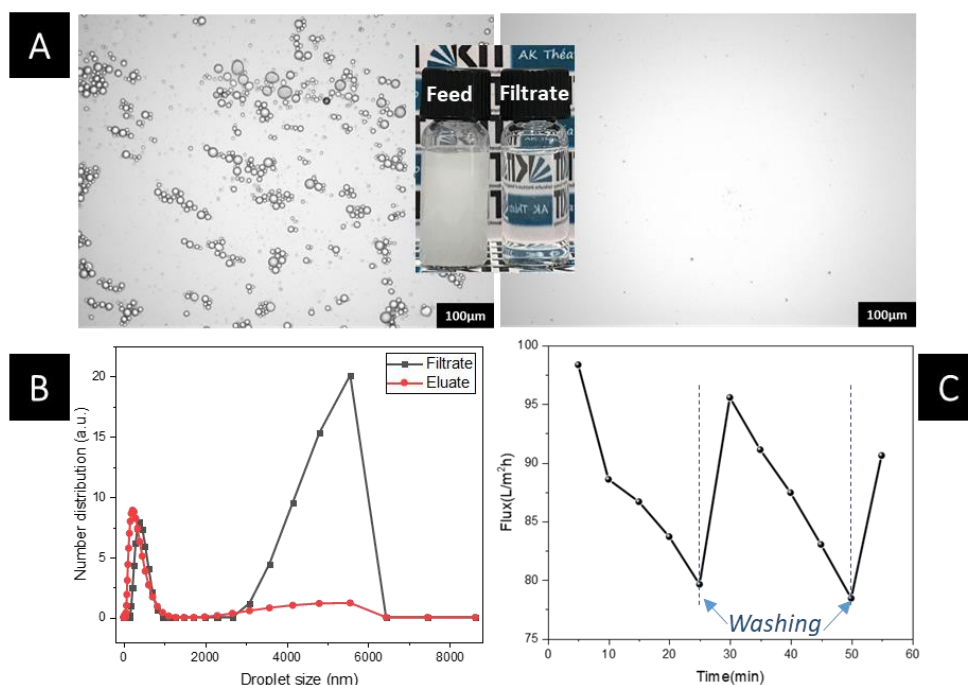


Figure 6.8. Oil-in-water separation of AAO-g-PMD-1. (A) Optical images and (B) droplet size distribution from DLS of toluene-in-water emulsion before and after filtration, (C) permeation of toluene-in-water emulsion.

6.4. Conclusion

In conclusion, poly(methyl methacrylate-*co*-2-(diethylamino)ethyl methacrylate) brushes have been grafted from through-hole AAO membrane via SI-RAFT. The obtained AAO/polymer composites were demonstrated to feature CO₂ stimuli-responsive property whose wettability and permeability were adjustable by gas aeration. In addition, the molecular weight of grafted polymer chains could be adjusted by varying the feed ratio between chain transfer agent and reactive

monomers during RAFT polymerization. A higher molecular weight of grafting polymer chains resulted in a broader flux variation upon stimulations.

Ultimately, the functionalized AAO membrane were demonstrated capable to be used for oil/water emulsion separation. Consequently, the work presented here provides a facile method for fabricating gas induced stimuli-responsive membranes. Indeed, these membranes may offer many possibilities to develop new smart materials that, for instance, could be applied to industrial sewage treatment, due to their continuous processing ability.

7. Concluding Remarks and Outlook

Within this thesis, anodic aluminum oxide templates having well-ordered-pore structures were fabricated. Each procedure during the fabrication process was investigated in detail in order to clarify the correlation between working conditions and corresponding template structures. Additionally, post-treatments were also intensively studied, such as pore widening and backside pore opening. By manipulating working conditions as well as post-treatments, various AAO templates that differ in pore length, pore diameter, inter-pore distance and pore structures were prepared and well-characterized. Additionally, three different AAO-template assisted fabrication techniques were successfully carried out for the realization of diverse objectives, as follows:

AAO template-assisted nanopatterning was first carried out in order to prepare a series of polymeric Janus nanorods. Conducting sequential free radical polymerization under AAO confinement, oxygen plasma treatment, and post-crosslinking process, PS-*b*-PNIPAm, PNIPAm-*b*-PPFPA and PPYNP-*b*-PMMA Janus nanorods were obtained. The formed Janus nanorods consist of two polymeric blocks with distinguishable shape and/or composition. In/between each block of formed Janus nanorods, photoinitiated crosslinker 4-acryloylbenzophenone was added and via a post UV treatment, the two blocks of Janus nanorods were chemically bonded to prevent nanorod separation. The method mentioned here overcame limitation of low producing yields and complex preparation process. Additionally, the fabrication method is generally applicable for preparing various polymeric Janus nanorods with different chemical components. Polymeric materials are more preferable to be modulated and functionalized and consequently may show potential application in surfactant, bio-related and optical devices.

Furthermore, AAO template assisted patterning was also utilized for the preparation of smart two-dimensional films. Accordingly, free standing PPFPA pillar arrays were polymerized from AAO template on a polyester substrate. As reported, amino groups are able to react with the PFP ester groups under mild conditions, enabling the PPFPA pillar array film to be post functionalized. For instance, poly(methacrylic acid) polymers bearing amino end groups were synthesized and then attached onto PPFPA pillar arrays via post-polymerization modification. The formed hierarchical films bearing PPFPA micro pillar arrays that were grafted with PMAA nanobrushes were found to maintain underwater superoleophobicity and showed reversible oil adhesion upon pH stimulation. The obtained hierarchical film showed potential application for underwater oil manipulation.

Additionally, the preparation strategy paves the way towards facile fabrication of smart films with versatile functionalities.

Beside the above mentioned sacrificial method for the preparation of nanomaterials, AAO templates are also able to be used as non-sacrificial membranes for constructing nanocomposites. On the basis of the nanocylindrical pores of an AAO membrane, CO₂ stimuli-responsive polymers were grafted from an AAO membrane via SI-RAFT polymerization. The grafted polymer molecular weight was controlled during synthesis by adjusting the feed ratio between reactive monomer and free chain transfer agent. As a consequence, the pore diameters and permeability of smart membrane could be customized via controlled polymer synthesis. In addition, attributing to the stimuli-responsive properties of the grafted polymer chains, variation of membrane pore diameter and membrane wettability were accessible. Upon CO₂ stimulation, fabricated membranes were able to utilize a controlled water flux as well as a controlled emulsion separation. Compared with conventional pH stimulation, CO₂ stimulations provides superior reversibility and avoids accumulation of contaminations in the working systems. Additionally, the obtained smart membrane is able to be applied in the field of sewage purification.

To sum up, in the present thesis I have provided versatile possibilities of preparing nanomaterials, from one dimensional Janus nanorods, to two dimensional nanostructured surfaces, to three dimensional smart membranes, using AAO template assisted approaches. The strategies presented above are all able to be widely useful for customized materials application.

8. Materials and Methods

8.1. Materials

Methacrylic acid (MAA, 99 %, Sigma-Aldrich), 1,6-hexanediol diacrylate (HDODA, 80 %, Sigma-Aldrich), 2-(*N,N*-diethylamino)ethyl methacrylate (DEAEMA, 99 %, Sigma-Aldrich) and methyl methacrylate (MMA, 99 %, Sigma-Aldrich) were purified by passing through a neutral aluminum oxide column. 2,2'-azobis(isobutyronitrile) (AIBN, 98 %, Sigma-Aldrich) was recrystallized from methanol. *N*-Isopropylacrylamide (NIPAm, >98 %, TCI) was purified by hot filtration and recrystallization from hexane.

Aluminum discs (99.999 %, Good Fellow), silicon dioxide (SiO₂, 10~20 nm, Sigma-Aldrich) 2,6-lutidine (≥99 %, Sigma-Aldrich), (3-aminopropyl)triethoxysilane (98 %, ABCR), 3-(trimethoxysilyl)propyl methacrylate (98 %, ABCR), tetraethyl orthosilicate (TEOS, 98 %, Sigma-Aldrich), 4-hydroxybenzophenone (98 %, Sigma-Aldrich), acryloyl chloride (≥97 %, Sigma-Aldrich), pentafluorophenyl (≥99 %, Sigma-Aldrich), *N,N,N',N'',N'''*-pentamethyldiethylenetriamine (PMDETA, 99 %, Sigma-Aldrich), copper(I) bromide (CuBr, 99.999 %, Sigma-Aldrich), copper(II) chloride (CuCl₂, 97 %, Sigma-Aldrich), sodium acetate (NaOAc, ≥99 %, Sigma-Aldrich), iron(III) chloride (FeCl₃, 97 %, Sigma-Aldrich), pyrrole (ppy, 98 %, Sigma-Aldrich), chromium(IV) oxide (CrO₃, ≥98 %, Sigma-Aldrich), 2-hydroxy-4'-(2-hydroxyethoxy)-2-methylpropiophenone (Irgacure 2959, 98 %, Sigma-Aldrich), *N,N'*-methylenebis(acrylamide) (MBAA, 99 %, Sigma-Aldrich), *N*-Boc-ethanolamine (98 %, Sigma-Aldrich), triethylamine (TEA, 99.5 %, Sigma-Aldrich), 2-bromoisobutyryl bromide (98%, Sigma-Aldrich), trifluoroacetic acid (TFA, 99 %, Sigma-Aldrich), sodium dodecyl sulfate (SDS, ≥99 %, Fischer), anhydrous sodium sulfate (Na₂SO₄, ≥ 99 %, Roth), *S*-(thiobenzoyl)thioglycolic acid (99 %, Sigma-Aldrich), *N*-hydroxysuccinimide (NHS, ≥ 97 %, Sigma-Aldrich) *N*-ethyl-*N'*-(3-dimethylaminopropyl)carbodiimide hydrochloride (EDC, 99 %, Sigma-Aldrich) were used without further purification.

Anhydrous dichloromethane (Anhyd. DCM, ≥ 99.8 %, Aldrich), anhydrous ethanol (99.8 %, Acros), anhydrous 1,4-dioxane (99.8 %, Acros), anhydrous toluene (99.8 %, Acros), tetrahydrofuran (THF, 99.9 %, VWR), *N,N*-dimethylformamide (DMF, 99.9 %, VWR), ethanol (96 %, VWR) methanol (99.99 %, VWR), hexane (99.99 %, VWR), chloroform (≥ 99.8 %, VWR), acetone (≥ 99.5 %, Fischer), diethyl ether (≥ 99.5 %, Roth), ethyl acetate (≥ 99.5 %, Roth), dimethyl

sulfoxide (DMSO, $\geq 99.5\%$, Roth), toluene ($\geq 99.5\%$, Roth), ortho-phosphoric acid (H_3PO_4 , 85 %, Roth), perchloric acid (HClO_4 , 70 %, Roth), hydrogen peroxide (H_2O_2 , 35 %, Roth), oxalic acid dihydrate ($\geq 99.5\%$, Roth), sodium hydroxide (NaOH, 98 %, Roth), 1, 2-dichloroethane (DCE, $\geq 99.5\%$, Roth), buffer solution (pH 5 ± 0.02 , Roth), chloroform- d_1 (CDCl_3 , 99.8 % D, Eurisotop), dimethyl sulfoxide- d_6 (DMSO- d_6 , 99.8 % D, Eurisotop), dichloromethane- d_2 (CD_2Cl_2 , 99.5 % D, Sigma-Aldrich) were used as received.

8.2. Characterization Methods and Instrumentations

8.2.1. Scanning Electron Microscopy

8.2.1.1. Theoretical Background

Scanning electron microscopy (SEM) is one type of most used electron microscopes for investigating sample surface topography and composition. Figure 8.1 schematically illustrates construction of a typical SEM device. Generally, for a typical SEM measurement, an electron beam is thermionically emitted from an electron gun and accelerated by an applied voltage up to 30 kV. The electron beam is then focused by a combination of lenses to a spot about 0.4 nm to 5 nm in diameter. After passing through a scanning coil, the electron beam is injected to the surface of the specimen. As the result of electron-sample interaction, secondary electrons (low energy), backscattered electrons (high energy) and characteristic X-rays are produced. Those signals can be collected via various detectors. The backscattered detector collects backscattered electrons generated from electrons reflected off the surface and deeper from within the specimen and providing images which convey information on the sample's composition as well as topography, crystallography and magnetic field of specimen. The secondary electron detector collects the secondary electrons which are created from the interaction of the primary beam with the sample and further integrate into surface topographical images on screen. X-ray detectors collect X-rays that are generated by the absorbed electrons. The element composition of the specimen can then be obtained due to element specific emission of X-rays.^[272]

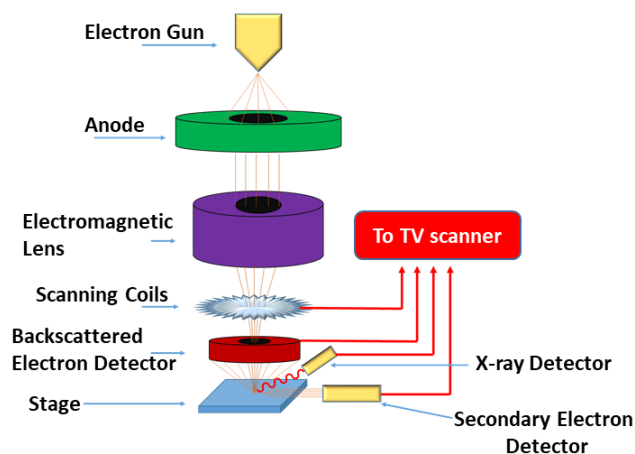


Figure 8.1. Schematic of a scanning electron microscope.

8.2.1.2. Instrumental Information

The SEM images are recorded using a Zeiss LEO 1530 field emission scanning electron microscope with accelerating voltage of 5 kV. Prior to SEM measurement, samples are coated with a thin layer of gold or platinum nanoparticles with a thickness of 5 nm to avoid charging effects.

8.2.2. Transmittance Electron Microscopy

8.2.2.1. Theoretical Background

Transmittance electron microscopy (TEM) is a microscopy technique and the operating principle is the transmission of an electron beam through a thin specimen to shape into an image. Similar to SEM, as revealed in Figure 8.2, a beam of electrons is produced from an electron source and then be accelerated towards the sample. Further, the electron beam is tightly focused by a condenser lens and aperture before it hits the specimen. The interaction between specimen and electrons results in different signals such as X-rays, transmitted beam, diffracted beam and in elastically scattered electrons. Depending on the position of the objective aperture, bright field (BF) and dark field (DF) images can be obtained. It is worth noting that the transmission of electrons is highly dependent on the materials properties like density, composition, etc. As an example, porous

materials allow more electrons to pass through than a dense material, which can be used to examine materials with non-uniform density.

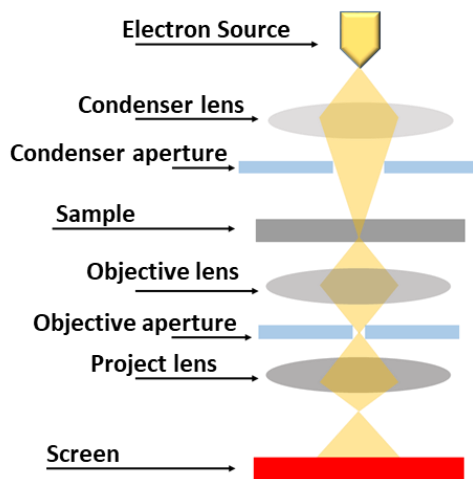


Figure 8.2. Schematic of a transmittance electron microscope.

8.2.2.2. Instrumental Information

TEM images were recorded by using a Hitachi H600 electron microscope instrument which operated with an accelerating voltage of 100 kV. The samples were prepared by dispersion in DI water and dropwise casting to a carbon film covered copper grid followed by drying at ambient condition.

8.2.3. Oxygen Plasma Cleaner

8.2.3.1. Theoretical Background

Plasma is a partially ionized gas which is one of four fundamental states of matter different from solid, liquid and gas. It consists of electrons, atomic ions, molecule ions, neutral atoms and molecules which presents in excited and ground states.^[273] Plasma can appear in nature and also can be artificially produced by applying an electric and/or magnetic field through a gas. Till now, plasma treatment has been used in processes such as deposition, etching, implantation, photoresist stripping, cleaning, and surface conditioning.

Oxygen plasma is carried out by utilizing oxygen as gas source on a plasma system. The generated oxygen plasma may cause the oxidation of polymer materials thus lead to polymer etching. Nowadays, removal of organic polymers using oxygen plasma has been extensively applied in various fields. Due to the reaction of oxygen with the carbon in the polymer specimen, the C-F and C-H bond will break and form volatile byproducts such as H₂O and CO_x from hydrocarbon polymers and COF_x, CO_x and F_x from fluorocarbon polymers, thus achieving the polymer removal. Noteworthy, polymer etching rate increased linearly with the treatment time, hence oxygen plasma was applied in this experiment for controllable micro-designed polymer etching.

8.2.3.2. Instrumental Information

The oxygen plasma treatment was carried out by low pressure plasma system type-ZEPTO from DIENER, the chamber pressure was constantly at 0.3~0.4 mbar, operating time was varied according different processing.

8.2.4. Fourier-transformation Infrared Spectroscopy

8.2.4.1. Theoretical Background

Infrared (IR) spectroscopy is a technique based on the absorption of infrared light to investigate the molecular vibrations which enabled identification of unknown compounds.^[274] Fourier-transformation infrared (FT-IR) spectrometers are the third generation of IR spectrometer. An interferogram Fourier-transform is required for the converting of raw data, hence FT-IR was named. Source, interferometer, sample compartment, detector, amplifier, analog-to-digital convertor and computer are the main components of a FT-IR spectrometer. The signals are amplified by the amplifier and converted into a digital signal through an analog-to-digital converter. Attenuated total reflectance (ATR) is an FT-IR technique which enables samples to be measured directly in the solid or liquid state avoiding comprehensive sample preparations and has been extensively used in this work. Figure 8.3 illustrates FT-IR measurement via ATR. A beam of infrared light is generated and passed through ATR crystal. Once in contact with specimen, reflections occurred at least once off the internal sample surface. In addition, reflections induced the formation of evanescent waves which penetrated and expanded into specimen. Generally, the

penetration reached between 0.5~2 μm of specimen. Afterwards, the beam is collected by a detector and further be converted characterize samples.^[275]

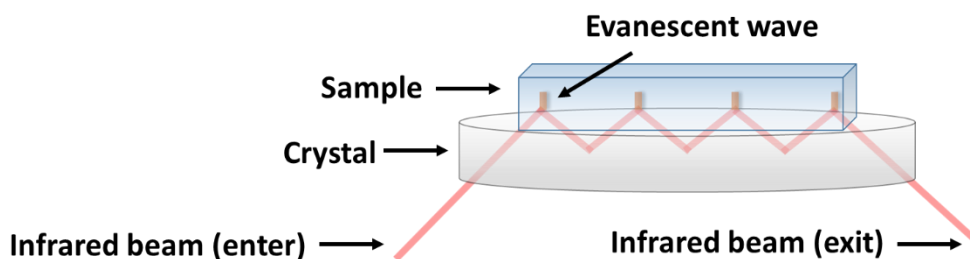


Figure 8.3. Schematic illustration of ATR FT-IR spectroscopy measurement.

8.2.4.2. Instrumental Information

ATR-FT-IR spectra was recorded from Bruker VERTEX 80V FT-IR spectrometer with a range of 600 to 4000 cm^{-1} at ambient temperature.

8.2.5. Nuclear Magnetic Resonance Spectroscopy

8.2.5.1. Theoretical Background

Nuclear magnetic resonance (NMR) spectroscopy is a technique in analytical chemistry which is utilized in research and quality control for the determination of specimen content, purity and molecular structure. It is based on the investigation of interaction of radiofrequency electromagnetic radiations with the nuclei of specimen molecules from a strong magnetic field. In a standard NMR test, the sample to be tested is placed in a magnetic field, followed by excitation with radio-frequency pulse to cause resonance between the atomic nucleus of the sample and the magnetic field, nuclei flipping into the higher-energy alignment. A time-domain radio frequency signal called the free induction decay (FID) signal is emitted as nuclei return to their original state. By Fourier-transformation, the FID signal convert to a frequency-domain signal, a NMR spectroscopy can be obtained. Attributing to the intramolecular magnetic field, resonance frequencies of molecule atoms are varied and thus representing a molecule's individual functional groups and their electronic structures.

8.2.5.2. Instrumental Information

^1H NMR and ^{19}F NMR spectroscopy were carried out using Bruker Ascend 400 spectrometer (^1H NMR 400 MHz, ^{19}F NMR 376 MHz) at 298 K. all chemical shifts are reported in ppm (δ) and calibrated on characteristic solvent signals as internal standards. All data were reported as follows: chemical shift, multiplicity (s=singlet, d=double, t=triplet, q=quartet, m=multiplet).

8.2.6. Gel Permeation Chromatography

8.2.6.1. Theoretical Background

Gel permeation chromatography (GPC) is one type of size exclusion chromatography which is often used for analysis of polymers. It is based on the separation of polymers via their size, i.e. hydrodynamic volume, by using column that packed with porous beads. During a typical GPC measurement, molecules pass through the column via elute flushing. Smaller analytes will enter into most of the pores before traversing further, which therefore requires more time for elution. On the contrary, larger sized analytes will be eluted directly out of the column and hence shorten the elution time. By comparison between the analytes' retention time and a calibration curve of polymer standards, the molecular weight as well as the dispersity can be obtained.

8.2.6.2. Instrumental Information

Size exclusion chromatography measurements were recorded using Polymer Laboratories (Varian) PL-GPC 50 Plus Integrated System equipped with two PLgel 5 m Mixed-Columns (300×7.5 mm). All measurements were carried out in DMAc under $50\text{ }^\circ\text{C}$ with a flow rate of 1 mL/min.

8.2.7. Contact Angle

The static water and oil contact angle were measured using a drop shape analyzer model DSA25S. The oil sliding angle was obtained by measuring the contact angle with a tilting speed of $1\text{ }^\circ\text{s}^{-1}$, owing to the limitation of sample water tank the maximum tilting angle of model test is 45° . 1, 2-dichloroethane was used as oil.

8.2.8. Dynamic Light Scattering

Dynamic light scattering (DLS) measurements of emulsions were recorded from Malvern Zetasizer Nano-ZS apparatus equipped with a He-Ne laser operated at 632 nm at 25 °C.

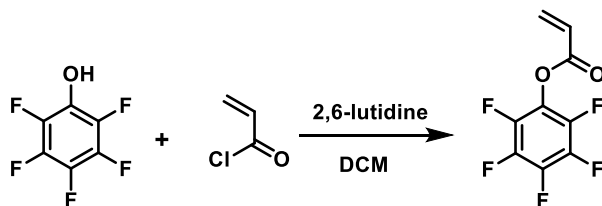
8.2.9. Optical Microscopy

The optical images of emulsions and eluates were recorded from Keyence bioevo microscope.

8.3. Experimental Procedures

8.3.1. Synthetic Protocols

8.3.1.1. Synthesis of Pentafluorophenyl Acrylate



Scheme 8.1. Synthetic route of pentafluorophenyl acrylate (PFPA).

Pentafluorophenyl (82.15 g, 0.445 mol) and 2,6-lutidine (57.38 g, 0.536 mol) were dissolved in 600 mL DCM in a three-necked round bottom flask under stirring in an ice bath. After the mixture became homogenous, acryloyl chloride (48.47 g, 0.536 mol) was added dropwise into the solution mixture and was kept in an ice bath under stirring for 3 h. The reaction was continued at room temperature for 20 h. Subsequently, the mixture was filtered to remove the precipitate and excess DCM was removed under pressure. The organic fraction was then washed with water and brine for three times and then dried with anhydrous sodium sulfate. The crude product was obtained by removing the organic solvent under pressure. The product was purified by column chromatography using DCM/hexane (9:1, v/v) to yield a colorless liquid of pentafluorophenyl acrylate (PFPA) (87 g, yield 82 %). ¹H NMR (400 MHz, CDCl₃): δ(ppm) 6.71 (dd, 1H, CH₂CH-), 6.36 (dd, 1H, CH₂CH-), 6.17 (dd, 1H, CH₂CH-); ¹⁹F NMR (376 MHz, CDCl₃): δ(ppm) -153.16 (d, 2F, -CF- from aryl), -158.51 (t, 1F, -CF- from aryl), -163.00 (d, 2F, -CF- from aryl).

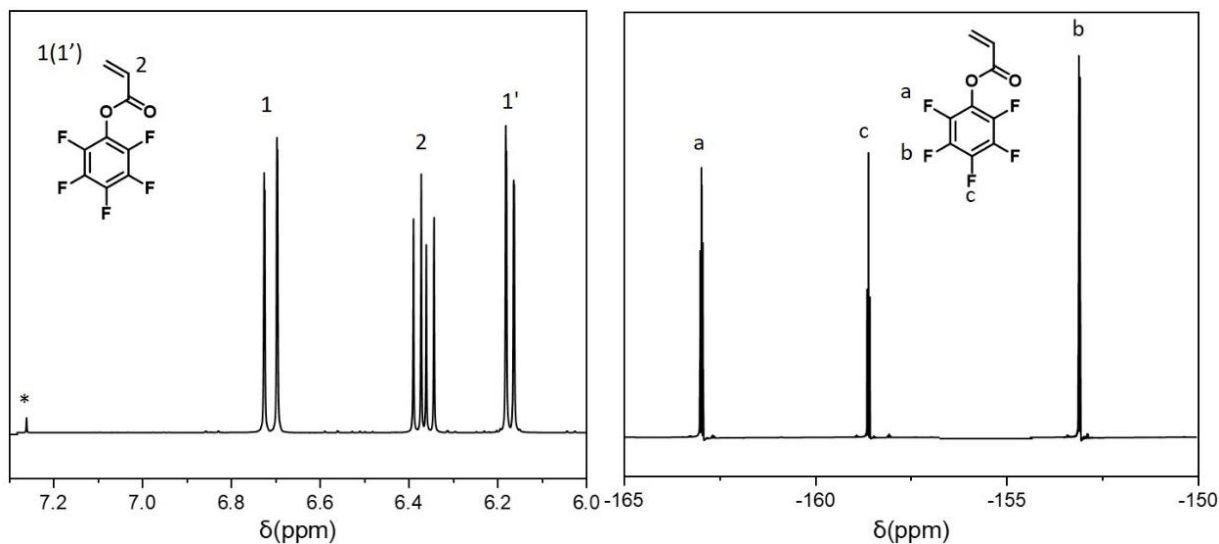
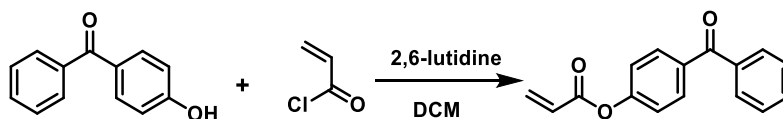


Figure 8.4. ^1H NMR (400 MHz, CDCl_3) and ^{19}F NMR (376 MHz, CDCl_3) spectra of PFPA at ambient temperature. The * indicates the residual signal of the solvent CHCl_3 .

8.3.1.2. Synthesis of 4-Acryloylbenzophenone



Scheme 8.2. Synthetic route of 4-acryloylbenzophenone (ABP).

4-hydroxybenzophenone (20 g, 0.1 mol), 2,6-lutidine (11.78 g, 0.11 mol) and 80 mL DCM were added into a round bottom flask. The mixture was stirred in an ice bath. After 30 min, acryloyl chloride (9.9 g, 0.11 mol) was dropwise into the reaction mixture. The reaction was carried out under stirring at room temperature for 4 h. The product was washed three times with water and brine then dried over anhydride Na_2SO_4 . The crude product solution was passed through a silica gel column with DCM as eluent. Volatiles were removed under reduced pressure and 14.7g of a white solid was obtained in a yield of 62 %. ^1H NMR (400 MHz, CD_2Cl_2): δ (ppm) 7.85 (d, 2H, -CH- from aryl), 7.82 (d, 2H, -CH- from aryl), 7.60 (t, 1H, -CH- from aryl), 7.52 (dd, 2H, -CH- from aryl), 7.27 (d, 1H, -CH- from aryl), 6.64 (dd, 1H, $\text{CH}_2\text{CH-}$), 6.31 (dd, 1H, $\text{CH}_2\text{CH-}$), 6.08 (d, 1H, $\text{CH}_2\text{CH-}$).

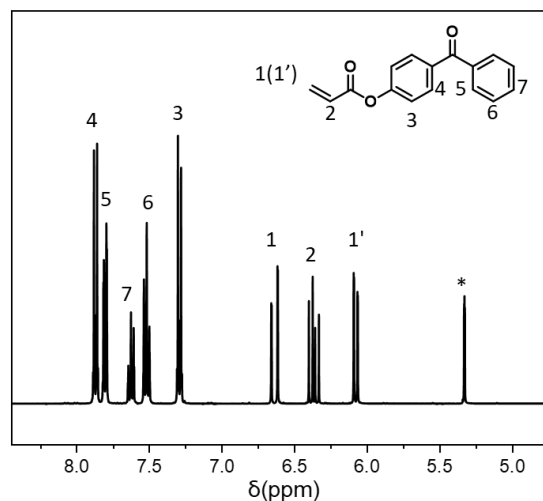
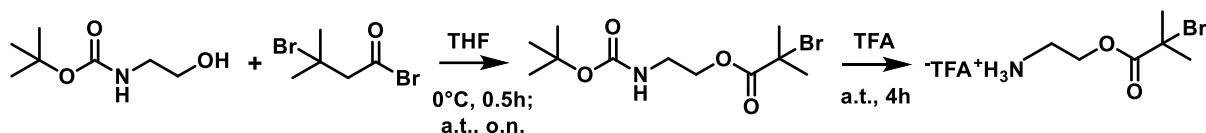


Figure 8.5. ^1H NMR (400 MHz, DCM) spectra of ABP at ambient temperature. The * indicates the residual signal of the solvent CH_2Cl_2 .

8.3.1.3. Synthesis of TFA Salt of *t*-Boc-aminoethyl 2-bromoisobutyrate



Scheme 8.3. Synthetic route of TFA salt of *t*-Boc-aminoethyl 2-bromoisobutyrate (AEBIB**TFA*).

N-Boc-ethanolamine (3.224 g, 0.02 mol) and triethylamine (2.43 g, 0.024 mol) were dissolved in 80 mL of dry DCM and were cooled with an ice bath. Then, 2-bromoisobutyryl bromide (4.87 g, 0.0212 mol) in 20 mL of DCM was added dropwise into the mixture for 0.5 h. The reaction was slowly warmed up to room temperature and stirred overnight. The precipitate was filtered off and the mixture was sequentially washed with saturated sodium bicarbonate solution and DI water three times, respectively. The organic phase was dried over sodium sulfate. After removing excess DCM under reduced pressure, the crude product obtained was purified by column chromatography using silica gel as the stationary phase and DCM/ethyl acetate (V/V, 4:1) as eluent to yield a pale yellow liquid. Finally, the *t*-Boc-aminoethyl 2-bromoisobutyrate was obtained by crystallization in hexane ($-20\text{ }^\circ\text{C}$) as white solid. ^1H NMR (400 MHz, CDCl_3) 4.80 ppm (s, 1H, $-\text{NH}-$), 4.22 ppm (t, 2H, $-\text{CH}_2\text{OCO}-$), 3.44 ppm (q, 2H, $-\text{NHCH}_2-$), 1.92 ppm (s, 6H, $-\text{C}(\text{CH}_3)_2\text{Br}$), 1.43 ppm (s, 9H, $-\text{NH}-$

$C(CH_3)_3$. *t*-Boc-aminoethyl 2-bromoisobutyrate (8.0 g, 0.026 mol) was dissolved in 20 mL of trifluoroacetic acid (TFA). After vigorous stirring for 4 h, excess TFA was removed by rotary evaporation. The TFA salt of *t*-Boc-aminoethyl 2-bromoisobutyrate (AEBIB**TFA*) was obtained as a white solid by recrystallization of the crude product from diethyl ether by keeping the solution at $-20\text{ }^\circ\text{C}$ for two nights. The white solid was filtered and dried under vacuum. $^1\text{H NMR}$ (400 MHz, CDCl_3) $\delta(\text{ppm})$ 8.25 (s, 1H, $\text{TFA}^-\text{NH}_3^+\text{CH}_2^-$), 4.48 (t, 2H, $-\text{CH}_2\text{OCO}-$), 3.34 (t, 2H, $\text{TFA}^-\text{NH}_3^+\text{CH}_2^-$), 1.94 (s, 6H, $-\text{C}(\text{CH}_3)_2\text{Br}$).

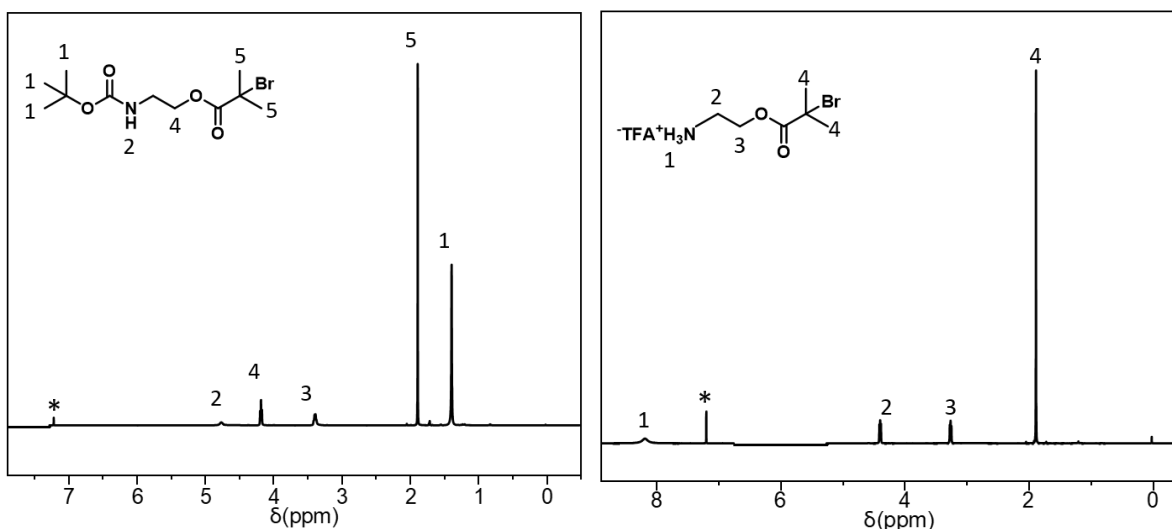
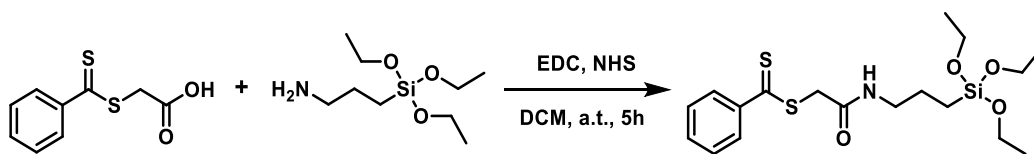


Figure 8.6. $^1\text{H NMR}$ (400 MHz, CDCl_3) spectrum of *t*-Boc-aminoethyl 2-bromoisobutyrate and AEBIB**TFA*. The * indicates the residual signal of the solvent CHCl_3 . Adapted with permission from Ref. [181], copyright (2020) John Wiley and Sons.

8.3.1.4. Synthesis of 2-Oxo-2-((3-(triethoxysilyl)propyl)amino)ethyl benzodithioate



Scheme 8.4. Synthetic route of 2-oxo-2-((3-(triethoxysilyl)propyl)amino)ethyl benzodithioate (*S*-CTA).

Surface chain transfer agent, 2-oxo-2-((3-(triethoxysilyl)propyl)amino)ethyl benzodithioate S-CTA was synthesized as follows: *S*-(thiobenzoyl)thioglycolic acid (2 g, 9.4 mmol), *N*-ethyl-*N'*-(3-dimethylaminopropyl)carbodiimide hydrochloride (2 g, 10.32 mmol), and *N*-hydroxysuccinimide (1.2 g, 10.32 mmol) were dissolved in 70 mL anhydrous DCM, and then cooled in an ice bath. Subsequently, (3-aminopropyl)triethoxysilane (2.08 g, 9.4 mmol) in 10 mL cold anhydrous DCM was dropwise added into the mixture. The reaction was then continuously stirred at ambient temperature for 5 h. Afterwards, the mixture was washed three times with brine and then dried from anhydrous Na₂SO₄. A red oil was obtained as product after evaporation of solvent with a yield of 88 %. The S-CTA was stored under -20 °C before usage. ¹H NMR (400 MHz, CDCl₃) δ(ppm) 8.02 (dd, H, -CH- from aryl), 7.55 (t, 2H, -CH- from aryl), 7.39 (t, 2H, -CH- from aryl), 6.45 (t, H, -NH-), 4.15 (s, 2H, -SCH₂C-), 3.76 (q, 6H, -OCH₂CH₃), 3.24 (m, 2H, -NHCH₂CH₂-), 1.57 (m, 2H, -NHCH₂CH₂-), 1.19 (t, 9H, -OCH₂CH₃), 0.55 (t, 2H, -CH₂CH₂Si-).

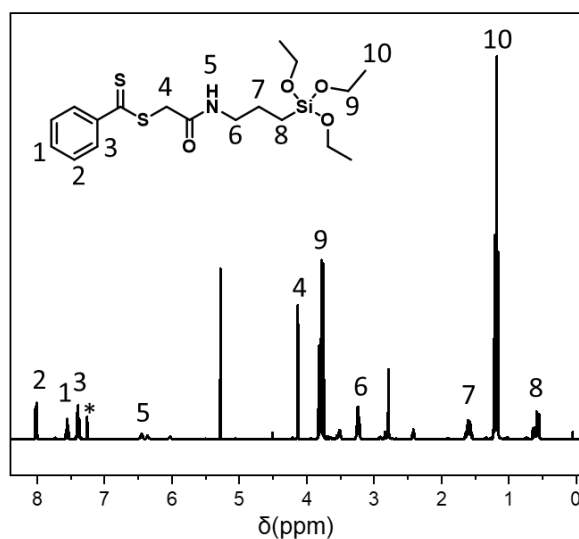
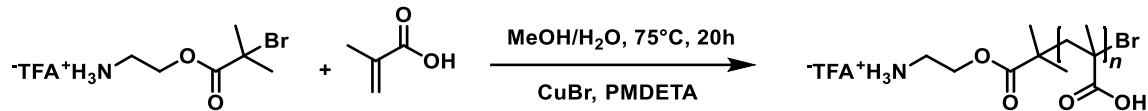


Figure 8.7. ¹H NMR (400 MHz, CDCl₃) spectrum of 2-oxo-2-[[3-(triethoxysilyl)propyl]amino]ethyl ester benzenecarbodithioic acid. The * indicates the residual signal of the solvent CHCl₃.

8.3.1.5. Synthesis of Amine-ended PMAA via ATRP



Scheme 8.5. Synthetic route of poly(methacrylic acid) (PMAA).

The typical procedure of atom transfer radical polymerization of poly(methacrylic acid) (PMAA) was as follows. PMDETA (50 μ L, 0.236 mmol) was dissolved in 1 mL DI water in a Schlenk tube and three freeze-pump-thaw cycles were performed. Then CuBr (16.9 mg, 0.118 mmol) was added over the frozen solution. MAA was dissolved in 1 mL methanol and degassed by three freeze-pump-thaw cycles and added into reaction system. Then AEBiB*TFA (76.7 mg, 0.236 mmol) was added and three times freeze-pump-thaw cycles was carried out again before immersed in pre-heated oil bath at 75 °C react for 20 h. The reaction was quenched by cooling with liquid nitrogen, the final product was precipitate in acetone and dialysis against methanol, dried under vacuum at 40 °C. ¹H NMR (400 MHz, DMSO-d₆) δ (ppm) 12.33 (s, 1H, -CH₂(CH₃)C(COOH)), 1.50-2.05 (s, 2H, -CH₂(CH₃)C(COOH)- the backbone of PMAA), 0.56-1.16 (s, 3H, -CH₂(CH₃)C(COOH)).

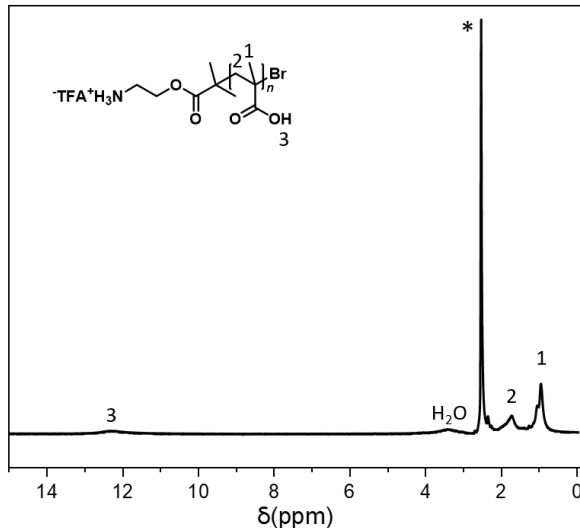


Figure 8.8. ¹H NMR (400 MHz, DMSO-d₆) spectrum of PMAA. The * indicates the residual signal of the solvent DMSO. Adapted with permission from Ref. [181], copyright (2020) John Wiley and Sons.

8.3.2. Fabrication Procedures

8.3.2.1. Preparation of Anodic Aluminum Oxide Template (Chapter 4, 5, 6)

AAO templates were prepared using a two-step anodization.^[205] 99.999 % pure aluminum discs were mounted in a tetrafluoroethylene case and then processed with electro-polishing at 20 V, 5 °C for 6 min in an electrolyte bath mixed with ethanol and perchloric acid (V/V, 3:1) to form a flat surface. Then the first anodization process was carried out. Upon cooling the electropolished aluminum disks were treated at 3~5 °C under a voltage of 175 V for 3 h, after that the voltage was increased to 195 V for 20 h. In this process, 1 wt% phosphoric acid (H₃PO₄) was used as bath solution. After first anodization treatment, an irregular layer of aluminum oxide pores was formed and then this layer was removed by an etching step using a mixed aqueous solution of chromic oxide solution (1.8 wt%) and phosphoric acid (6.0 wt%) at 45 °C for 36 h. Later on, the chamber contained aluminum disks were washed thoroughly with deionized water. Following the first step, a second anodization step proceeded under the voltage of 195 V for 1 h, 6 h and 20 h, respectively, in 1 wt% phosphoric acid at 3~5 °C. The attained AAO templates were washed and sonicated with acetone and dried. A wet chemical etching in 10 wt% H₃PO₄ at 45 °C was applied to selected AAO template for pore widening for 1 h. And then all the AAO template was washed and sonicated with acetone, and dried at 45 °C.

8.3.2.2. Fabrication of Janus PS-*b*-PNIPAm Nanorods (Chapter 4)

A styrene solution was prepared by dissolving styrene (100 mg) 2,2'-azobis(isobutyronitrile) (1 mg), 1,6-hexanediol diacrylate (10 mg) and 4-acryloylbenzophenone (10 mg) in 1,4-dioxane (100 μL). The solution was drop casted onto the prepared AAO template followed by pressing the template between two glass sides and transferred into a vacuum oven. The temperature was increased from 40 °C to 80 °C and was kept at 80 °C for 8 h. The polymerization was performed under vacuum and steps were operated in absence of light. After the synthesis of polystyrene in the AAO template the template underwent oxygen plasma treatment. A NIPAm solution consisting of NIPAm (100 mg) together with 2,2'-azobis(isobutyronitrile) (1 mg), *N,N'*-methylenebis(acrylamide) (1 mg) and 4-acryloylbenzophenone (1 mg) in 1,4-dioxane (200 μL) was added onto the template, and pressed in between two glass sides. The sample was then

processed with the same polymerization conditions. After polymerization, the template was treated with UV (365 nm) for 1 h, hence chemically bonded polystyrene-*block*-poly(*N*-isopropylacrylamide) (PS-*b*-PNIPAm) Janus nanorods were formed within the AAO template. Subsequently, the Janus nanorods were released from the AAO template by dissolving the template in 10 wt% aqueous phosphoric acid at 45 °C for 2 h, the Janus nanorods were collected by further filtration and washed thoroughly with deionized water.

8.3.2.3. Fabrication of Janus PNIPAm-*b*-PPFPA Nanorods (Chapter 4)

N-isopropylacrylamide solution was prepared following the same recipe illustrated in 8.3.2.2. After polymerization in the AAO template, oxygen plasma treatment was carried out. Afterwards, PFFPA solution containing PFFPA (100 mg), 2,2'-azobis(isobutyronitrile) (1 mg), 1,6-hexanediol diacrylate (2.5 mg), 4-acryloylbenzophenone (2.5 mg) and 1,4-dioxane (100 μ L) was drop casted onto the AAO membrane. After polymerization, the template was again treated under UV (365 nm) for 1 h, followed the Janus poly(*N*-isopropylacrylamide)-*block*-poly(pentafluorophenyl acrylate) (PNIPAm-*b*-PPFPA) nanorods were dissolved from AAO washed thoroughly before further characterization.

8.3.2.4 Fabrication of Janus PPYNP-*b*-PMMA Nanorods (Chapter 4)

Polypyrrole nanoparticles (PPYNPs) were prepared using FeCl₃, NaOAc and pyrrole in distilled water. To start, NaOAc (82 mg, 1 mmol) together with pyrrole (70 μ L, 0.001 mmol) were dissolved in 5 mL DI water, in another sample vial, FeCl₃ (162 mg, 1 mmol) was dissolved in 5 ml DI water. Until formation of a homogenous solution, two solutions were added into the sample vial with AAO template. After 30 min sonication at room temperature, PPYNPs were formed on the surface and inside the cannulas of AAO membrane. The SEM image of formed PPYNPs were illustrated in Figure 8.9, with average diameter of \approx 180 nm. After that oxygen plasma treatment was carried out for 30 min. Poly(methyl methacrylate) (PMMA) was synthesized on top of PPYNPs in AAO cannulas. MMA solution, which contained MMA (100 mg), 4-acryloylbenzophenone (10 mg), Irgacure 2959 (5 mg) and 1,4-dioxane (100 μ L), were drop casted onto the AAO membrane and 1

h of photoinitiated polymerization was carried out under UV (365 nm). The formed Janus polypyrrole nanoparticle-*block*-poly(methyl methacrylate) (PPYNP-*b*-PMMA) nanorods were dissolved out of the AAO membrane and was washed with DI water before further characterization.

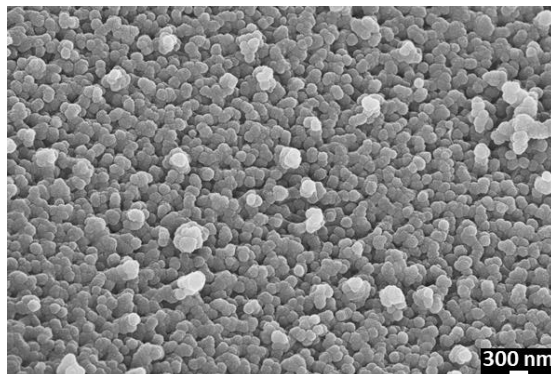


Figure 8.9. SEM image of polypyrrole nanoparticles (PPYNPs).

8.3.2.5. Silanization of Polyester Film (Chapter 5)

Melinex film was cut into 2.5*2.5 cm square sheets and washed with methanol. These sheets were then immersed into 4.5 M sodium hydroxide solution at 90 °C for 2 h of hydrolysis. Afterwards the polyester sheets were washed with DI water and dried in 45 °C drying oven. Then 30 min oxygen plasma treatment was carried out and the sheets were directly immersed into 3-(trimethoxysilyl)propyl methacrylate/toluene (V/V, 1/100) at 90 °C overnight. Modified films were washed with ethanol and dried before usage.

8.3.2.6. Preparation of Pillar-PPFPA (Chapter 5)

Monomer pentafluorophenyl acrylate (1 g), photocrosslinker 4-acryloylbenzophenone (50 mg), crosslinker 1,6-hexanediol diacrylate (50 mg) and photo-initiator Irgacure 2959 (50 mg) was added into 200 μ L THF, sealed, and shaking for 1 h until a homogenous solution was obtained. Then 100 μ L monomer solution was dropped onto the prepared AAO template and gently covered with a silanized PET film. The sample was then treated with UV (365 nm, 1 W cm⁻²) for 1 h. The Al layer was dissolved in CuCl₂/HCl solution and Al₂O₃ layer in 10 wt% H₃PO₄ solution, then washed thoroughly with DI water and finally dried under ambient temperature.

8.3.2.7. Post-polymerization Modification of Pillar-PPFPA with PMAA (Chapter 5)

PMAA (300 mg) polymer was dissolved in 15 mL DMSO and shaken to form a homogenous solution. Then the PPFPA micro-pillar film was immersed into PMAA/DMSO solution and shake at room temperature for 12 h, 24 h, 36 h, and 48 h, respectively. Afterwards, the film was washed thoroughly with ethanol and water, then dried at room temperature.

8.3.2.8. Preparation of Flat-PPFPA (Chapter 5)

The same monomer solution was prepared as for the preparation of pillar-PPFPA. The monomer solution was spread onto a silanized PET film via spin coating with a speed of 1000 rpm/s for 10 s. Afterwards the film was UV polymerized for 1 h, and then washed thoroughly with ethanol and DI water before it was dried under ambient temperature.

8.3.2.9. Post-polymerization Modification of Flat-PPFPA with PMAA (Chapter 5)

The flat-PPFPA film was immersed into the same PMAA solution in DMSO as illustrated in the post-polymerization modification of pillar-PPFPA and after same modification time, the sample was taken out and rinsed thoroughly with ethanol and water before dried under ambient temperature.

8.3.2.10. Immobilization of S-CTA onto AAO Membrane (Chapter 6)

The pristine AAO membrane was immersed in concentrated H_2O_2 for 15 min at room temperature and then processed via 10 min oxygen plasma treatment. The silica solution consisted of 100 mg silicon dioxide, 10 mL ethanol, 200 μL 0.1M HCl and 1 mL TEOS and was sonicated to form a homogenous solution. Subsequently, the silica solution was spin coated onto the hydrolyzed AAO membrane at a speed of 1500 rpm for 30 s. Afterwards the AAO membrane was cured in oven at 120 °C for 2 h and was washed thoroughly and dried. Pre-treated AAO membrane, 100 mg S-CTA and 10 mL dry toluene was added into a round bottom flask sealed with a rubber septum. Afterwards, the immobilization reaction was carried out in a water bath shaker at 40 °C overnight.

Further, the membrane was rinsed with DCM and cured in oven at 120 °C for 2 h. It was washed and dried under reduced pressure before usage.

8.3.2.11. SI-RAFT Polymerization of Poly(MMA-*co*-DEAEMA) on AAO Membrane (Chapter 6)

The preparation of poly(methyl methacrylate-*co*-2-(diethylamino)ethyl methacrylate) on AAO membrane (AAO-*g*-PMD) was achieved by SI-RAFT polymerization of MMA and DEAEMA onto S-CTA anchored AAO membrane according to the following procedure. AAO-*g*-CTA, MMA, DEAEMA, AIBN, free CTA (*S*-(thiobenzoyl)thioglycolic acid) and anhydrous 1,4-dioxane were added into a Schlenk flask (Table 8.1). The mixture was degassed by three freeze-pump-thaw cycles. Simultaneously, the AAO membrane was degassed with N₂ in another Schlenk flask. Afterwards, the monomer mixture was transferred in to the AAO contained flask and put into a preheated shaking bath at 70 °C for 4 h. After polymerization, the AAO membrane was taken out and washed thoroughly with DMF, DCM and acetone and dried at ambient environment. ¹H NMR (400 MHz, CDCl₃) δ(ppm) 8.02 (dd, 6H, -CH- from aryl), 7.50 (t, 1H, -CH- from aryl), 7.34 (t, 2H, -CH- from aryl), 4.15 (s, 2H, -CH₂-COOH), 4.01 (t, 2H, -O-CH₂-CH₂-), 3.59 (s, 3H, -O-CH₃), 2.71 (t, 2H, -O-CH₂-CH₂-), 2.57 (q, 2H, -N-CH₂-CH₃), 2.14-1.64 (s, 2H, -CH₂- from the polymer backbone), 1.16-0.68 (t, 3H, -CH₂-CH₃ from the polymer backbone), 0.87 (t, 3H, -N-CH₂-CH₃).

Table 8.1. Detailed recipe for synthesis of poly(methyl methacrylate-*co*-2-(diethylamino)ethyl methacrylate).

	<i>MMA</i>	<i>DEAEMA</i>	<i>AIBN</i>	<i>CTA</i>	<i>1, 4-dioxane</i>
<i>PMD-1</i>	600 mg, 6 mmol	740 mg, 4 mmol	3.28 mg, 0.02 mmol	42.4 mg, 0.2 mmol	10 ml
<i>PMD-2</i>	600 mg, 6 mmol	740 mg, 4 mmol	1.64 mg, 0.01 mmol	21.2 mg, 0.1 mmol	10 ml
<i>PMD-3</i>	600 mg, 6 mmol	740 mg, 4 mmol	0.328 mg, 0.002 mmol	4.24 mg, 0.02 mmol	10 ml

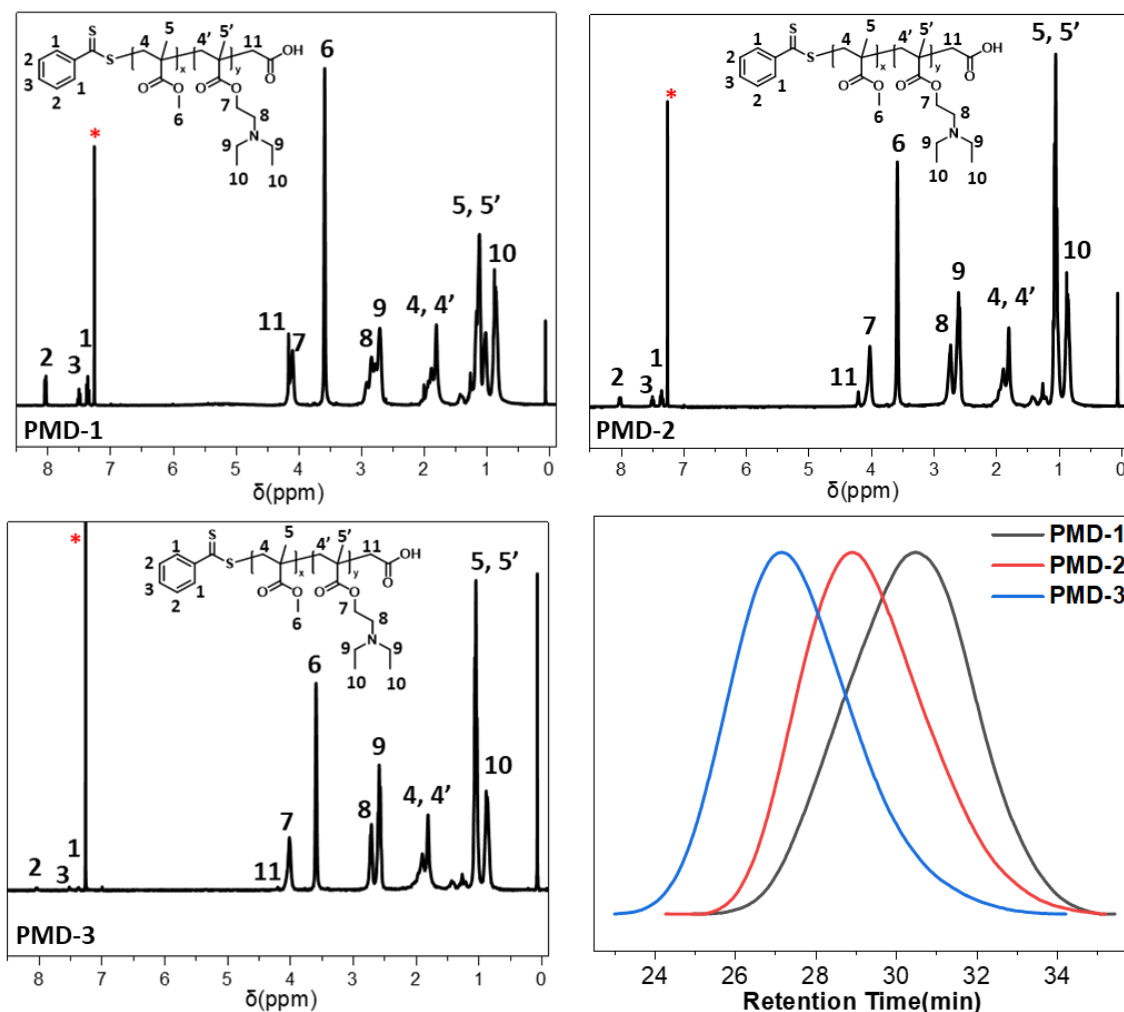


Figure 8.10. ^1H NMR (400 MHz, CDCl_3) spectrum and GPC curve of in DMAc of PMD-1, PMD-2 and PMD-3. The * indicates the residual signal of the solvent CHCl_3 .

8.3.2.12. Flux experiment (Chapter 6)

The flux test was carried out using a commercially available filtration funnel (Figure 8.11). The AAO membrane was placed on a fritted sand core support and tightly sealed with an O-ring to prevent any leakage. Permeation experiments were performed at a pressure of 0.11 bar at room temperature, all the eluate was collected in the conical flask. For controlled water flux testing, the eluate was weighted every 5 min for five times at each condition. The transition was achieved by alternatively purging with CO_2 for 5 min or N_2 for 10 min at ambient environment.

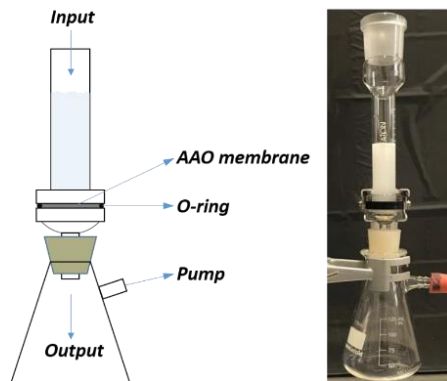


Figure 8.11. A schematic (left) and optical image (right) of flux measurement cell.

8.3.2.13. Emulsion Preparation (Chapter 6)

The typical recipe of oil-in-water emulsion is as follows: toluene and buffer solution (pH 5 ± 0.02) mixed in 1/100 (v/v) with the addition of 0.1 mg/mL SDS. The emulsion was sonicated for 15 min to form a homogenous oil-in-water emulsion solution before usage. For the water-in-oil emulsion, the volume ratio of distilled water and toluene is 1/100 (v/v). The mixture solution was carried out via 15 min sonication.

9. Reference

- [1] J. Jeevanandam, A. Barhoum, Y. S. Chan, A. Dufresne, M. K. Danquah, *Beilstein J. Nanotechnol.* **2018**, *9*, 1050.
- [2] C. R. Martin, *Science.* **1994**, *266*, 1961.
- [3] B. D. Gates, Q. Xu, M. Stewart, D. Ryan, C. G. Willson, G. M. Whitesides, *Chem. Rev.* **2005**, *105*, 1171.
- [4] N. Haberkorn, *Template-Assisted Patterning of Functional Polymers*, Universitätsbibliothek Mainz, **2010**.
- [5] H. Yan, *Preparation and Optical Characterization of Nanoporous Templates as a Basis for Nanocontact Arrays*, Technische Universität Braunschweig, **2012**.
- [6] J. R. Davis, *Corrosion of Aluminum and Aluminum Alloys*, Asm International, **1999**.
- [7] L. H. Hihara, R. P. I. Adler, R. M. Latanision, *Environmental Degradation of Advanced and Traditional Engineering Materials*, CRC Press, **2013**.
- [8] E. McCafferty, *Corros. Sci.* **2003**, *45*, 1421.
- [9] H. Buff, *Justus Liebigs Ann. Chem.* **1857**, *102*, 265.
- [10] G. D. Bengough, J. M. Stuart, *UK Pat.* **1923**, 223.
- [11] S. Kawai, I. Ishiguro, *J. Electrochem. Soc.* **1976**, *123*, 1047.
- [12] S. Kawai, R. Ueda, *J. Electrochem. Soc.* **1975**, *122*, 32.
- [13] H. Masuda, K. Fukuda, *Science.* **1995**, *268*, 1466.
- [14] H. Masuda, M. Satoh, *Jpn. J. Appl. Phys.* **1996**, *35*, L126.
- [15] F. Keller, M. S. Hunter, D. L. Robinson, *J. Electrochem. Soc.* **1953**, *100*, 411.
- [16] T. Y. Kim, S. H. Jeong, *Korean J. Chem. Eng.* **2008**, *25*, 609.
- [17] M. Steinhart, in *Self-Assembled Nanomater. II*, Springer, **2008**, pp. 123–187.
- [18] F. Zhang, X. Liu, C. Pan, J. Zhu, *Nanotechnology* **2007**, *18*, 345302.

- [19] A. Rath, P. Theato, *Adv. Funct. Mater.* **2020**, *30*, 1902959.
- [20] W. Lee, S. J. Park, *Chem. Rev.* **2014**, *114*, 7487.
- [21] A. R. Despić, *J. Electroanal. Chem. interfacial Electrochem.* **1985**, *191*, 417.
- [22] Z. Su, M. Bühl, W. Zhou, *J. Am. Chem. Soc.* **2009**, *131*, 8697.
- [23] S. K. Thamida, H.-C. Chang, *Chaos An Interdiscip. J. Nonlinear Sci.* **2002**, *12*, 240.
- [24] F. Li, L. Zhang, R. M. Metzger, *Chem. Mater.* **1998**, *10*, 2470.
- [25] S. Zhao, K. Chan, A. Yelon, T. Veres, *Adv. Mater.* **2007**, *19*, 3004.
- [26] O. Jessensky, F. Müller, U. Gösele, *Appl. Phys. Lett.* **1998**, *72*, 1173.
- [27] A. Güntherschulze, H. Betz, *Zeitschrift für Phys.* **1931**, *68*, 145.
- [28] A. Güntherschulze, H. Betz, *Zeitschrift für Phys.* **1934**, *92*, 367.
- [29] A. M. M. Jani, D. Losic, N. H. Voelcker, *Prog. Mater. Sci.* **2013**, *58*, 636.
- [30] G. E. Thompson, *Thin Solid Films* **1997**, *297*, 192.
- [31] J. E. Houser, K. R. Hebert, *Nat. Mater.* **2009**, *8*, 415.
- [32] J. Sarkar, G. G. Khan, A. Basumallick, *Bull. Mater. Sci.* **2007**, *30*, 271.
- [33] S.-H. Su, C.-S. Li, F.-B. Zhang, M. Yokoyama, *Superlattices Microstruct.* **2008**, *44*, 514.
- [34] W. J. Stępniewski, Z. Bojar, *Surf. Coatings Technol.* **2011**, *206*, 265.
- [35] J. Zhang, J. E. Kielbasa, D. L. Carroll, *Mater. Chem. Phys.* **2010**, *122*, 295.
- [36] J. P. O'sullivan, G. C. Wood, *Proc. R. Soc. London. A. Math. Phys. Sci.* **1970**, *317*, 511.
- [37] A. Belwalkar, E. Grasing, W. Van Geertruyden, Z. Huang, W. Z. Misiolek, *J. Memb. Sci.* **2008**, *319*, 192.
- [38] O. Nishinaga, T. Kikuchi, S. Natsui, R. O. Suzuki, *Sci. Rep.* **2013**, *3*, 2748.
- [39] J. Martin, J. Maiz, J. Sacristan, C. Mijangos, *Polymer (Guildf).* **2012**, *53*, 1149.
- [40] J. M. Montero Moreno, M. Waleczek, S. Martens, R. Zierold, D. Görlitz, V. V. Martínez, V. M. Prida, K. Nielsch, *Adv. Funct. Mater.* **2014**, *24*, 1857.

- [41] Y. Lei, W. Cai, G. Wilde, *Prog. Mater. Sci.* **2007**, *52*, 465.
- [42] J. Li, C. Papadopoulos, J. Xu, *Nature* **1999**, *402*, 253.
- [43] G. Meng, Y. J. Jung, A. Cao, R. Vajtai, P. M. Ajayan, *Proc. Natl. Acad. Sci.* **2005**, *102*, 7074.
- [44] W. Lee, R. Ji, U. Gösele, K. Nielsch, *Nat. Mater.* **2006**, *5*, 741.
- [45] D. Losic, M. Lillo, D. Losic Jr, *small* **2009**, *5*, 1392.
- [46] M. Steinhart, J. H. Wendorff, A. Greiner, R. B. Wehrspohn, K. Nielsch, J. Schilling, J. Choi, U. Gösele, *Science*. **2002**, *296*, 1997.
- [47] J. Martin, C. Mijangos, *Langmuir* **2008**, *25*, 1181.
- [48] M. Zhang, P. Dobriyal, J.-T. Chen, T. P. Russell, J. Olmo, A. Merry, *Nano Lett.* **2006**, *6*, 1075.
- [49] S. Schlitt, A. Greiner, J. H. Wendorff, *Macromolecules* **2008**, *41*, 3228.
- [50] J.-T. Chen, T.-H. Wei, C.-W. Chang, H.-W. Ko, C.-W. Chu, M.-H. Chi, C.-C. Tsai, *Macromolecules* **2014**, *47*, 5227.
- [51] R. V Parthasarathy, C. R. Martin, *Chem. Mater.* **1994**, *6*, 1627.
- [52] B. Sanz, N. Ballard, J. M. Asua, C. Mijangos, *Macromolecules* **2017**, *50*, 811.
- [53] A. M. Md Jani, D. Losic, N. H. Voelcker, *Prog. Mater. Sci.* **2013**, *58*, 636.
- [54] Y. Cui, C. Tao, S. Zheng, Q. He, S. Ai, J. Li, *Macromol. Rapid Commun.* **2005**, *26*, 1552.
- [55] Y. Wang, A. S. Angelatos, F. Caruso, *Chem. Mater.* **2008**, *20*, 848.
- [56] R. R. Costa, J. F. Mano, in *Nanomater. Tissue Eng.*, Elsevier, **2013**, pp. 88–118.
- [57] S. Ai, G. Lu, Q. He, J. Li, *J. Am. Chem. Soc.* **2003**, *125*, 11140.
- [58] C. S. Peyratout, L. Dähne, *Angew. Chemie Int. Ed.* **2004**, *43*, 3762.
- [59] P. C. Stair, C. Marshall, G. Xiong, H. Feng, M. J. Pellin, J. W. Elam, L. Curtiss, L. Iton, H. Kung, M. Kung, H.-H. Wang, *Top. Catal.* **2006**, *39*, 181.

- [60] S. Hou, C. C. Harrell, L. Trofin, P. Kohli, C. R. Martin, *J. Am. Chem. Soc.* **2004**, *126*, 5674.
- [61] O. Azzaroni, K. H. A. Lau, *Soft Matter* **2011**, *7*, 8709.
- [62] H. J. Fan, P. Werner, M. Zacharias, *Small* **2006**, *2*, 700.
- [63] J. Duay, E. Gillette, J. Hu, S. B. Lee, *Phys. Chem. Chem. Phys.* **2013**, *15*, 7976.
- [64] A. Brzózka, K. Fic, J. Bogusz, A. Brudzisz, M. Marzec, M. Gajewska, G. Sulka, *Nanomaterials* **2019**, *9*, 307.
- [65] M. Lahav, E. A. Weiss, Q. Xu, G. M. Whitesides, *Nano Lett.* **2006**, *6*, 2166.
- [66] L. Wen, Z. Wang, Y. Mi, R. Xu, S.-H. Yu, Y. Lei, *Small* **2015**, *11*, 3408.
- [67] C. Mijangos, R. Hernandez, J. Martin, *Prog. Polym. Sci.* **2016**, *54*, 148.
- [68] Q. Hao, H. Huang, X. Fan, X. Hou, Y. Yin, W. Li, L. Si, H. Nan, H. Wang, Y. Mei, others, *Nanotechnology* **2017**, *28*, 105301.
- [69] M. P. Murphy, S. Kim, M. Sitti, *ACS Appl. Mater. Interfaces* **2009**, *1*, 849.
- [70] G. Carbone, E. Pierro, S. N. Gorb, *Soft Matter* **2011**, *7*, 5545.
- [71] E. Arzt, S. Gorb, R. Spolenak, *Proc. Natl. Acad. Sci.* **2003**, *100*, 10603.
- [72] C. Greiner, A. del Campo, E. Arzt, *Langmuir* **2007**, *23*, 3495.
- [73] A. del Campo, C. Greiner, I. Álvarez, E. Arzt, *Adv. Mater.* **2007**, *19*, 1973.
- [74] M. Jin, X. Feng, L. Feng, T. Sun, J. Zhai, T. Li, L. Jiang, *Adv. Mater.* **2005**, *17*, 1977.
- [75] D. Y. Lee, D. H. Lee, S. G. Lee, K. Cho, *Soft Matter* **2012**, *8*, 4905.
- [76] L. Xue, A. Kovalev, F. Thöle, G. T. Rengarajan, M. Steinhart, S. N. Gorb, *Langmuir* **2012**, *28*, 10781.
- [77] A. Gombert, W. Glaubitt, K. Rose, J. Dreibholz, B. Bläsi, A. Heinzl, D. Sporn, W. Döll, V. Wittwer, *Thin Solid Films* **1999**, *351*, 73.
- [78] A. Nakajima, A. Fujishima, K. Hashimoto, T. Watanabe, *Adv. Mater.* **1999**, *11*, 1365.

- [79] S. G. Lee, D. Y. Lee, H. S. Lim, D. H. Lee, S. Lee, K. Cho, *Adv. Mater.* **2010**, *22*, 5013.
- [80] M. I. Gibson, R. K. O'Reilly, *Chem. Soc. Rev.* **2013**, *42*, 7204.
- [81] J. I. Clodt, V. Filiz, S. Rangou, K. Buhr, C. Abetz, D. Höche, J. Hahn, A. Jung, V. Abetz, *Adv. Funct. Mater.* **2013**, *23*, 731.
- [82] B. Liu, H. Zhou, S. Zhou, H. Zhang, A.-C. Feng, C. Jian, J. Hu, W. Gao, J. Yuan, *Macromolecules* **2014**, *47*, 2938.
- [83] L. T. de Haan, J. M. N. Verjans, D. J. Broer, C. W. M. Bastiaansen, A. P. H. J. Schenning, *J. Am. Chem. Soc.* **2014**, *136*, 10585.
- [84] R. G. Joshi, B. V. R. Tata, J. Brijitta, in *AIP Conf. Proc.*, **2011**, pp. 208–209.
- [85] J. Liu, Y. Lu, *J. Am. Chem. Soc.* **2005**, *127*, 12677.
- [86] W. L. Zhang, H. J. Choi, *Polymers (Basel)*. **2014**, *6*, 2803.
- [87] A. S. Hoffman, P. S. Stayton, *Prog. Polym. Sci.* **2007**, *32*, 922.
- [88] Y. G. Takei, T. Aoki, K. Sanui, N. Ogata, T. Okano, Y. Sakurai, *Bioconjug. Chem.* **1993**, *4*, 42.
- [89] P. Gupta, K. Vermani, S. Garg, *Drug Discov. Today* **2002**, *7*, 569.
- [90] J. Hu, H. Meng, G. Li, S. I. Ibekwe, *Smart Mater. Struct.* **2012**, *21*, 53001.
- [91] M. Rajagopalan, J. H. Jeon, I. K. Oh, *Sensors Actuators, B Chem.* **2010**, *151*, 198.
- [92] J. Liu, *Soft Matter* **2011**, *7*, 6757.
- [93] J. E. Stumpel, D. J. Broer, A. P. H. J. Schenning, *Chem. Commun.* **2014**, *50*, 15839.
- [94] B. Jeong, A. Gutowska, *TRENDS Biotechnol.* **2002**, *20*, 305.
- [95] J. F. Mano, *Adv. Eng. Mater.* **2008**, *10*, 515.
- [96] E. Fleige, M. A. Quadir, R. Haag, *Adv. Drug Deliv. Rev.* **2012**, *64*, 866.
- [97] F. Guo, Z. Guo, *RSC Adv.* **2016**, *6*, 36623.
- [98] Y. Liu, X. Wang, B. Fei, H. Hu, C. Lai, J. H. Xin, *Adv. Funct. Mater.* **2015**, *25*, 5047.

- [99] L. Dong, A. K. Agarwal, D. J. Beebe, H. Jiang, *Nature* **2006**, *442*, 551.
- [100] R. Liu, M. Fraylich, B. R. Saunders, *Colloid Polym. Sci.* **2009**, *287*, 627.
- [101] C. Pietsch, R. Hoogenboom, U. S. Schubert, *Polym. Chem.* **2010**, *1*, 1005.
- [102] M. R. Aguilar, J. San Román, *Smart Polymers and Their Applications*, Woodhead Publishing, **2019**.
- [103] B. Sanz, C. Von Bilderling, J. S. Tuninetti, L. Pietrasanta, C. Mijangos, G. S. Longo, O. Azzaroni, J. M. Giussi, *Soft Matter* **2017**, *13*, 2453.
- [104] J. M. Giussi, C. Von Bilderling, E. Alarcón, L. I. Pietrasanta, R. Hernandez, P. Rafael, M. Vázquez, C. Mijangos, M. L. Cortez, O. Azzaroni, *Nanoscale* **2018**, *10*, 1189.
- [105] X. Guo, L. Wang, X. Wei, S. Zhou, *J. Polym. Sci. Part A Polym. Chem.* **2016**, *54*, 3525.
- [106] H. G. Schild, *Prog. Polym. Sci.* **1992**, *17*, 163.
- [107] T. Aoki, K. Nakamura, K. Sanui, A. Kikuchi, T. Okano, Y. Sakurai, N. Ogata, *Polym. J.* **1999**, *31*, 1185.
- [108] S. Saeki, N. Kuwahara, M. Nakata, M. Kaneko, *Polymer (Guildf)*. **1976**, *17*, 685.
- [109] R. Longenecker, T. Mu, M. Hanna, N. A. D. Burke, H. D. H. Stöver, *Macromolecules* **2011**, *44*, 8962.
- [110] H. Y. Liu, X. X. Zhu, *Polymer (Guildf)*. **1999**, *40*, 6985.
- [111] J. Seuring, F. M. Bayer, K. Huber, S. Agarwal, *Macromolecules* **2012**, *45*, 374.
- [112] D. Crespy, R. M. Rossi, *Polym. Int.* **2007**, *56*, 1461.
- [113] P. J. Roth, F. D. Jochum, P. Theato, *Soft Matter* **2011**, *7*, 2484.
- [114] A. S. Dubovik, E. E. Makhaeva, V. Y. Grinberg, A. R. Khokhlov, *Macromol. Chem. Phys.* **2005**, *206*, 915.
- [115] J. Seuring, S. Agarwal, *Macromolecules* **2012**, *45*, 3910.
- [116] S. Dai, K. C. Tam, *Langmuir* **2004**, *20*, 2177.
- [117] I. Roy, M. N. Gupta, *Chem. Biol.* **2003**, *10*, 1161.

- [118] S. Dai, P. Ravi, K. C. Tam, *Soft Matter* **2008**, *4*, 435.
- [119] D. Schmaljohann, *Adv. Drug Deliv. Rev.* **2006**, *58*, 1655.
- [120] G. Kocak, C. Tuncer, V. Bütün, *Polym. Chem.* **2017**, *8*, 144.
- [121] S. Ma, M. Scaraggi, D. Wang, X. Wang, Y. Liang, W. Liu, D. Dini, F. Zhou, *Adv. Funct. Mater.* **2015**, *25*, 7366.
- [122] T. Du, S. Ma, X. Pei, S. Wang, F. Zhou, *Small* **2017**, *13*, 1602020.
- [123] Y. Wang, A. S. Angelatos, F. Caruso, *Chem. Mater.* **2007**, *20*, 848.
- [124] Y. Zhao, *Chem. Rec.* **2007**, *7*, 286.
- [125] Y. Li, X. Jia, M. Gao, H. He, G. Kuang, Y. Wei, *J. Polym. Sci. Part A Polym. Chem.* **2010**, *48*, 551.
- [126] V. Shibaev, A. Bobrovsky, N. Boiko, *Prog. Polym. Sci.* **2003**, *28*, 729.
- [127] C. J. Barrett, J. Mamiya, K. G. Yager, T. Ikeda, *Soft Matter* **2007**, *3*, 1249.
- [128] G. S. Kumar, D. C. Neckers, *Chem. Rev.* **1989**, *89*, 1915.
- [129] R. Klajn, *Chem. Soc. Rev.* **2014**, *43*, 148.
- [130] R. C. Bertelson, in *Org. Photochromic Thermochromic Compd.*, Kluwer Academic Publishers, Boston, **2006**, pp. 11–83.
- [131] H. Jo, N. Haberkorn, J.-A. Pan, M. Vakili, K. Nielsch, P. Theato, *Langmuir* **2016**, *32*, 6437.
- [132] D. A. Davis, A. Hamilton, J. Yang, L. D. Cremar, D. Van Gough, S. L. Potisek, M. T. Ong, P. V. Braun, T. J. Martínez, S. R. White, J. S. Moore, N. R. Sottos, *Nature* **2009**, *459*, 68.
- [133] J. Y. Choi, J. Y. Kim, H. J. Moon, M. H. Park, B. Jeong, *Macromol. Rapid Commun.* **2014**, *35*, 66.
- [134] H. Liu, S. Lin, Y. Feng, P. Theato, *Polym. Chem.* **2017**, *8*, 12.
- [135] W. Fan, B. C. Yung, X. Chen, *Angew. Chemie Int. Ed.* **2018**, *57*, 8383.

- [136] K. Kuwabara, M. Ogino, S. Motowaki, A. Miyauchi, *Microelectron. Eng.* **2004**, *73*, 752.
- [137] D. S. Peterson, T. Rohr, F. Svec, J. M. J. Fréchet, *Anal. Chem.* **2003**, *75*, 5328.
- [138] W. Zhan, G. H. Seong, R. M. Crooks, *Anal. Chem.* **2002**, *74*, 4647.
- [139] G. Chen, R. L. McCarley, S. A. Soper, C. Situma, J. G. Bolivar, *Chem. Mater.* **2007**, *19*, 3855.
- [140] X. Liu, L. Chen, H. Liu, G. Yang, P. Zhang, D. Han, S. Wang, L. Jiang, *NPG Asia Mater.* **2013**, *5*, 63.
- [141] K. Du, Z. Gan, *ACS Appl. Mater. Interfaces* **2012**, *4*, 4643.
- [142] Y. S. Lin, *Sep. Purif. Technol.* **2001**, *25*, 39.
- [143] D. Routkevitch, T. Bigioni, M. Moskovits, J. M. Xu, *J. Phys. Chem.* **1996**, *100*, 14037.
- [144] K. Liu, Z. Huang, A. Hemmatifar, D. I. Oyarzun, J. Zhou, J. G. Santiago, *ACS Appl. Mater. Interfaces* **2018**, *10*, 26759.
- [145] A. Mutalib Md Jani, E. J. Anglin, S. J. P. McInnes, D. Losic, J. G. Shapter, N. H. Voelcker, *Chem. Commun.* **2009**, 3062.
- [146] Y. Cho, J. Lim, K. Char, *Soft Matter* **2012**, *8*, 10271.
- [147] R. Yang, A. Asatekin, K. K. Gleason, *Soft Matter* **2012**, *8*, 31.
- [148] A. Tufani, G. O. Ince, *J. Appl. Polym. Sci.* **2015**, *132*, 1.
- [149] E. Armagan, G. Ozaydin Ince, *Soft Matter* **2015**, *11*, 8069.
- [150] W. E. Tenhaeff, K. K. Gleason, *Adv. Funct. Mater.* **2008**, *18*, 979.
- [151] D. Losic, M. A. Cole, B. Dollmann, K. Vasilev, H. J. Griesser, *Nanotechnology* **2008**, *19*, 245704.
- [152] A. Tufani, G. Ozaydin Ince, *J. Memb. Sci.* **2017**, *537*, 255.
- [153] D. Roy, M. Semsarilar, J. T. Guthrie, S. Perrier, *Chem. Soc. Rev.* **2009**, *38*, 2046.
- [154] J. S. Kim, T. G. Kim, W. H. Kong, T. G. Park, Y. S. Nam, *Chem. Commun.* **2012**, *48*, 9227.

- [155] Y. Cai, D. Chen, N. Li, Q. Xu, H. Li, J. He, J. Lu, *J. Memb. Sci.* **2018**, 555, 69.
- [156] J. H. Jang, I. In, *Chem. Lett.* **2010**, 39, 1190.
- [157] L. Szuwarzyński Michałand Zaraska, G. D. Sulka, S. Zapotoczny, *Chem. Mater.* **2013**, 25, 514.
- [158] C. Song, M. Wang, X. Liu, H. Wang, X. Chen, L. Dai, *Mater. Sci. Eng. C* **2017**, 78, 748.
- [159] B. Lee, S. Hyun, G. Jeon, E. Y. Kim, J. Kim, W. J. Kim, J. K. Kim, *ACS Appl. Mater. Interfaces* **2016**, 8, 11758.
- [160] S. Ma, J. Liu, Q. Ye, D. Wang, Y. Liang, F. Zhou, *J. Mater. Chem. A* **2014**, 2, 8804.
- [161] G. D. Sulka, A. Brzózka, L. Zaraska, E. Wierzbicka, A. Brudzisz, in *Submicron Porous Mater.*, Springer International Publishing, Cham, **2017**, pp. 107–156.
- [162] K. Tajiri, Y. Saito, Y. Yamanaka, Z. Kabeya, *J. Vac. Sci. Technol. A Vacuum, Surfaces, Film.* **1998**, 16, 1196.
- [163] D. Ma, S. Li, C. Liang, *Corros. Sci.* **2009**, 51, 713.
- [164] G.-Y. Zhao, C.-L. Xu, D.-J. Guo, H. Li, H.-L. Li, *J. Solid State Electrochem.* **2006**, 10, 266.
- [165] C. Y. Han, G. A. Willing, Z. Xiao, H. H. Wang, *Langmuir* **2007**, 23, 1564.
- [166] M. Lattuada, T. A. Hatton, *Nano Today* **2011**, 6, 286.
- [167] F. Tu, D. Lee, *J. Am. Chem. Soc.* **2014**, 136, 9999.
- [168] H. Xie, Z. G. She, S. Wang, G. Sharma, J. W. Smith, *Langmuir* **2012**, 28, 4459.
- [169] X. Ma, K. Hahn, S. Sanchez, *J. Am. Chem. Soc.* **2015**, 137, 4976.
- [170] S. C. Glotzer, M. J. Solomon, *Nat. Mater.* **2007**, 6, 557.
- [171] S. J. Hurst, E. K. Payne, L. Qin, C. A. Mirkin, *Angew. Chemie Int. Ed.* **2006**, 45, 2672.
- [172] J. Park, J. D. Forster, E. R. Dufresne, **2010**, 5960.
- [173] N. Haberkorn, K. Nilles, P. Schattling, P. Theato, *Polym. Chem.* **2011**, 2, 645.

- [174] J. Du, R. K. O'Reilly, *Chem. Soc. Rev.* **2011**, *40*, 2402.
- [175] M. K. Choi, H. Yoon, K. Lee, K. Shin, *Langmuir* **2011**, *27*, 2132.
- [176] N. S. Enikolopyan, M. L. Fridman, I. O. Stalnova, V. L. Popov, in *Fill. Polym. I Sci. Technol.*, Springer, **1990**, pp. 1–67.
- [177] J. Ruiz, B. Gonzalo, J. R. Dios, J. M. Laza, J. L. Vilas, L. M. León, *Adv. Polym. Technol.* **2013**, *32*, E180.
- [178] E. L. Kalinchev, *Int. Polym. Sci. Technol.* **2002**, *29*, 55.
- [179] X. She, G. Song, J. Li, P. Han, S. Yang, W. Shulong, Z. Peng, *Polym. J.* **2006**, *38*, 639.
- [180] G. Stoychev, N. Puretskiy, L. Ionov, *Soft Matter* **2011**, *7*, 3277.
- [181] X. Huang, H. Mutlu, P. Theato, *Adv. Mater. Interfaces* **2020**, *7*, 2000101.
- [182] K. Liu, L. Jiang, *ACS Nano* **2011**, *5*, 6786.
- [183] Y. Cai, L. Lin, Z. Xue, M. Liu, S. Wang, L. Jiang, *Adv. Funct. Mater.* **2014**, *24*, 809.
- [184] J. Yong, F. Chen, Q. Yang, Z. Jiang, X. Hou, *Adv. Mater. Interfaces* **2018**, *5*, 1701370.
- [185] T. Du, S. Ma, X. Pei, S. Wang, F. Zhou, *Small* **2017**, *13*, 1.
- [186] T. Jiang, Z. Guo, W. Liu, *J. Mater. Chem. A* **2015**, *3*, 1811.
- [187] J. Tian, D. Kannangara, X. Li, W. Shen, *Lab Chip* **2010**, *10*, 2258.
- [188] S. Gao, J. Sun, P. Liu, F. Zhang, W. Zhang, S. Yuan, J. Li, J. Jin, *Adv. Mater.* **2016**, *28*, 5307.
- [189] X. Yao, J. Gao, Y. Song, L. Jiang, *Adv. Funct. Mater.* **2011**, *21*, 4270.
- [190] S. Krishnan, C. J. Weinman, C. K. Ober, *J. Mater. Chem.* **2008**, *18*, 3405.
- [191] G. Zhang, X. Zhang, Y. Huang, Z. Su, *ACS Appl. Mater. Interfaces* **2013**, *5*, 6400.
- [192] Z. Xue, S. Wang, L. Lin, L. Chen, M. Liu, L. Feng, L. Jiang, *Adv. Mater.* **2011**, *23*, 4270.
- [193] W. Ma, H. Xu, A. Takahara, *Adv. Mater. Interfaces* **2014**, *1*, 1300092.
- [194] M. Liu, S. Wang, Z. Wei, Y. Song, L. Jiang, *Adv. Mater.* **2009**, *21*, 665.

- [195] W. Liu, X. Liu, J. Fangteng, S. Wang, L. Fang, H. Shen, S. Xiang, H. Sun, B. Yang, *Nanoscale* **2014**, *6*, 13845.
- [196] X. Liu, J. Zhou, Z. Xue, J. Gao, J. Meng, S. Wang, L. Jiang, *Adv. Mater.* **2012**, *24*, 3401.
- [197] D. Wu, S. Wu, Q.-D. Chen, S. Zhao, H. Zhang, J. Jiao, J. A. Piersol, J.-N. Wang, H.-B. Sun, L. Jiang, *Lab Chip* **2011**, *11*, 3873.
- [198] E. Zhang, Z. Cheng, T. Lv, L. Li, Y. Liu, *Nanoscale* **2015**, *7*, 19293.
- [199] J. Yong, F. Chen, Q. Yang, U. Farooq, H. Bian, G. Du, X. Hou, *Appl. Phys. A* **2015**, *119*, 837.
- [200] Z. Cheng, H. Liu, H. Lai, Y. Du, K. Fu, C. Li, J. Yu, N. Zhang, K. Sun, *ACS Appl. Mater. Interfaces* **2015**, *7*, 20410.
- [201] M. Li, B. Wang, L. Heng, L. Jiang, *Adv. Mater. Interfaces* **2014**, *1*, 1400298.
- [202] D. Wu, S.-Z. Wu, Q.-D. Chen, Y.-L. Zhang, J. Yao, X. Yao, L.-G. Niu, J.-N. Wang, L. Jiang, H.-B. Sun, *Adv. Mater.* **2011**, *23*, 545.
- [203] M. Liu, L. Jiang, *Adv. Funct. Mater.* **2010**, *20*, 3753.
- [204] Y. Tokudome, K. Okada, A. Nakahira, M. Takahashi, *J. Mater. Chem. A* **2014**, *2*, 58.
- [205] H. Masuda, K. Fukuda, *Science*. **1995**, *268*, 1466.
- [206] H. Zhao, M. Zhou, L. Wen, Y. Lei, *Nano Energy* **2015**, *13*, 790.
- [207] E. Park, O. seok Kwon, S. joo Park, J. seop Lee, S. You, J. Jang, *J. Mater. Chem.* **2012**, *22*, 1521.
- [208] D. O'carroll, I. Lieberwirth, G. Redmond, *Nat. Nanotechnol.* **2007**, *2*, 180.
- [209] P. W. Bohn, *Annu. Rev. Anal. Chem.* **2009**, *2*, 279.
- [210] P. Kohli, M. Wirtz, C. R. Martin, *Electroanal. An Int. J. Devoted to Fundam. Pract. Asp. Electroanal.* **2004**, *16*, 9.
- [211] C. R. Martin, M. Nishizawa, K. Jirage, M. Kang, S. B. Lee, *Adv. Mater.* **2001**, *13*, 1351.
- [212] K. C. Popat, E. E. L. Swan, V. Mukhatyar, K.-I. Chatvanichkul, G. K. Mor, C. A. Grimes,

- T. A. Desai, *Biomaterials* **2005**, *26*, 4516.
- [213] S. Simovic, D. Losic, K. Vasilev, *Chem. Commun.* **2010**, *46*, 1317.
- [214] S. D. Alvarez, C.-P. Li, C. E. Chiang, I. K. Schuller, M. J. Sailor, *ACS Nano* **2009**, *3*, 3301.
- [215] M. Wang, G. Meng, Q. Huang, M. Li, Z. Li, C. Tang, *Analyst* **2011**, *136*, 278.
- [216] J. Bachmann, J. Escrig, K. Pitzschel, J. M. M. Moreno, J. Jing, D. Görlitz, D. Altbir, K. Nielsch, *J. Appl. Phys.* **2009**, *105*, 63.
- [217] W.-C. Tsai, S.-J. Wang, J.-K. Lin, C.-L. Chang, R.-M. Ko, *Electrochem. commun.* **2009**, *11*, 660.
- [218] J. Yong, F. Chen, Q. Yang, J. Huo, X. Hou, *Chem. Soc. Rev.* **2017**, *46*, 4168.
- [219] H. Zhao, P. Theato, *Polym. Chem.* **2013**, *4*, 891.
- [220] P. Theato, *J. Polym. Sci. Part A Polym. Chem.* **2008**, *46*, 6677.
- [221] S. Lin, A. Das, P. Theato, *Polym. Chem.* **2017**, *8*, 1206.
- [222] S. Lin, X. Huang, R. Guo, S. Chen, J. Lan, P. Theato, *J. Polym. Sci. Part A Polym. Chem.* **2019**, *57*, 1580.
- [223] A. Das, P. Theato, *Chem. Rev.* **2016**, *116*, 1434.
- [224] S. Lin, J. Shang, P. Theato, *ACS Macro Lett.* **2018**, *7*, 431.
- [225] Q. Cheng, M. Li, F. Yang, M. Liu, L. Li, S. Wang, L. Jiang, *Soft Matter* **2012**, *8*, 6740.
- [226] L. P. Xu, J. Peng, Y. Liu, Y. Wen, X. Zhang, L. Jiang, S. Wang, *ACS Nano* **2013**, *7*, 5077.
- [227] B. Su, Y. Tian, L. Jiang, *J. Am. Chem. Soc.* **2016**, *138*, 1727.
- [228] P. Singleton, P. Mazliak, *Bacteria in Biology, Biotechnology and Medicine*, Wiley Chichester, **1997**.
- [229] T. B. Tennikova, M. Bleha, F. Švec, T. V Almazova, B. G. Belenkii, *J. Chromatogr. A* **1991**, *555*, 97.
- [230] R. Ghosh, *J. Chromatogr. A* **2002**, *952*, 13.

- [231] H. U. Osmanbeyoglu, T. B. Hur, H. K. Kim, *J. Memb. Sci.* **2009**, *343*, 1.
- [232] A. Rath, P. Theato, *Adv. Funct. Mater.* **2019**.
- [233] A. Santos, T. Kumeria, D. Losic, *TrAC - Trends Anal. Chem.* **2013**, *44*, 25.
- [234] S. B. Lee, D. T. Mitchell, L. Trofin, T. K. Nevanen, H. Söderlund, C. R. Martin, *Science* . **2002**, *296*, 2198.
- [235] S. Kipke, G. Schmid, *Adv. Funct. Mater.* **2004**, *14*, 1184.
- [236] S. U. Hong, M. L. Bruening, *J. Memb. Sci.* **2006**, *280*, 1.
- [237] W. Shi, Y. Shen, D. Ge, M. Xue, H. Cao, S. Huang, J. Wang, G. Zhang, F. Zhang, *J. Memb. Sci.* **2008**, *325*, 801.
- [238] Y. Huang, H. Li, L. Wang, Y. Qiao, C. Tang, C. Jung, Y. Yoon, S. Li, M. Yu, *Adv. Mater. interfaces* **2015**, *2*, 1400433.
- [239] N. T. Phuong, A. Andisetiawan, D. Van Lam, J. H. Kim, D. S. Choi, K. H. Whang, J. Nham, Y. J. Lee, Y. E. Yoo, J. S. Yoon, *Sci. Rep.* **2016**, *6*, 1.
- [240] M. Agheli, A. Habibolahzadeh, *Prot. Met. Phys. Chem. Surfaces* **2016**, *52*, 972.
- [241] M. Fujiwara, T. Imura, *ACS Nano* **2015**, *9*, 5705.
- [242] J. Song, H. Oh, H. Kong, J. Jang, *J. Hazard. Mater.* **2011**, *187*, 311.
- [243] Z. Zhang, L. Wen, L. Jiang, *Chem. Soc. Rev.* **2018**, *47*, 322.
- [244] Z. Liu, W. Wang, R. Xie, X.-J. Ju, L.-Y. Chu, *Chem. Soc. Rev.* **2016**, *45*, 460.
- [245] G. Kang, Y. Cao, *J. Memb. Sci.* **2014**, *463*, 145.
- [246] A. Tufani, G. Ozaydin Ince, *J. Memb. Sci.* **2019**, *575*, 126.
- [247] S. Y. Yang, I. Ryu, H. Y. Kim, J. K. Kim, S. K. Jang, T. P. Russell, *Adv. Mater.* **2006**, *18*, 709.
- [248] H. Zhao, L. Liu, Y. Lei, *Front. Chem. Sci. Eng.* **2018**, *12*, 481.
- [249] S. P. Pujari, L. Scheres, A. T. M. Marcelis, H. Zuilhof, *Angew. Chemie Int. Ed.* **2014**, *53*, 6322.

- [250] P.-F. Li, R. Xie, J.-C. Jiang, T. Meng, M. Yang, X.-J. Ju, L. Yang, L.-Y. Chu, *J. Memb. Sci.* **2009**, *337*, 310.
- [251] A. Tufani, G. O. Ince, *J. Memb. Sci.* **2017**, *537*, 255.
- [252] C. Song, W. Shi, H. Jiang, J. Tu, D. Ge, *J. Memb. Sci.* **2011**, *372*, 340.
- [253] M. Motornov, R. Sheparovych, E. Katz, S. Minko, *ACS Nano* **2007**, *2*, 41.
- [254] L. A. Fielding, S. Edmondson, S. P. Armes, *J. Mater. Chem.* **2011**, *21*, 11773.
- [255] Q. Yan, R. Zhou, C. Fu, H. Zhang, Y. Yin, J. Yuan, *Angew. Chemie Int. Ed.* **2011**, *50*, 4923.
- [256] S. Lin, P. Theato, *Macromol. Rapid Commun.* **2013**, *34*, 1118.
- [257] Q. Zhang, L. Lei, S. Zhu, *ACS Macro Lett.* **2017**, *6*, 515.
- [258] Z. Guo, Y. Feng, S. He, M. Qu, H. Chen, H. Liu, Y. Wu, Y. Wang, *Adv. Mater.* **2013**, *25*, 584.
- [259] L. Dong, W. Fan, H. Zhang, M. Chen, Y. Zhao, *Chem. Commun.* **2017**, *53*, 9574.
- [260] C. P. Sharma, M. C. Sunny, *Biomaterials* **1990**, *11*, 255.
- [261] Z. Zhang, T. Shimizu, S. Senz, U. Gösele, *Adv. Mater.* **2009**, *21*, 2824.
- [262] G. E. J. Poinern, X. Le, C. Loomes, D. Fawcett, *Mater. Lett.* **2014**, *131*, 182.
- [263] R. Pal, D. Kundu, *J. Non. Cryst. Solids* **2009**, *355*, 76.
- [264] D. Wang, J. Tan, H. Kang, L. Ma, X. Jin, R. Liu, Y. Huang, *Carbohydr. Polym.* **2011**, *84*, 195.
- [265] B. Schneider, J. Štokr, P. Schmidt, M. Mihailov, S. Dirlikov, N. Peeva, *Polymer (Guildf)*. **1979**, *20*, 705.
- [266] D. Han, O. Boissiere, S. Kumar, X. Tong, L. Tremblay, Y. Zhao, *Macromolecules* **2012**, *45*, 7440.
- [267] D. Han, X. Tong, O. Boissière, Y. Zhao, *ACS Macro Lett.* **2011**, *1*, 57.
- [268] H. Jiang, E. Wang, J. Wang, *RSC Adv.* **2015**, *5*, 35622.

- [269] S. Kumar, X. Tong, Y. L. Dory, M. Lepage, Y. Zhao, *Chem. Commun.* **2013**, 49, 90.
- [270] S. Turgman-Cohen, J. Genzer, *J. Am. Chem. Soc.* **2011**, 133, 17567.
- [271] L. Hu, S. Gao, Y. Zhu, F. Zhang, L. Jiang, J. Jin, *J. Mater. Chem. A* **2015**, 3, 23477.
- [272] D. Stokes, *Principles and Practice of Variable Pressure/Environmental Scanning Electron Microscopy (VP-ESEM)*, John Wiley & Sons, **2008**.
- [273] E. V Shun'ko, V. S. Belkin, *J. Appl. Phys.* **2007**, 102, 83304.
- [274] P. R. Griffiths, J. A. De Haseth, *Fourier Transform Infrared Spectrometry.*, John Wiley & Sons, **2007**.
- [275] J. I. Goldstein, D. E. Newbury, J. R. Michael, N. W. M. Ritchie, J. H. J. Scott, D. C. Joy, *Scanning Electron Microscopy and X-Ray Microanalysis*, Springer, **2017**.

Appendix

List of Abbreviations

AAO	Anodic aluminum oxide
AIBN	2,2'-azobis(isobutyronitrile)
ATRP	Atom transfer radical polymerization
ATR	Attenuated total reflectance
ABP	4-Acryloylbenzophenone
AEBIB	<i>t</i> -Boc-aminoethyl 2-bromoisobutyrate
BF	Bright field
CA	Contact angle
CD ₂ Cl ₂	Dichloromethane-d ₂
CDCl ₃	Chloroform-d ₁
CTA	Chain transfer agent
CuBr	Copper(I) bromide
CuCl ₂	Copper(II) chloride
CrO ₃	Chromium(IV) oxide
CLSM	Confocal laser scanning microscope
CHCl ₃	Chloroform
DCM	Dichloromethane
DCE	1,2-Dichloroethane
DMF	<i>N,N</i> -dimethylformamide
DMSO	Dimethyl sulfoxide
DMSO-d ₆	Dimethyl sulfoxide-d ₆
DF	Dark field
DLS	Dynamic light scattering
DOP-SP	Dopamine self-polymerization
EtOH	Ethanol
EDX	Energy-dispersive X-ray
EDC	<i>N</i> -ethyl- <i>N</i> '-(3-dimethylaminopropyl)carbodiimide hydrochloride
FT-IR	Fourier-transformation infrared spectroscopy

GPC	Gel permeation chromatography
iCVD	Initiated chemical vapor deposition
LbL	Layer-by-layer
LCST	Lower critical solution temperature
MA	Mild anodization
MeOH	Methanol
MBAA	<i>N,N'</i> -methylenebisacrylamide
NaOH	Sodium hydroxide
NaOAc	Sodium acetate
NMR	Nuclear magnetic resonance
Na ₂ SO ₄	Sodium sulfate
NHS	<i>N</i> -hydroxysuccinimide
HA	Hard anodization
HDODA	1,6-Hexanediol diacrylate
H ₃ PO ₄	Ortho-phosphoric acid
HClO ₄	Perchloric acid
H ₂ O ₂	Hydrogen peroxide
Irgacure 2959	2-Hydroxy-4'-(2-hydroxyethoxy)-2-methylpropiophenone
PMMA	Poly(methyl methacrylate)
PS	Polystyrene
PAA	Poly(acrylic acid)
PAH	Poly(allylamine)
PCL	Poly(<i>ε</i> -caprolactone)
PDADMAC	Poly-(diallyldimethylammonium chloride)
PDMS	Polydimethylsioxane
PEDOT	Poly(3,4-ethylenedioxythiophene)
PEI	Poly(ethyleneimine)
P2VP	Poly(2-vinyl pyridine)
P4VP	Poly(4-vinylpyridine)
PNIPAm	Poly(<i>N</i> -isopropylacrylamide)
PPFPA	Poly(pentafluorophenyl acrylate)

PFP	Pentafluorophenyl
PDEAEMA	Poly(2-(diethylamino)ethyl methacrylate)
PMMA	Poly(methyl methacrylate)
PMD	Poly(methyl methacrylate- <i>co</i> -2-(diethylamino)ethyl methacrylate)
PMDETA	<i>N,N,N',N'',N'''</i> -Pentamethyldiethylenetriamine
PSS	Poly(styrenesulfonate)
PVS	Poly(vinylsulfate)
SDS	Sodium dodecyl sulfate
SI-ATRP	Surface-initiated atom transfer radical polymerization
SI-RAFT	Surface-initiated reversible addition-fragmentation chain-transfer
SEM	Scanning electron microscopy
S-CTA	Surface chain transfer agent
SiO ₂	Silicon dioxide
TA	Transition anodization
TMOS	Tetramethoxysilane or Tetramethyl orthosilicate
TEOS	Tetraethoxysilane or Tetraethyl orthosilicate
TEA	Trimethylamine
THF	Tetrahydrofuran
TEM	Transmittance electron microscopy
TGA	Thermogravimetric analysis
TFA	Trifluoroacetic acid
RAFT	Reversible addition-fragmentation chain-transfer
UCST	Upper critical solution temperature
UOCA	Underwater oil contact angle
UV-vis	Ultraviolet-visible
WCA	Water contact angle

List of Publications

- [1] **Xia Huang**, Hatice Mutlu, Patrick Théato*. A bio-inspired hierarchical anti-oilfouling surface with reversible pH response. *Advanced Materials Interfaces*, **2020**, 2000101.
- [2] Shaojian Lin, **Xia Huang**, Ronghui Guo, Sheng Chen, Janwu Lan, Patrick Théato*. UV-triggered CO₂-responsive behavior of nanofibers and their controlled drug release properties. *Journal of Polymer Science Part A: Polymer Chemistry*, **2019**, 57.
- [3] Bultema, Lindsey A, **Xia Huang**, Daniel D. Brauer, and Patrick Théato*. Polymer Functionalization. *Functional Polymers*, **2019**, 53-103.
- [4] **Xia Huang**, Hatice Mutlu, Patrick Théato*. The toolbox of porous anodic aluminum oxide based nanocomposites: From fabrication to application. *Colloid and Polymer Science*. Submitted.
- [5] **Xia Huang**, Hatice Mutlu, Patrick Théato*. CO₂-gated anodic aluminum oxide based nanocomposite membrane for de-emulsification. *Nanoscale*. Submitted.
- [6] **Xia Huang**, Hatice Mutlu, Patrick Théato*. Polymeric one-dimensional Janus nanorods via AAO templating. In preparation.

Conference Contributions

- [1] 2018 *Biennial Meeting of the GDCh-Division of Macromolecular Chemistry, Karlsruhe (DE)*
Poster presentation: Oxygen Changeable Aqueous UCST Transition of Uncharged Random Copolymers Through Post-Polymerization Modification
- [2] 2018 *Particle-Based Materials Symposium, Erlangen (DE)*
Poster presentation: Fabrication of Thermo-Responsive Polymeric Janus Nanorods via AAO Template

Acknowledgements

So far, my PhD study is approaching the ending, recalled that in the study period of four and half years I have met a lot of people, with their accompanying and help I just went here today this one pace. All of them deserve my sincerely gratitude.

First and foremost, I would like to express my gratitude to my supervisor Professor Dr. Patrick Théato who offer me the opportunity to join the flourishing research group and work on the interesting and challenging topic. Thank you for your continuous supporting on my research work from the designing of experiment to writing and revising scientific articles, as well as various problems that arises during my PhD period.

Furthermore, I would like to thank Prof. Pavel Levkin for his acceptance to be the co-referee of my thesis and I appreciate his time for reviewing my thesis.

I would like thank to Dr. Hatice Mutlu, thank you for your tireless guidance to my research work. Specially thanks for teaching me all the skills and tips for preparing scientific articles which benefited me a lot. Also thanks for your strong support for applying funding at my final PhD period. I want to thank Dr. Dominik Voll, Dr. Xiang Zhang and Prof. Weigui Fu, thanks for the fruitful discussion with you and always help me out when I meet problems on my experiment.

I also would like to appreciate our technician Katharina Elies who offering me the training on diverse laboratory testing instruments. And thank you for your support about ordering all the stuff that I need for the laboratory works.

I would thank Birgit Huber for the GPC measurement and thanks to Ms. Ingrid Zeller for the help on sputter coating.

Special thanks to Mr. Volker Zibat who helped me on the SEM measurement which is the most important characterization method during my research.

I would like to thank the people that I meet in Hamburg, with all your company I had a joyful time there. Very special thanks to Prof. Shaojian Lin and Prof. Jiaojiao Shang, thanks for your meticulous cares and with your help I had a smooth start of my life studying abroad and also thanks for your selfless sharing on scientific skills which helped had a smooth start of the research work as well. Thanks to Dr. Hanju Jo for your help on dealing with the AAO setup and sharing your knowledge on AAO. I would like to thank to Dr. Lirong He, Dr. Michael W. Thielke, Dr. Tim Krappitz, Dr. Alexander Hoefling, Dr. Heba Gaballa, Dr. Xiaoxiao Zhang, Julia Steicke, Fenja Moldenhauer, Sven and Xinyang Liu. It's nice to having you and working with you, thanks for all

your help during my study in Hamburg. Special thanks to my friend Dr. Fu Li, Dr. Jiaying Sun, Linyu Mu and Mengyu Zhang, thanks for cheering me up when I was done.

I would also thank Xiaohui for your company from Hamburg to Karlsruhe, from lab to office. Thank to Araya, my intern from Thailand. Thanks for your help on dealing with my experiments. Thanks Hongxin, Yunji, Zengwen and Wenyuan for your support on dealing with daily laboratory works, it's nice to have discussions with you and it also inspiring me a lot on my research works. Special thanks to Johannes you are always kind to offer me help on sample characterization and thanks for driving me from time to time to Campus North, it's so lucky for me to have you in our research group. I would like also thank to Isabella, Marvin, Meryem, Sergej, Martin, Stefan, Andreas, Edgar, Victoria, Ziwei, Linrui, Yan, Wenwen, David and Vaishali, *et al.*, you are all wonderful colleague and I'm appreciate working with all of you.

I sincerely thank China Scholarship Council (CSC) for a fellowship for supporting my doctoral research. I would also thank DAAD STIBET for the pre-graduation scholarship during the final period of my doctoral research.

My deepest gratitude goes to my family for their strong support, understanding and always be patient to encourage me during my studies.

Last but not least, I have meet many people during my PhD studies which are not listed above, thank you for sharing your time with me which made my journey in Germany unforgettable.